

General-purpose Data-driven Wall Model for Low-speed Flows Part I: Baseline Model

Yuenong Ling*

Department of Aeronautics and Astronautics, Massachusetts Institute of Technology, Cambridge, MA 01239, USA

Imran Hayat

Graduate Aerospace Laboratories, California Institute of Technology, Pasadena, CA 91125, USA

Konrad Goc

The Boeing Company, Everett, 98204 WA, USA

Adrian Lozano-Duran

*Department of Aeronautics and Astronautics, Massachusetts Institute of Technology, Cambridge, MA 02139, USA and
Graduate Aerospace Laboratories, California Institute of Technology, Pasadena, CA 91125, USA*

We present a general-purpose wall model for large-eddy simulation (LES). The model builds on the building-block flow principle [1], leveraging essential physics from simple flows to train a generalizable model applicable across complex geometries and flow conditions. The model addresses key limitations of traditional equilibrium wall models (EQWM) and improves upon shortcomings of earlier building-block-based approaches. The model comprises four components: (i) a baseline wall model, (ii) an error model, (iii) a classifier, and (iv) a confidence score. The baseline model predicts the wall-shear stress, while the error model estimates epistemic errors (due to missing or unrepresented physics) and aleatoric errors (stemming from unpredictable physics), both used for uncertainty quantification. When appropriate, the error model corrects the baseline prediction, enabling additive learning without retraining or overfitting. The classifier identifies the flow regime and the training data used to make predictions, improving the explainability of the model. Finally, the confidence score quantifies prediction reliability, flagging instances of extrapolation or operation outside the range of applicability of the baseline model. In Part I of this work, we present the baseline model, while the remaining three components are introduced in Part II. The baseline model is designed to capture a broad range of flow phenomena, including turbulence over curved walls and zero, adverse, and favorable mean pressure gradients (PGs), as well as flow separation and laminar flow. The problem is formulated as a regression task to predict wall shear stress using a feedforward artificial neural network. Model inputs are localized in space and dimensionless, with their selection guided by information-theoretic criteria. Training data include, among other cases, a newly generated direct numerical simulation dataset of turbulent boundary layers under favorable and adverse PG conditions. Validation is carried out through both *a priori* and *a posteriori* tests. The *a priori* evaluation spans 140 diverse high-fidelity numerical datasets and experiments (67 training cases included), covering turbulent boundary layers, airfoils, Gaussian bumps, and full aircraft geometries, among others. We demonstrate that the baseline wall model outperforms the EQWM in 90% of test scenarios, while maintaining errors below 20% for 98% of the cases.

I. INTRODUCTION

Wall-modeled large-eddy simulation (WMLES) is a key tool for simulating high-Reynolds-number turbulence across diverse scientific and engineering applications. Compared with wall-resolved LES (WRLES) and direct numerical simulation (DNS), WMLES is computationally tractable: it resolves large energy-containing eddies while modeling the near-wall dynamics, enabling accurate predictions of complex flows at competitive cost suitable for industrial design [2, 3]. However, many wall models rely on strong equilibrium assumptions that break down in separated flows, under strong pressure gradients, or during laminar-to-turbulent transition, which limits their accuracy and generalizability [4–8].

To address these challenges, non-equilibrium wall models have been developed to account for departures from the idealized equilibrium behavior of near-wall turbulence. Here, we use the term *non-equilibrium* to denote any deviation from the canonical zero-pressure-gradient (ZPG) turbulent boundary layer. One class of non-equilibrium wall models

* Contact author: lingyn@mit.edu

consists of Reynolds-Averaged Navier–Stokes (RANS)-based partial differential equation (PDE) formulations, which have proven effective in capturing non-equilibrium effects [9–12]. However, their use in WMLES is limited because they require a secondary mesh with full connectivity, complicating implementation and reducing solver efficiency. Moreover, despite their sophistication, RANS-based-PDE wall models are not a panacea: they often require ad hoc tuning of eddy-viscosity closures across flow scenarios [13], while still underperforming in favorable-pressure-gradient (FPG) regions and separation [14].

Ordinary differential equation (ODE) non-equilibrium wall models relax the secondary-mesh connectivity requirement by estimating one or more terms in the wall-shear-stress balance (convective, pressure-gradient, and viscous) [15–20]. Other approaches include dynamic slip-based models that adjust a slip length to infer wall shear stress (τ_w) predictions [21–23]. Mixed viscous and pressure-gradient scalings have also been leveraged to incorporate pressure-gradient effects [24, 25], and analytical non-equilibrium models have been derived from asymptotic solutions [26]. More recently, sensor-based augmentation has been proposed to enhance stresses where pressure gradients dominate near separation [27]. While these strategies perform well in the cases for which they were developed, many still depend on case-specific assumptions, limiting their ability to generalize across the broad range of flows encountered in WMLES.

Another critical challenge is the need for laminar wall models, which are essential for accurately predicting the leading-edge region of wings and the subsequent transition to turbulence [2]. Because the laminar boundary layer is extremely thin, resolving it within the standard WMLES framework is computationally prohibitive. Moreover, without special treatment, deploying a wall model designed for turbulent flow can induce large errors, degrading lift and drag predictions and even triggering spurious leading-edge separation [7]. One remedy is to use sensors to switch between a wall model and a no-slip boundary condition—effectively resolving the near-wall region—when turbulent activity is low [28]; however, this still demands fine near-wall resolution. To address these limitations, several laminar wall-modeling strategies have been proposed. Gonzalez *et al.* [29] and Dauricio and Azevedo [30] derived analytical solutions based on Falkner–Skan boundary-layer theory to predict local wall shear stress, and Dujardin [31] showed that coupling a laminar and a turbulent wall model via a sensor can improve airfoil simulations. Other approaches have proposed the use of parabolized stability equations for the laminar region [32]. While promising, most prior approaches rely on boundary-layer edge (outer-layer) quantities as inputs, which can be difficult to obtain or even ill-defined in simulations over complex geometries [33].

Over the past decade, data-driven wall models have increasingly relied on machine learning (ML) to infer mappings from the resolved field to the wall shear stress using high-fidelity data, typically parameterized by artificial neural networks (ANNs) of varying complexity. Table I summarizes existing ML-based wall models, including their input structure, physics considered, and reported generalization capability. Early developments focused on channel-flow datasets and leveraged the law of the wall to train neural networks for τ_w prediction [34–36]. These efforts were later extended to include rotation effects [37] and high-speed-flow regimes [38]. Beyond supervised learning, reinforcement-learning strategies have also been explored to infer optimal wall-modeling policies [39–41]. In addition, graph neural networks have been employed to model wall shear stress [42–44], and non-local convolutional neural-network (CNN) wall models have been evaluated through both *a priori* and *a posteriori* analyses [45–48]. A different direction was introduced by Lozano-Durán and Bae [1], who proposed a building-block strategy designed to capture multiple near-wall physical mechanisms while providing prediction confidence. This approach has since demonstrated strong applicability to complex geometries [49–53], and it is the one adopted in the present work.

Paradoxically, despite the promise of ML to enable general-purpose wall models, most existing approaches remain fundamentally limited in scope. By construction, many models cannot be applied broadly given the required inputs, and even in the cases where they are applicable, they often underperform relative to simple equilibrium wall models. As a result, only a few ML wall models have seen adoption in practical simulations. The key challenges are:

1. *Arbitrary geometries.* Many models rely on non-local inputs that are not directly tied to near-wall quantities, complicating implementation or even preventing their use in general geometries. For example, while CNNs can capture non-local effects, adapting planar or grid-aligned inputs to complex surfaces often limits their practicality. Other models do not comply with rotation, translation, or Galilean invariance, which are fundamental physical requirements that any model must satisfy.
2. *Insufficient physics* Practical applications involve superposed effects (mean PG effects, flow separation, wall curvature, laminar flow, etc.), yet most models are trained on a handful of canonical cases where crucial regimes are often missing. Even when relevant physics are present (e.g., periodic hills with pressure gradients, separation, and curvature), studies typically target a single geometry and a narrow range of Reynolds numbers, encouraging memorization rather than learning transferable physics.
3. *Limited validation.* Many data-driven models are tested on one or few cases closely resembling their training set. As summarized in Table I, with the notable exceptions of Lozano-Durán and Bae [1] (and follow-up

TABLE I: Overview of machine-learning wall models, ordered chronologically. Columns report (i) input locality, (ii) input structure, (iii) physics considered, (iv) applicability to arbitrary geometries, (v) training database, and (vi) untrained test cases that differ substantially from the training data. **Input Locality** refers to the classification as local (\checkmark), non-local (\times), or semi-local ($-$). **Input Structure** specifies the data organization: *Points* (one or more spatial samples), *Graph* (graph-neural-network topology), *Integral* (integrals of known quantities), or *Plane* (full planar fields). **Physics Considered** includes turbulence under zero/adverse/favorable mean-pressure gradients (ZPG/APG/FPG), mean-flow three-dimensionality (3D), Rotation, wall Curvature, Laminar flow, Separation, and statistically unsteady turbulence (Unsteady). **Arbitrary Geometry** (\checkmark) indicates applicability to arbitrary geometries. **Training cases** list datasets used for model development, while **Untrained Test Cases** enumerate distinct flows used to assess generalization as reported in the original sources. Unless otherwise noted, all flows are turbulent.

	Year	Input Locality	Input Structure	Physics Considered	Arbitrary Geometry	Training Case	Untrained Testing Cases
Yang <i>et al.</i> [34]	2019	\times	Points	ZPG	\times	Channel	Channel with spanwise acceleration
Huang <i>et al.</i> [37]	2019	-	Points	ZPG Rotation	\times	Channel with spanwise rotation	N/A
Zangeneh [38]	2021	\times	Points	ZPG APG/FPG	\times	Supersonic TBL Expansion/ Compression Corner	N/A
Zhou <i>et al.</i> [35]	2021	\times	Points	APG/FPG Curvature	\times	Periodic hill	Channel
Bae and Koumoutsakos [39]	2022	-	Points	ZPG	\checkmark	Channel	ZPG TBL
Lozano-Durán and Bae [1]	2023	\checkmark	Points	Laminar ZPG Separation APG/FPG 3D Unsteady	\checkmark	Laminar Channel Channel Channel with PG 3D Channel	Laminar BL Turbulent BL Pipe NASA CRM-HL NASA Juncture Flow
Dupuy <i>et al.</i> [42]	2023	\times	Points	ZPG APG/FPG Separation 3D	\times	Channel Backward Step 3D Diffuser	N/A
Dupuy <i>et al.</i> [43]	2023	\times	Graph	ZPG APG/FPG Curvature Separation 3D	\checkmark	Channel Blade Backward Step Smooth Ramp 3D Diffuser	N/A
Tabe Jamaat and Hattori [45]	2023	\times	Plane	ZPG	\times	Channel	N/A
Lee <i>et al.</i> [54]	2023	\times	Integral	ZPG	\times	Channel	Separation Bubble
Vadrot <i>et al.</i> [41]	2023	$-$	Points	ZPG	\checkmark	Channel	N/A
Zhou <i>et al.</i> [36]	2023	\times	Points	APG/FPG Curvature	\checkmark	Periodic Hill Law of the Wall	N/A
Maejima <i>et al.</i> [55]	2024	\times	Points	ZPG	\checkmark	ZPG TBL	N/A
Radhakrishnan <i>et al.</i> [56]	2024	\checkmark	Points	ZPG APG/FPG 3D	\checkmark	Channel 3D Diffuser	Juncture NASA Hump
Zhou and Bae [40]	2024	-	Points	APG/FPG Curvature	\checkmark	Periodic Hill	Gaussian Bump
Boxho <i>et al.</i> [48]	2025	\times	Points	ZPG APG/FPG Curvature	\times	Channel Periodic Hill	N/A
Zhang <i>et al.</i> [57]	2025	\times	Points	APG/FPG Curvature	\times	Periodic Hill	Gaussian Bump
Zhou <i>et al.</i> [58]	2025	\times	Points	APG/FPG Curvature	\times	Periodic Hill	Wavy Wall

versions) and Radhakrishnan *et al.* [56], most works do not report performance on flows that differ substantially from training. Systematic benchmarking across diverse, out-of-training distributions is essential to avoid over-optimistic conclusions and to guide iteration.

4. *Lack of explainability.* Most ML wall models behave as black boxes that map inputs to τ_w without exposing which mechanisms drive their predictions. This opacity limits physical interpretation. Thus, a model can perform accurately on benchmarks yet “get the right answer for the wrong reasons,” due to error cancelation, a risk that may go unnoticed in practice. Explainability tools are needed to reveal the basis of the predictions and make model behavior more transparent; however, they remain rarely used in wall modeling with few exceptions [49].
5. *Need for uncertainty quantification (UQ).* Most ML wall models return estimates of τ_w without a confidence measure or a decomposition of *epistemic* versus *aleatoric* uncertainty. In realistic WMLES settings—where ground truth is unavailable—UQ is vital to detect out-of-distribution inputs, prioritize additional data collection, trigger mesh/SGS/wall-model adaptation, and support risk-aware decisions. Accordingly, models should report predictive distributions or credible intervals with reliability metrics, not just a mere point prediction.
6. *Effect of external errors.* Wall models are susceptible to (i) *external* errors propagated from the outer LES field and its subgrid-scale (SGS) model, and (ii) *internal* errors due to the wall-modeling assumptions themselves [59, 60]. Even a physically exact wall model would inherit outer-layer inaccuracies; in practice, it has been shown that external errors can completely degrade the performance of accurate wall models [49]. Thus, improving the wall model alone is insufficient and advances in SGS modeling and outer-layer accuracy are also required to improve WMLES performance.

We develop a wall model that addresses the six challenges outlined above. The overall approach is summarized in Figure 1. In Part I, we tackle Challenges 1–3; Challenges 4 and 5 are treated in Part II. Challenge 6 is deferred to future work to be addressed by the SGS model. An overview of all the modeling components is shown in Figure 1. The approach is rooted in the building-block-flow principle—extracting essential physics from simple canonical cases—and is implemented with an artificial neural network. The formulation facilitates incorporating diverse cases into the training set, constructed from mean-flow statistics. Among these, we leverage a new DNS dataset spanning turbulent boundary layers (TBLs) subjected to a range of mean-pressure-gradient conditions. Model performance is validated against a comprehensive suite of experimental and high-fidelity numerical benchmarks, covering varied flow physics including pressure gradients, wall curvature, and laminar–turbulent transition, among others.

The remainder of the paper is organized as follows. Section II introduces the wall-model formulation, the training database, and outlines the non-dimensional input-selection methodology. Section III presents comprehensive *a priori* assessments and *a posteriori* WMLES results. Finally, Section IV discusses the limitations of the current model and outlines directions for future extensions.

II. METHODOLOGY

A. Overview of building-block flow model

The wall model follows the building-block flow model (BFM) principle of Lozano-Durán and Bae [1]. The central assumption is that the unresolved physics in complex scenarios can be locally mapped to the small-scale dynamics of simpler flows. Accordingly, we posit a finite set of *building-block flows* (BBFs) that encapsulate the essential physics needed to construct generalizable wall models. This design prioritizes learning the governing mechanisms rather than memorizing cases—for example, avoiding correct predictions over a particular wing merely because similar wings appeared in the training set—and thus aims to capture the underlying flow physics faithfully.

The building-block idea has been used for both subgrid-scale (SGS) models (to represent unresolved motions away from the wall) and wall models (to represent the missing scales at solid boundaries). The first implementation (version 1), BFM-v1, was introduced in our prior work [49, 53, 61], which comprised coupled SGS model (BFM-SGS-v1) and wall model component (BFM-WM-v1) and extensions accounting for wall roughness in incompressible and compressible flow regimes [50, 62]. BFM-v1 was assessed across flows ranging from low geometric complexity (turbulent channels, pipes, boundary layers) to moderate (airfoils, Gaussian bump) and fully complex configurations (aircraft-like geometries). While BFM-v1 improves upon traditional wall models, it still underperforms in several regimes. Here, we present the second-generation wall model component, referred to as BFM-WM-v2. The updated SGS model component (BFM-SGS-v2) will be reported in a subsequent work.

We summarize the model requirements we aim to satisfy, following the guidelines from our previous work [1]:

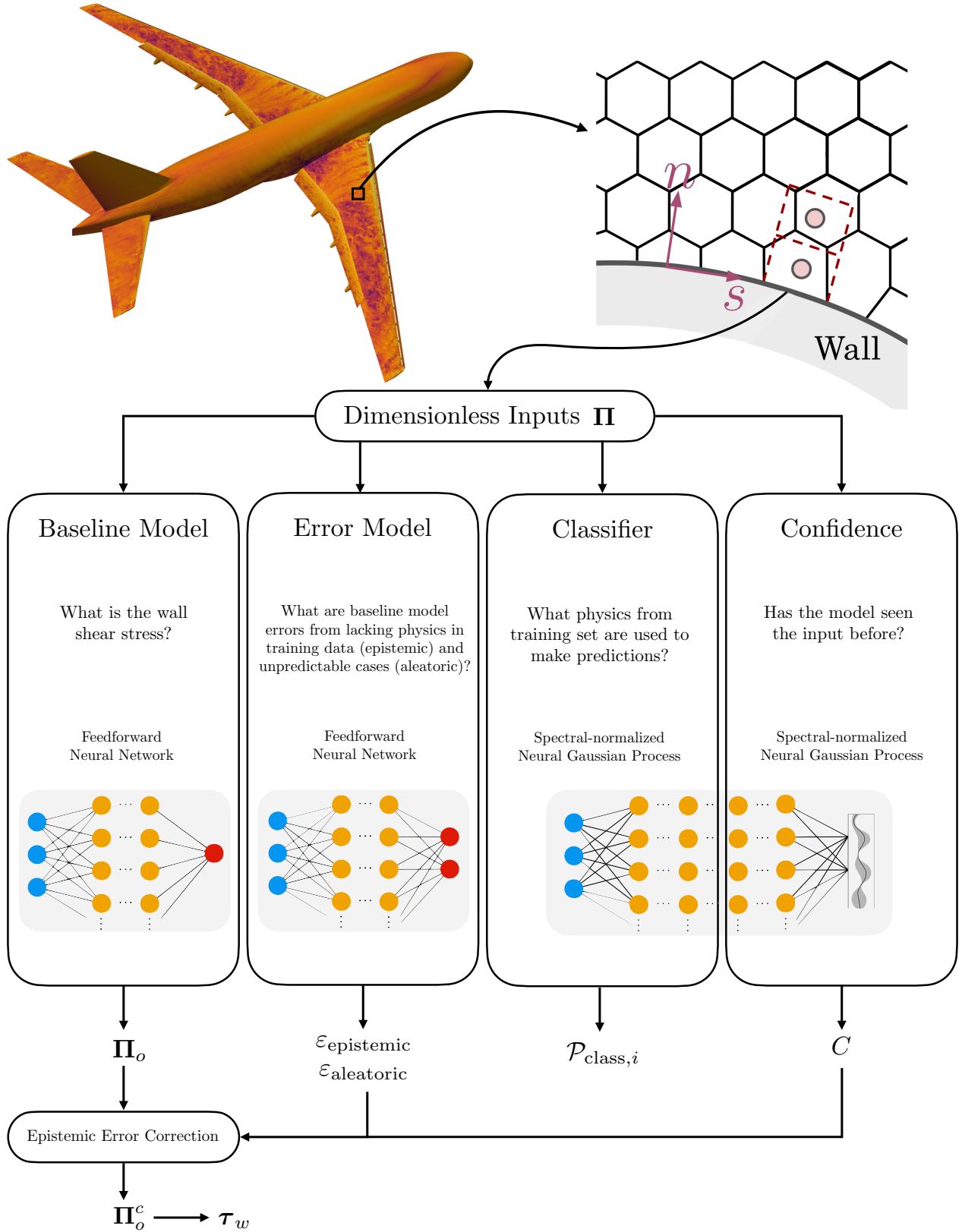


FIG. 1: Overview of the building-block flow wall model version 2 (BFM-WM-v2). The model comprises four components: (i) a baseline wall model, (ii) an error model, (iii) a classifier, and (iv) a confidence score. Each panel contains the question the module is aiming to answer. When appropriate, the error model corrects the baseline prediction. The model inputs and output are formulated in dimensionless form. In Part I of this work, we present the baseline model. The other three components are presented in Part II.

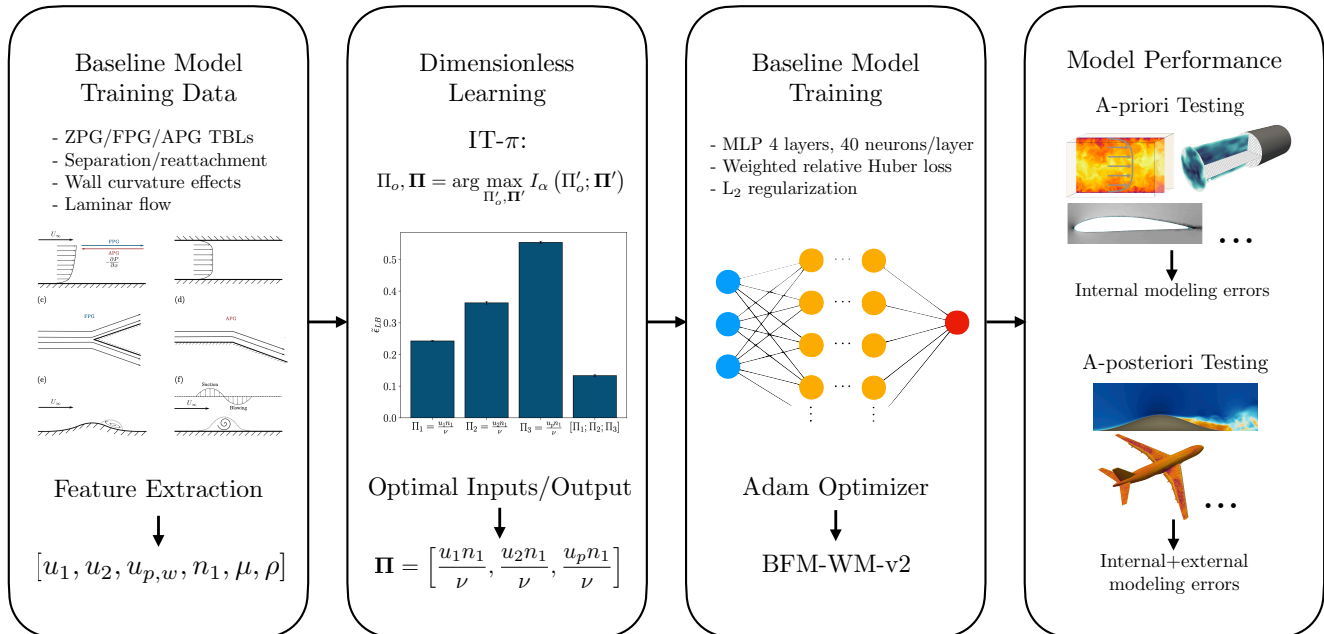


FIG. 2: Workflow of the training data, dimensionless input/output design, training process, and testing of the baseline model.

1. The wall model should provide accurate predictions of the *mean* (e.g., time-averaged) wall shear stress, rather than attempting to capture its time-dependent dynamics.
2. The model must account for different flow regimes (e.g., laminar flow, wall-attached turbulence, separated flow, ...) in a unified manner, i.e., the input and output structure must remain identical across all cases.
3. The formulation must be scalable, allowing additional flow physics (building-block flows) to be incorporated in future versions.
4. The model must provide a confidence score and an uncertainty estimate for its prediction at each wall location.
5. The formulation must be directly applicable to complex geometries with unstructured grids without requiring any case-specific modifications.
6. The input set should exclude wall-normal gradients. This choice is motivated by the fact that, in WMLES, the near-wall grid is deliberately coarse. As a result, wall-normal gradients depend strongly on the numerical scheme used, and excluding them improves portability across solvers.
7. All model inputs and outputs must be expressed in dimensionless form to ensure dimensional homogeneity, i.e., invariance under changes in the units of the variables.
8. The model must satisfy Galilean invariance and remain invariant under constant spatial and temporal translations, as well as rotations of the reference frame.

Figure 2 shows an overview of the preparation of training data, the design of dimensionless input and output variables, the training procedure, and the evaluation of the baseline model.

B. Main model assumptions

We discuss the key assumptions underlying the model. In addition to the standard WMLES assumptions, the main assumptions specific to BFM-WM-v2 are:

- *Building-block-flow assumption:* This is the main assumption of the wall model, namely that there is a finite set of simple flows (building-block flows) that contain the essential flow physics to formulate generalizable wall models.
- *Local state sufficiency:* We assume that the local flow state provides the necessary information for accurately predicting the wall shear stress. This assumption is supported by recent findings showing that history effects are small in the near-wall region of statistically unsteady wall turbulence and PG turbulent boundary layers [13, 63]. Although incorporating global information could further improve predictions, restricting the inputs to local quantities ensures applicability to arbitrarily complex geometries.
- *Ensemble-averaged inputs for training:* The model is trained on ensemble-averaged values of near-wall DNS data rather than instantaneous samples. This choice is motivated by the objective of predicting the mean wall shear stress accurately, without reproducing instantaneous dynamics. The approach offers several advantages: First, it simplifies data preparation and reduces the complexity of the training process. Second, it enables the inclusion of a wider range of flow cases by leveraging mean quantities without requiring full flow fields. Finally, it avoids the underfitting issues reported when training deterministic models with complex instantaneous inputs [42]. When deployed, a time-averaging filter is applied to the instantaneous WMLES inputs during inference to approximate the averaged value [1, 64].
- *Wall-shear stress direction:* We assume that the wall-shear stress vector, $\boldsymbol{\tau}_w$, is aligned with the velocity vector at the first grid point, \mathbf{u}_1 , which corresponds to the velocity in the WMLES grid closest to the wall and serves as an input to the wall model. As a result, the primary task of the model is to predict only the magnitude of the wall-shear stress, τ_w . This assumption is supported by evidence that, at high Reynolds numbers and for typical WMLES wall-normal grid spacing, $\boldsymbol{\tau}_w$ and \mathbf{u}_1 remain aligned on average within a reasonable margin of error [13].

C. Baseline model formulation

The wall model predicts the wall-shear stress vector $\boldsymbol{\tau}_w$ based on local near-wall flow features, which is imposed as boundary conditions for the LES equations. The procedure is illustrated in Figure 3a. The prediction of $\boldsymbol{\tau}_w$ is formulated as

$$\boldsymbol{\tau}_w = \text{ANN}(\mathbf{q}; \boldsymbol{\theta}) \frac{\mathbf{u}_1}{u_1}, \quad (1)$$

where \mathbf{q} is the input feature vector composed of near-wall flow quantities, and ANN denotes a feedforward artificial neural network with trainable parameters $\boldsymbol{\theta}$. The direction of $\boldsymbol{\tau}_w$ is assumed to align with the wall-parallel velocity at the first off-wall grid point, \mathbf{u}_1 , and $u_1 = \|\mathbf{u}_1\|$, where $\|\cdot\|$ denotes the Euclidean norm.

Figure 3b illustrates the set of local input features included in \mathbf{q} . These comprise the wall-parallel velocities at various distances from the wall, $u_1 = u|_{n=n_1}$, and $u_2 = u|_{n=3n_1}$, where n_1 is the wall-normal distance of the first grid point. These quantities characterize the shape of the local velocity profile. We also examined an extended stencil that includes $u_3 = u|_{n=5n_1}$ and $u_4 = u|_{n=7n_1}$. However, the results indicate that the added complexity yields only marginal improvements.

To capture the effect of streamwise pressure gradients, the model also includes a pressure-gradient/acceleration-based velocity at the wall:

$$u_p = \text{sign} \left(\frac{1}{\rho} \frac{\partial p}{\partial s} \Big|_w + \frac{\partial u_{\parallel}}{\partial t} \Big|_w \right) \left| \mu \left(\frac{1}{\rho} \frac{\partial p}{\partial s} \Big|_w + \frac{\partial u_{\parallel}}{\partial t} \Big|_w \right) \right|^{1/3}, \quad (2)$$

where $\partial p / \partial s|_w$ is the wall-parallel pressure gradient projected along the local flow direction (s),

$$\frac{\partial p}{\partial s} \Big|_w = \nabla_{\mathbf{x}_{\parallel}} p \cdot \mathbf{u}_{1\parallel}, \quad (3)$$

with $\nabla_{\mathbf{x}_{\parallel}}$ the spatial gradient operator and $(\cdot)_{\parallel}$ denotes projection onto the wall-parallel plane. The term $\partial u_{\parallel} / \partial t|_w$ is the wall-parallel acceleration of the wall with respect to an inertial frame of reference. The model also takes as input the local kinematic viscosity μ and density ρ . In summary, the input feature vector is

$$\mathbf{q} = [u_1, u_2, u_p, n_1, \mu, \rho], \quad (4)$$

where all variables are dimensional. Their dimensionless form is discussed in §III E.

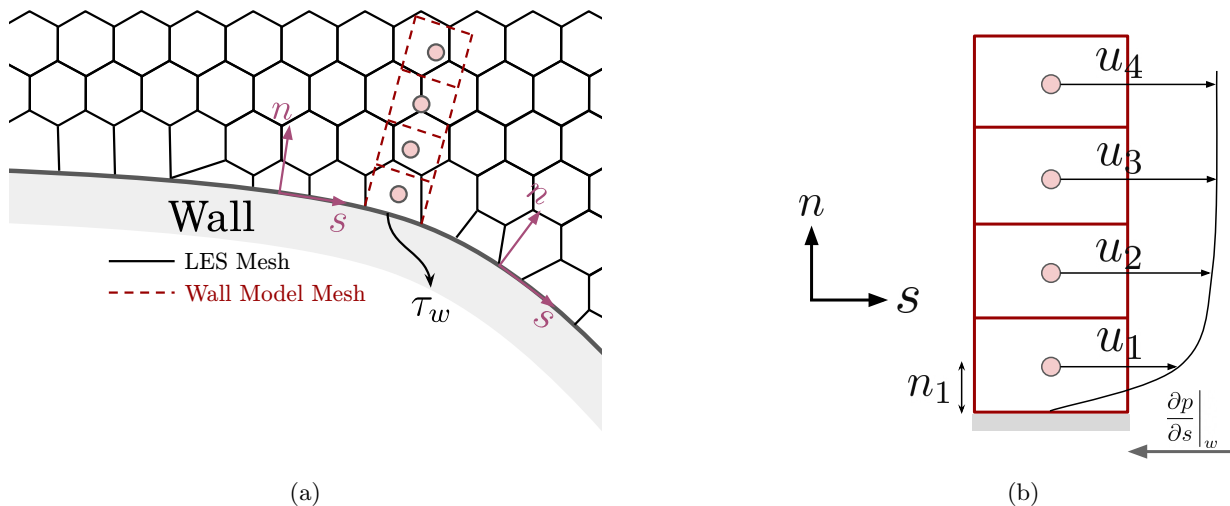


FIG. 3: (a) Wall-model mesh (dashed red) defined in the local (n, s) coordinates over a curved wall; the surrounding unstructured LES mesh is shown in black. (b) Dimensional inputs investigated to construct the wall model, in addition to fluid properties such as density and viscosity. Subscripts 1–4 denote the i -th off-wall grid point, and the subscript w indicates wall values.

TABLE II: Summary of training cases. Details of flow parameters can be found in the text.

Case	Dominant Flow Physics	Type	Subcase Count	Symbol
APG & FPG turbulent boundary layers (Arranz and Lozano-Durán [65])	ZPG/APG/FPG Separation	DNS	16	∇
Turbulent channel flows (Lozano-Durán and Jiménez [66], Lee and Moser [67], Hoyas <i>et al.</i> [68])	Akin ZPG	DNS	6	c
Synthetic data by the log law [69]	High-Re ZPG	Analytical	3	s
Falkner-Skan laminar boundary layers (Falkner and Skan [70])	Laminar APG/FPG	Analytical/ODE	40	l
Spanwise-periodic Gaussian bump ($Re_L = 2M$) (Uzun and Malik [71])	Wall curvature Separation	DNS/WRLES	1	★
Pressure-induced turbulent separation bubbles (Kamogawa <i>et al.</i> [19])	Separation w/ reattachment	WRLES	1	\curvearrowright

D. Training database

The training database used to develop the wall model is summarized in Table II, with representative flow cases shown in Figure 4. Following the building-block principle, we select simple flow configurations that isolate key physical mechanisms relevant for wall modeling. Our aim is to assemble a database that is both diverse and physically rich. The dataset includes turbulent channel flows, ZPG/FPG/APG turbulent boundary layers, separation bubbles with subsequent reattachment, wall-curvature effects, laminar flows, and high-Reynolds-number conditions.

The training data include all quantities required to construct the input–output pairs (\mathbf{q}, τ_w) to train the wall model. Sampling is performed over a broad range of wall-normal matching locations along streamwise directions, as illustrated in Figure 5. Specifically, the wall-model matching height h_{wm} is normalized by the local boundary layer thickness δ , and varies from $h_{\text{wm}}/\delta = 0.005$ to 0.25. This corresponds to spatial resolutions ranging from approximately 200 to just 4 grid points per δ . The range spans from the finest grid resolutions feasible in complex geometries to highly under-resolved settings, where only a few grid points lie within the boundary layer [59, 60]. This ensures the training data reflect both idealized and practically relevant WMLES conditions. A total of $N \sim 10^6$ input–output pairs are collected for the training dataset.

In the following, we discuss the rationale behind including each specific case in the training database and describe

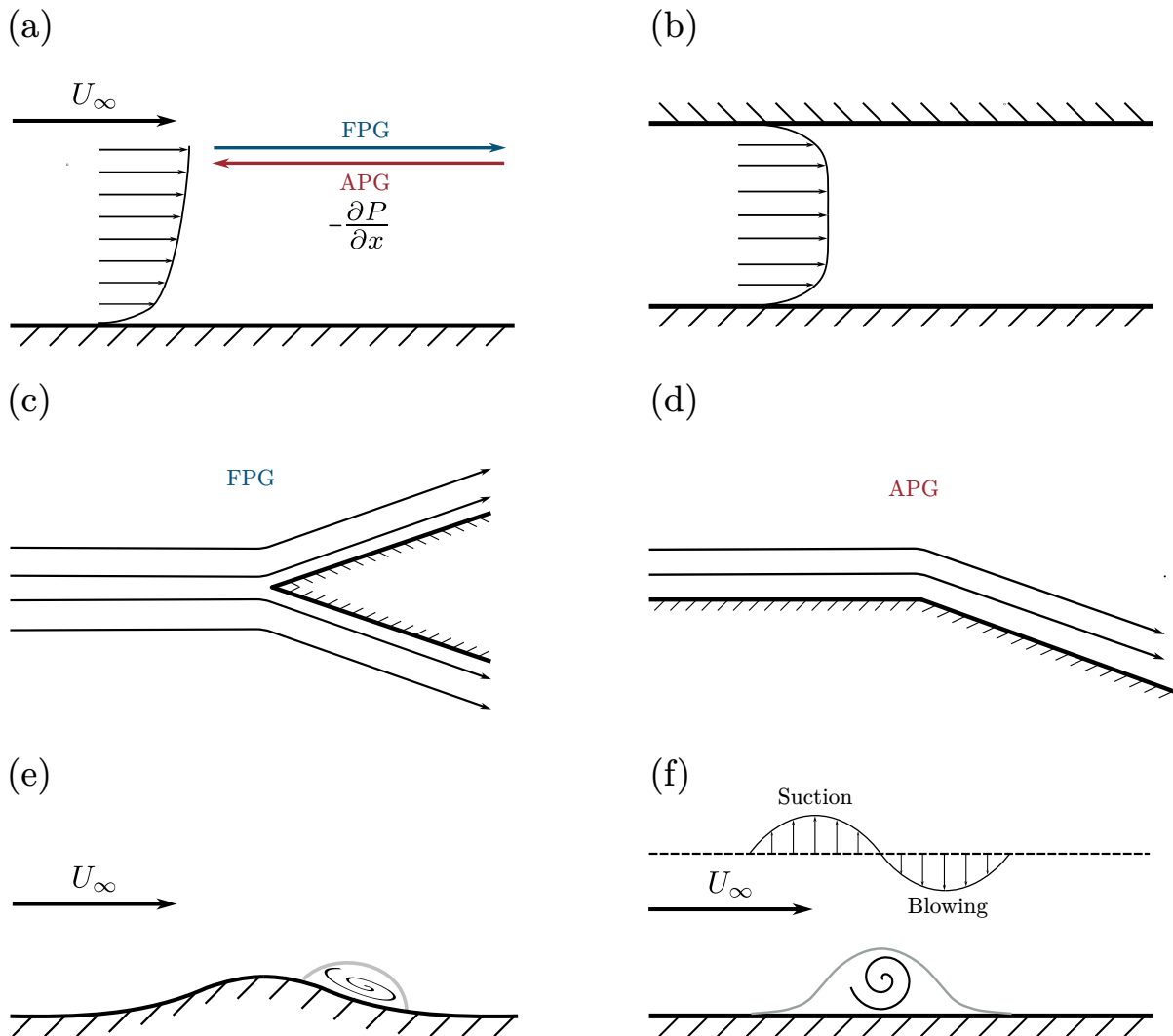


FIG. 4: Schematics of representative training cases. (a) APG and FPG turbulent boundary layers; (b) turbulent channel flows; (c) FPG Falkner–Skan laminar flow; (d) APG Falkner–Skan laminar flow; (e) spanwise-periodic Gaussian bumps; (f) pressure-induced turbulent separation bubbles. Regions enclosed by grey lines indicate separated flow.

the corresponding flow parameters.

1. *ZPG, APG, and FPG turbulent boundary layers.* We employ a new collection of DNS of TBLs spanning zero-, adverse-, and favorable-pressure-gradient conditions by prescribing a ceiling with a virtual straight ramp that deflects the freestream either upward (APG) or downward (FPG) [65]. This configuration generates statistically stationary, spatially developing TBLs with controlled pressure-gradient histories, including attached, incipiently separated, and reattaching states—thus covering the range of behaviors encountered in practical aerodynamic applications. The inclusion of this dataset is motivated by the need to capture non-equilibrium near-wall physics induced by streamwise pressure gradients—effects that are poorly represented in canonical ZPG databases and often absent or too limited in existing datasets. The ramp deflection angle is varied over $\alpha \in \{-4^\circ, -3^\circ, -2^\circ, -1^\circ, 5^\circ, 10^\circ, 15^\circ, 20^\circ\}$, producing favorable ($\alpha < 0$), zero ($\alpha \approx 0$), and adverse ($\alpha > 0$) pressure gradients. The pressure-gradient intensity is characterized by the Clauser parameter $\beta = (\delta^*/\tau_w) (dP_e/dx)$, where δ^* is the displacement thickness and dP_e/dx is the edge-pressure gradient. We have $\beta \approx 0$ for ZPG, $\beta < 0$ for FPG, and $\beta > 0$ for APG, with $\beta \rightarrow \infty$ in the limit of separation as $\tau_w \rightarrow 0$. The cases cover the range $\beta \in [-0.6, \infty)$. Two inflow Reynolds numbers, $Re_{in} = 300$ and 670 , are used, yielding a momentum-thickness Reynolds-number range of $300 < Re_\theta < 10^4$. Additional details on the case setup and simulation parameters are provided in Appendix A.

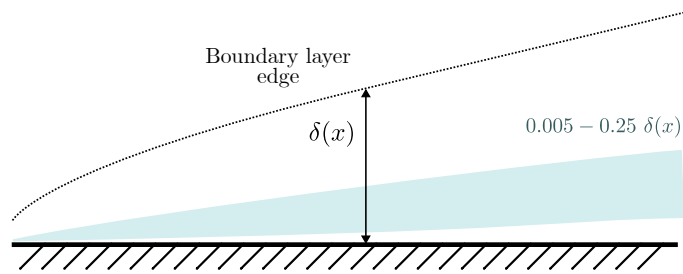


FIG. 5: The sampling region for the training data covering the range $0.005-0.25 \delta(x)$, where $\delta(x)$ is boundary layer thickness.

2. *Turbulent channel flow.* This case represents fully developed turbulent flow between two parallel plates, driven by a constant pressure gradient under statistically steady conditions. Its simple geometry and absence of mean streamwise pressure gradients make it a canonical configuration for isolating near-wall turbulence physics. The data considered several friction Reynolds numbers, defined as $Re_\tau = u_\tau h / \nu$, where $u_\tau = \sqrt{\tau_w / \rho}$ is the friction velocity, h is the channel half-height, and ν is the kinematic viscosity. Specifically, we include $Re_\tau = 550, 950, 2000, 4200, 5200,$ and 10000 [66–68].
3. *Synthetic log-law for high Reynolds numbers.* This dataset consists of analytically generated velocity profiles based on the classical logarithmic law of the wall [5, 69], representative of ZPG turbulent boundary layers at high Reynolds numbers. These profiles emulate the asymptotic behavior of wall-bounded turbulence in regimes currently inaccessible to DNS. This guides the model to predict correct physics when deployed in simulations where no high-fidelity training data exist. We include three representative friction Reynolds numbers in this category: $Re_\tau = 5 \times 10^4, 10^6,$ and 5×10^6 .
4. *Falkner–Skan laminar boundary layers.* This dataset comprises similarity solutions of laminar flat-plate boundary layers with streamwise acceleration or deceleration, obtained by numerically solving the Falkner–Skan [70] ODE via a shooting method. The cases are computed on smooth flat surfaces with no curvature so that pressure-gradient effects are isolated in a clean laminar setting. The rationale for including these cases is to train the wall model with an explicit laminar regime and a physically consistent response to streamwise pressure gradients prior to transition. The edge velocity is prescribed as $U_e = Cx^m$, where x is the streamwise coordinate, C is a constant, and m controls the pressure gradient: negative m yields decelerating flow with possible incipient separation, while positive m produces accelerating flow. The aim is to avoid spurious leading-edge separation or incorrect shear in low-Re zones, and to encode how acceleration ($m > 0$) steepens the near-wall profile while deceleration ($m < 0$) thickens it toward separation. The parameter range follows $m \in \{-0.0904, -0.08, -0.05, 0, 0.1, 0.6, 1.0, 2.0\}$, covering scenarios from incipient separation through strong favorable pressure gradients. Four freestream-based Reynolds numbers are used spanning 10^3 to 10^5 , resulting in 40 subcases in total.
5. *2-D Gaussian bump.* This case employs the spanwise-periodic Gaussian bump of Uzun and Malik [71] to introduce controlled surface curvature on an otherwise simple flat-plate configuration. The purpose of including this case is to isolate the influence of curvature on near-wall turbulence and wall shear stress without introducing confounding effects associated with complex geometries. Instead of prescribing curvature as an explicit input feature, we encode its effects implicitly by sampling velocities along multiple wall-normal directions. This strategy enables the model to infer curvature-induced modifications directly from local flow signatures while remaining applicable to flat walls, curved surfaces, and rotating systems. The incoming boundary layer encounters a smooth convex rise followed by recovery, producing streamwise variations of curvature, pressure gradient, and thickness with minimal geometric complexity. The computational setup is three-dimensional and periodic in the span, and the reference Reynolds number is $Re_L = 2 \times 10^6$ based on the bump length scale, yielding a fully turbulent approach flow and a broad range of local non-equilibrium responses. The parameterization includes a curvature range summarized by $\delta/R \in [0, 0.07]$, representative of many practical applications, together with the streamwise evolution from mild APG on the upstream face to FPG over the downstream recovery. The local Clauser parameter $\beta = (\delta^* / \tau_w)(dP_e/dx)$, varies smoothly across the bump, capturing attached flow, potential incipient separation, and recovery without relying on equilibrium assumptions. Although not as exhaustively parametric as the APG/FPG flat-plate suite, this configuration supplies high-quality training data at $Re_L = 2 \times 10^6$ with realistic curvature levels and coupled PG effects. As detailed in Appendix D, it is necessary to include this dataset to improve the model performance for cases with curved geometry.

6. *Blowing-suction-induced separation bubbles.* This dataset comprises simulations of a flat-plate TBL that undergoes controlled separation and reattachment by imposing a suction–blowing distribution at the freestream. The forcing generates a strong APG followed by a FPG, producing a separated shear layer that reattaches downstream and a recovery region with pronounced non-equilibrium dynamics [19]. The rationale for including these cases is to expose the wall model to the physics of shear-layer development and reattachment. Training on these flows teaches the model how wall stress behaves as τ_w weakens and approaches zero at separation, and how the outer shear layer interacts with and impinges on the wall during reattachment. This informs the behavior of the model in extended reattaching zones—regimes where canonical log-law scaling breaks down and where equilibrium-based closures systematically fail [72, 73]. The flow setup is characterized by an upstream $Re_\theta \approx 2000$ and a streamwise evolution of β that becomes large and positive approaching the separation point (as $\tau_w \rightarrow 0$) and turns negative in the FPG-driven recovery after reattachment. The case thus samples a broad range of states from attached flow through separation to reattached recovery, providing critical coverage for wall-stress prediction under strong APG/FPG transients.

E. Dimensionless learning by information-theoretic Buckingham- π

The model operates internally with dimensionless input and output variables. This ensures dimensional homogeneity—i.e., invariance under changes in the units of all quantities—which is a necessary requirement for constructing generalizable models. Violating this principle leads to models that are physically inconsistent and lack robustness across different flow conditions. Here, we examine the optimal dimensionless formulation of the input and output variables to achieve maximum predictive performance.

The construction of dimensionless variables, as guided by the Buckingham- π theorem [74], is not uniquely determined. Traditional approaches to identifying dimensionless variables rely heavily on physical intuition; however, such choices are not guaranteed to be optimal, in the sense that they may not produce a set of dimensionless variables with the highest predictive power. Here, we adopt a more systematic strategy using the Information-Theoretic Buckingham- π (IT- π) approach introduced by Yuan and Lozano-Durán [75]. This method leverages information-theoretic principles to identify the most predictive input and output dimensionless variables. The core insight of the approach is that the predictive capability of any model is fundamentally bounded by the amount of information the inputs carry about the outputs [76], where information is defined in the formal sense of information theory [77]. A key feature of IT- π is that the identification of optimal dimensionless variables is independent of the model structure, whether it involves analytical expressions, neural networks, or other functional forms. This methodology has previously been applied to derive optimal dimensionless inputs for wall models incorporating compressibility and surface roughness effects [50, 75].

The optimal dimensionless inputs $\mathbf{\Pi} = [\Pi_1, \Pi_2, \dots, \Pi_l]$ and dimensionless output Π_o can be found by solving the optimization problem:

$$\Pi_o, \mathbf{\Pi} = \arg \min_{\Pi'_o, \mathbf{\Pi}'} \tilde{\epsilon}_{LB}, \quad (5)$$

where $\tilde{\epsilon}_{LB} = e^{-I[\Pi_o; \mathbf{\Pi}]}$ denotes the normalized irreducible error and $I[\cdot; \cdot]$ is the mutual information [77]. As shown by Yuan and Lozano-Durán [75], $\tilde{\epsilon}_{LB}$ quantifies the portion of the prediction error that cannot be reduced any further regardless of the underlying modeling approach. Its values lie in $[0, 1]$, with smaller values indicating lower irreducible error. We use this approach to determine both the required number of inputs and their corresponding dimensionless form. The optimization problem from Eq. (5) is solved by employing the covariance matrix adaptation evolution strategy (CMA-ES)[78] using *pycma* package [79]. The reader is referred to Yuan and Lozano-Durán [75] for additional details.

The dataset used to identify the optimal dimensionless variables via IT- π corresponds to the training set introduced in §II, which is also employed later to train the wall model. The optimization process was limited to a maximum of 400 iterations, with a population size of 200 and a convergence tolerance of 10^{-5} . We progressively increased the number of required input features until the normalized irreducible error $\tilde{\epsilon}_{LB}$ ceased to decrease. The results, shown in the left panel of Figure 6, indicate that the optimal number of inputs is three. when the number of inputs increases from 3 to 4, the reduction in the normalized irreducible error is marginal. The three optimized dimensionless inputs and the optimal dimensionless output are

$$\mathbf{\Pi} = \left[\frac{u_1 n_1}{\nu}, \frac{u_2 n_1}{\nu}, \frac{u_p n_1}{\nu} \right], \quad \Pi_o = \frac{u_\tau n_1}{\nu}. \quad (6)$$

These inputs can be interpreted as local Reynolds numbers based on the first and second off-wall grid points, as well as the pressure-gradient velocity-scale Reynolds number, while the output corresponds to the local friction Reynolds

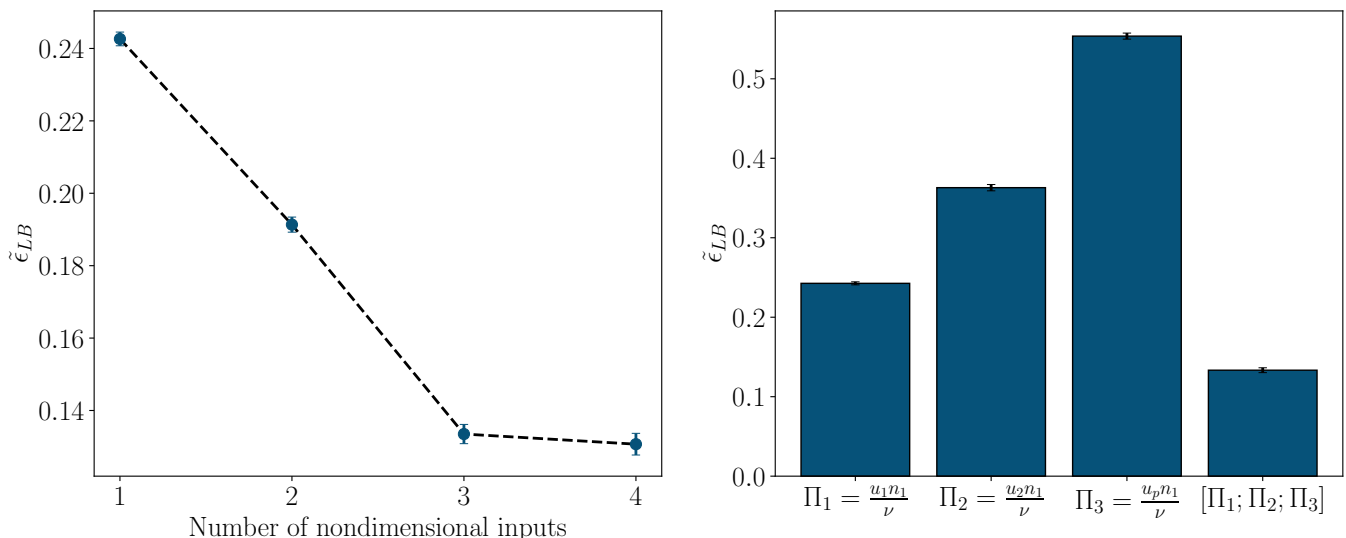


FIG. 6: (Left) Optimal normalized irreducible error as a function of the number of dimensionless inputs considered. (Right) Normalized irreducible error for the optimal three-input solution, $\mathbf{\Pi} = [\Pi_1, \Pi_2, \Pi_3]$, evaluated using each individual dimensionless input and using all three inputs jointly. Error bars denote the estimated uncertainty in $\tilde{\epsilon}$.

number. The irreducible errors associated with each individual variable from the optimal solution along with their combination are summarized in the right panel of Figure 6. The predictive capabilities of the inputs follow the ordering $\tilde{\epsilon}_{LB}(u_1 n_1/\nu) < \tilde{\epsilon}_{LB}(u_2 n_1/\nu) < \tilde{\epsilon}_{LB}(u_p n_1/\nu)$. This explains the strong predictive performance of EQWMs, which typically rely on $u_1 n_1/\nu$. Incorporating $u_2 n_1/\nu$ enables detection of changes in the shape of the mean velocity profile (due to PG effects, laminar flow, wall curvature, etc.). Finally, $u_p n_1/\nu$ further assists in capturing pressure-gradient effects.

F. Model architecture and training

The regression task in terms of the optimal dimensionless variables is defined as

$$\Pi_o = \text{ANN}(\mathbf{\Pi}; \boldsymbol{\theta}), \quad (7)$$

where the input vector is given by $\mathbf{\Pi} = [u_1 n_1/\nu, u_p n_1/\nu, u_2 n_1/\nu]$, and the output is $\Pi_o = u_\tau n_1/\nu$ as determined in the §II E. We employ a multilayer perceptron (MLP) architecture consisting of four hidden layers, each with forty neurons. The activation function used in all layers is the Rectified Linear Unit (ReLU). The selected network size has proven sufficient to accurately fit the training data while avoiding overfitting.

To ensure balanced training across different flow regimes, weights inversely proportional to the number of samples in each subcase from Table II are applied. Specifically, let $\mathcal{C} = \{C_1, C_2, \dots, C_n\}$ denote the collection of $n = 67$ distinct flow datasets from subcases in Table II, where each dataset C_i contains N_i samples and $\sum_{i=1}^n N_i = N$. The weight w_i assigned to each sample $s \in C_i$ is defined as

$$w_i = \frac{N}{N_i}, \quad \text{if } s \in C_i. \quad (8)$$

A weighted relative Huber loss is employed to reduce the influence of outliers during training [80]. The loss for a single sample is given by

$$L_h(\Pi_o^{\text{true}}, \text{ANN}(\mathbf{\Pi})) = \begin{cases} \frac{1}{2} w \left(\frac{\Pi_o^{\text{true}} - \text{ANN}(\mathbf{\Pi})}{|\Pi_o^{\text{true}}| + \epsilon} \right)^2, & \text{if } \frac{|\Pi_o^{\text{true}} - \text{ANN}(\mathbf{\Pi})|}{|\Pi_o^{\text{true}}| + \epsilon} \leq \sigma, \\ w \sigma \left(\frac{|\Pi_o^{\text{true}} - \text{ANN}(\mathbf{\Pi})|}{|\Pi_o^{\text{true}}| + \epsilon} - \frac{1}{2} \sigma \right), & \text{otherwise,} \end{cases} \quad (9)$$

where Π_o^{true} is the true output, $\sigma = 1$ is the threshold hyperparameter, w is the sample weight defined in Eq. (8), and $\epsilon = 10^{-8}$ is a small constant added to prevent division by zero. To prevent overfitting, an L_2 regularization term is

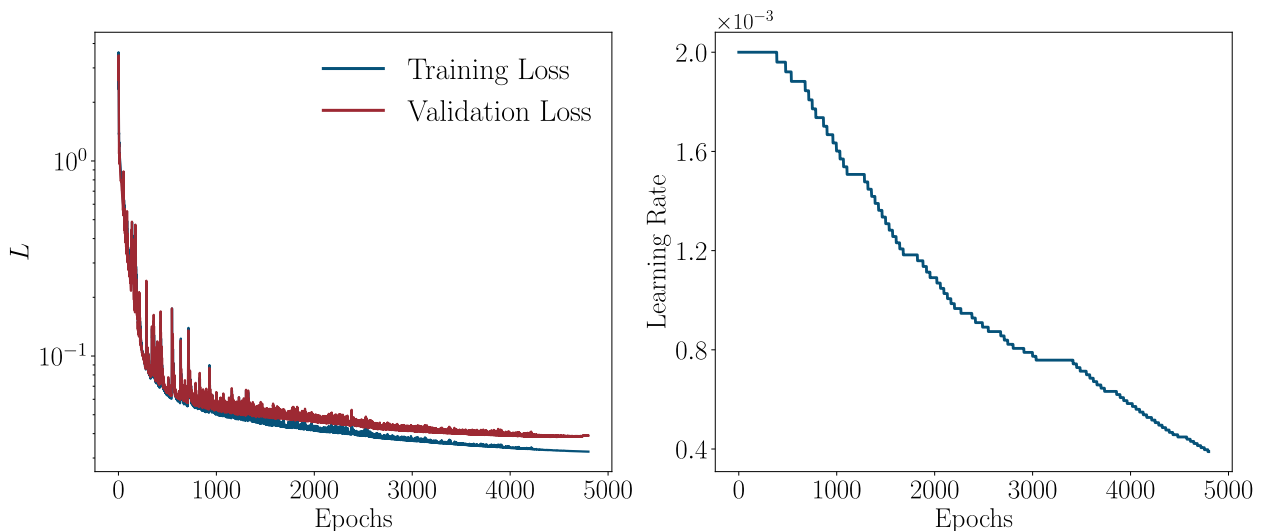


FIG. 7: Left: Convergence history of the loss function L as defined in Eq. (10). Right: Learning rate history due to the learning rate scheduler.

added to the total loss function, defined as

$$L = \frac{1}{N} \sum_{i=1}^N L_h(\Pi_{o,i}^{\text{true}}, \text{ANN}(\Pi_i)) + \frac{\lambda}{2} \sum_{l=1}^L \|\mathbf{W}^{(l)}\|_F^2, \quad (10)$$

where the index i denotes the i -th training sample, $\mathbf{W}^{(l)}$ is the weight matrix at the l -th layer of the MLP, $\|\cdot\|_F$ denotes the Frobenius norm, and $\lambda = 10^{-5}$ is the regularization hyperparameter.

The complete dataset was partitioned into training, validation, and testing sets using a 7:1.5:1.5 ratio. Training was performed using the Adam optimizer [81], with decay rates 0.9 and 0.999, and an initial learning rate of 0.002. A learning rate scheduler was employed to reduce the learning rate by a factor of 0.95 when the validation loss failed to improve for more than 25 consecutive epochs. To avoid overfitting, an early stopping criterion was implemented, terminating training if the validation loss did not decrease for 100 consecutive epochs. The model was trained using the open-source PyTorch framework [82]. The convergence and learning rate histories are shown in Figure 7. The performance of the model on both training and validation sets are shown in Figure 8.

III. RESULTS

The collection of test cases comprises flow scenarios drawn from both experimental studies and high-fidelity numerical simulations. These cases have been compiled over the past 50 years through the collective efforts of researchers worldwide. In total, 140 cases (training cases included) are considered for evaluation. The selection is designed to span a broad range of flow physics—including regimes for which the model was not explicitly trained.

To evaluate the performance of our model, we adopt two complementary testing methodologies: *a priori* and *a posteriori* analyses. The *a priori* test assesses model performance using input–output pairs derived directly from high-fidelity data, bypassing the need to run full WMLES. In contrast, the *a posteriori* test involves coupling the wall model to an SGS model and conducting WMLES. In this work, we place greater emphasis on the *a priori* assessment. This decision is motivated by the distinct nature of the errors inherent in wall modeling [60], which can be broadly categorized into two types, internal errors and external errors:

- *Internal errors* represent the intrinsic physical limitations of the wall model. Even in the presence of exact (i.e., error-free) input data, the wall model may produce inaccurate results when its physical assumptions do not hold. For example, internal errors can arise from the inadequacy of the model to accurately model the physics of the near-wall region (e.g., compressibility effects, separation patterns not captured in the training database, three-dimensional turbulent boundary layer effects, etc.). One example of internal error is the erroneous prediction of wall-shear stress by the classic equilibrium wall model when using the mean velocity profile from a separation bubble obtained via DNS as input. Although the input is error-free, the prediction may still exhibit significant inaccuracies, as the model is not designed to account for separated flows.

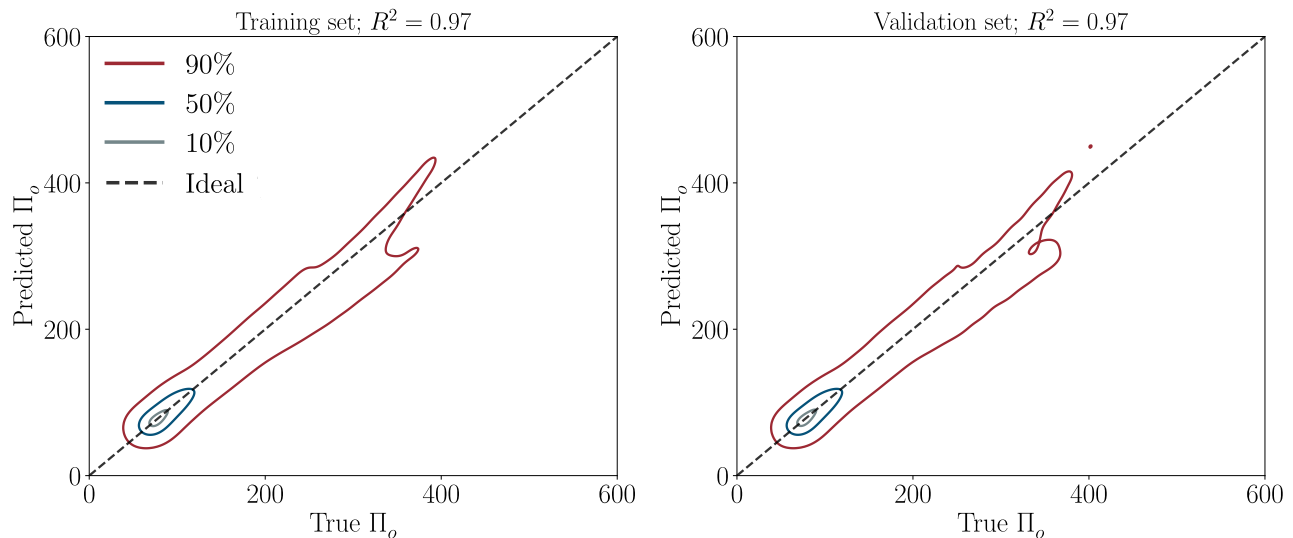


FIG. 8: Joint probability density contours of predicted versus true values of Π_o . Contours enclose 10%, 50%, and 90% of the data for the training set (left) and validation set (right). In both cases, the high coefficient of determination ($R^2 = 0.97$) demonstrates strong agreement between the predicted and true outputs.

- *External errors* are introduced by exogenous factors unrelated to the wall model itself. These errors originate from imperfect input data in actual WMLES. A dominant contributor is the performance of the SGS model: underperformance of the SGS model leads to inaccurate mean profiles, which in turn propagate errors into the wall model predictions. Additional sources of external error include history effects (e.g., imperfect inflow conditions), inadequate grid resolution (e.g., too few points per boundary-layer thickness), and uncertainties in other boundary conditions, to name a few. These errors are classified as external because they persist even when the wall model provides an exact physical representation of the near-wall region. The combined external and internal errors are collectively referred to as the total error. Continuing the example above, the equilibrium wall model will yield external errors in the prediction of wall-shear stress even when applied to a flat-plate ZPG TBL, if the input mean velocity profiles are inaccurate. This can occur even if the model was previously calibrated to produce nearly exact predictions in ZPG TBLs.

The distinction between internal and external errors plays a critical role in the design and evaluation of wall models. Internal errors arise from intrinsic limitations of the model itself, whereas external errors originate from factors beyond the model. In a practical WMLES setup (i.e., *a posteriori* testing), both types of errors are present, making it challenging to isolate and assess the contribution of each. The situation is further complicated by potential error cancellation between internal and external sources, which can be misleading and even counterproductive, leading to erroneous conclusions about the true performance of the wall model. Since the primary objective of this work is to evaluate the wall model, we focus on *a priori* testing as the principal means of performance assessment.

While our primary objective is to minimize internal errors, we also aim to evaluate the performance of our wall model within a realistic solver environment using *a posteriori* testing. To this end, we conduct the analysis using two modalities: *nudged a posteriori* testing and *true a posteriori* testing. In the former, we employ the nudged simulation approach proposed by Ling and Lozano-Durán [83], which mitigates the influence of the SGS model to reduce external wall-modeling errors. This method consists of performing *a posteriori* simulations in which the flow fields are nudged toward the correct statistical state of the flow. Specifically, a forcing term is added to the momentum equation to drive the velocity field toward the target mean velocity profile. In contrast, the *true a posteriori* test evaluates the total modeling error without explicitly separating internal and external contributions as encountered in practical WMLES. Addressing these external errors in WMLES requires advances in the SGS model, as demonstrated by BFM-v1 [53]. The development of its successor, BFM-SGS-v2, is presented in a subsequent work.

A. *A priori* testing

The set of cases used for *a priori* testing is summarized in Table III. Each entry in the table typically represents a family of flow conditions, yielding a total of 70 distinct cases, none of which appear in the training set. Providing a full

account of all individual variations would be cumbersome; therefore, we do not detail them here. Interested readers are referred to the original sources (cited in the table) for detailed descriptions of the corresponding simulations or experiments. Instead, we provide a high-level overview of the scenarios considered. The test set includes internal flows (pipe, square duct, rotating channel), turbulent boundary layers under zero, favorable, and adverse pressure gradients, and a variety of separated flows—such as pressure-induced separation bubbles with and without sweep, converging–diverging channels, backward-facing steps, Gaussian bumps, smooth ramps, axisymmetric separated boundary layers, rounded steps, and wall-mounted humps. The set also comprises strongly three-dimensional and curvature-dominated flows, including concave, convex, and curved walls; periodic hills; laterally strained and spinning cylinders; swept wings; a 3D diffuser; and airfoils spanning laminar, transitional, and near-stall regimes. In addition to these cases, the training set in Table II—which is not included in Table III—is also used to evaluate the wall model, contributing an additional 67 cases. For each case, we examine multiple spatial positions along the walls as well as a range of matching locations (corresponding to different WMLES grid resolutions) spanning $0.005\text{--}0.25\delta$. Between 10 and 100 matching locations are evaluated at each spatial position, yielding a total of $\mathcal{O}(1000)$ case scenarios.

We evaluate the performance of the wall model using two complementary error metrics, chosen based on the proximity of the flow to incipient separation. The rationale for using two metrics is to avoid spuriously large relative errors when $\tau_{w,\text{true}} \rightarrow 0$, a situation that typically arises near separation. The *relative error* is defined as

$$\varepsilon(\%) = \frac{|\tau_{w,\text{true}} - \tau_{w,\text{pred}}|}{|\tau_{w,\text{true}}|}, \quad (11)$$

and the *dimensionless error* is defined as

$$\varepsilon = \frac{|\tau_{w,\text{true}} - \tau_{w,\text{pred}}|}{\rho U_o^2}. \quad (12)$$

Here, U_o is an outer velocity scale used for normalization (e.g., freestream velocity for external flows and bulk inlet velocity for internal flows). In what follows, when the flow is far from incipient separation—quantified by the condition $|u_{\tau,\text{true}}|\delta/\nu > 50$ —we report the relative error $\varepsilon(\%)$. Conversely, when the flow is close to incipient separation, i.e., $|u_{\tau,\text{true}}|\delta/\nu \leq 50$, we assess performance using the dimensionless error ε .

For reference, we compare the performance of BFM-WM-v2 against a standard algebraic equilibrium wall model (EQWM). The friction velocity u_τ in the EQWM is obtained by solving

$$u^+(n_1^+) = \begin{cases} n_1^+ + a_1 (n_1^+)^2, & \text{for } n_1^+ < 23, \\ \frac{1}{\kappa} \ln n_1^+ + B, & \text{otherwise,} \end{cases} \quad (13)$$

where n_1 is the wall-normal matching location, $(\cdot)^+$ denotes normalization by the friction velocity u_τ and kinematic viscosity ν , $\kappa = 0.41$ is the von Kármán constant, and $B = 5.0$ is the log-law intercept [4, 6, 7].

1. Overview of model performance

We begin by providing an overview of the overall performance of BFM-WM-v2 compared with EQWM across all training and testing cases. For brevity in the notation, we refer to BFM-WM-v2 simply as BFM from this point onward. For each case, the errors are averaged over all spatial positions and matching locations, and the resulting mean values are reported. Figure 9 presents the probability density function (PDF) of these mean errors for all cases, comparing BFM with EQWM. The results show that BFM consistently outperforms EQWM, in most instances providing substantially improved accuracy.

Further insight into the model performance is provided in Figure 10 and Figure 11. The former compares the average errors of EQWM and BFM for cases far from incipient separation (i.e., $|u_{\tau,\text{true}}|\delta/\nu > 50$), while the latter presents results for cases close to separation (i.e., $|u_{\tau,\text{true}}|\delta/\nu \leq 50$). The symbols used for each case follow the conventions listed in Table III and Table II. Multiple occurrences of the same symbol indicate subcases corresponding to different flow conditions within the same main case. Based on these results, we can draw the following conclusions:

1. *For training cases*, BFM demonstrates high accuracy, confirming that the model has been properly constructed. This is reflected by the blue symbols in the figure, none of which exhibit relative errors exceeding 10%. For cases near incipient separation, the dimensionless errors remain small—as low as $\mathcal{O}(10^{-5})$ —which is an order of magnitude lower than the typical errors produced by EQWM at the same sample points.

TABLE III: Summary of the cases used for *a priori* testing. **Symbols** identify each case consistently across subsequent figures, and **Count** denotes the number of subcases with distinct flow conditions included under each main case.

Case	Dominant Flow Physics	Type	Symbol	Count
Pipe (Pirozzoli <i>et al.</i> [84])	ZPG	DNS	p	6
Square duct (Pirozzoli <i>et al.</i> [85], Modesti <i>et al.</i> [86])	Secondary	DNS	d	4
Channel with (spanwise) rotation (Andersson and Kristoffersen [87])	Rotation	DNS	r	7
TBLs subjected to mild APG (Hirt and Thomann [88])	PG	EXP	◻	1
TBL subjected to FPG followed by APG (Volino [89])	PG	EXP	▷	8
TBLs subjected to mild APG (Bobke <i>et al.</i> [90])	PG	WRLES	◦	5
TBLs subjected to FPG and APG (Gungor <i>et al.</i> [91, 92])	PG	DNS	g	3
Backward facing step (Driver and Seegmiller [93])	Separation	EXP	+	2
Pressure-induced separation bubble (Coleman <i>et al.</i> [94])	Separation	DNS	∩	3
Separation bubble with sweep (Coleman <i>et al.</i> [95])	Separation + 3D TBL	DNS		1
Converging-diverging channel (Marquillie <i>et al.</i> [96])	Separation + PG	DNS	◇	1
Axisymmetric separated boundary layer (Driver and Seegmiller [93])	Separation + PG	EXP	∪	1
Convex curvature boundary layer (Smits <i>et al.</i> [97])	Curvature + PG	EXP	∧	1
Concave bend (Barlow and Johnston [98])	Curvature + PG	EXP	<i>C</i>	1
Smooth ramp (Simmons <i>et al.</i> [99], Uzun and Malik [100])	Curvature + PG	EXP/DNS	◡	1
Curved boundary layer (Appelbaum <i>et al.</i> [101])	Curvature + PG	DNS	△	2
Gaussian bump ($Re_L = 1M$) (Uzun and Malik [102])	Curvature + PG	DNS	★	2
NACA 0012/4412 airfoils (Tanarro <i>et al.</i> [103])	Curvature + PG	DNS	n	2
Periodic hill (Balakumar and Park [104], Gloerfelt and Cinnella [105])	Curvature + PG	DNS	∪	1
Rounded Step (Bassi <i>et al.</i> [106])	Curvature + PG	DNS	□	1
A-airfoil near stall (Tamaki and Kawai [107])	Curvature + PG	WRLES	a	2
NASA wall-mounted hump (Uzun and Malik [108])	Curvature + PG	WRLES	◻	1
Laminar NACA0012 airfoil (Swanson and Langer [109])	Laminar + Curvature + PG	DNS	0	1
Transitional boundary layer (Roach [110])	Transition	EXP	✘	8
Transitional boundary layer (Lee [111])	Transition	DNS	+	1
35deg yawed wing (Van Den Berg <i>et al.</i> [112])	3D TBL	EXP	○	1
Laterally strained boundary layers (Pompeo <i>et al.</i> [113])	PG + 3D TBL	EXP	◁	3
3D TBL driven by a spinning cylinder (Driver and Hebbbar [114])	PG + 3D TBL	EXP	×	5
3D diffuser (Ohlsson <i>et al.</i> [115], Lehmkuhl <i>et al.</i> [116])	PG + 3D TBL	DNS	3	1

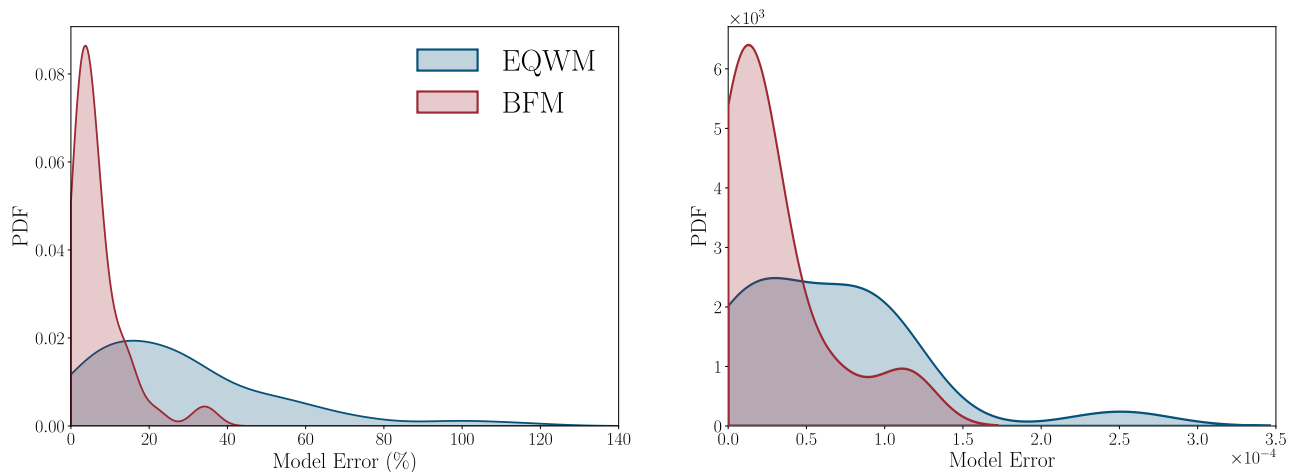


FIG. 9: *A priori* error distribution for BFM and EQWM for all cases considered. (a) Relative error (Eq. 11) for sample points far from incipient separation, i.e., $|u_{\tau, \text{true}}| \delta / \nu > 50$. (b) Dimensionless error (Eq. 12) for sample points close to incipient separation, i.e., $|u_{\tau, \text{true}}| \delta / \nu \leq 50$.

2. For *untrained cases*, BFM outperforms EQWM across all scenarios considered, as indicated by the symbols lying below the dashed line representing equal performance. For more than half of the cases, the error is reduced from above 40% to below 20%. From the chart summarizing the number of cases in each region (Figure 10a), we observe that more than 50% of the cases undergo major improvements.
3. An exception to the observations above occurs in three cases that favor EQWM—turbulent channel flow, turbulent pipe flow, and synthetic data generated from the law of the wall. These results are expected, as EQWM is specifically calibrated for these canonical flows. Nonetheless, the performance of BFM is only marginally worse, with errors remaining close to 1%.
4. *Underperforming cases* are identified in the right gray region, where BFM yields errors above 20%. Even so, BFM still significantly outperforms EQWM. These cases include the curved TBL by Appelbaum *et al.* [101], the transitional boundary layer by Roach [110], and the 3D TBL driven by a spinning cylinder by Driver and Hebbbar [114]. A detailed analysis of the potential causes of BFM underperformance in these cases is provided in the next section.
5. For *cases near separation*, BFM provides an order-of-magnitude improvement, with errors on the order of 10^{-5} compared to 10^{-4} for EQWM. This highlights the inaccuracy of EQWM near incipient separation and demonstrates the advantage offered by BFM.
6. For *laminar flows*, BFM also outperforms EQWM, with the latter exhibiting relative errors exceeding 100% in some instances. An exception is the Falkner–Skan laminar separation case, which is omitted from the plot because its relative errors are extremely large. The corresponding dimensionless errors are $\varepsilon = 5.12 \times 10^{-4}$ for EQWM and $\varepsilon = 3.2 \times 10^{-5}$ for BFM, demonstrating an order-of-magnitude improvement with BFM.

2. Detailed analysis for selected cases

We select five representative cases for detailed analysis. These include: (i) Falkner–Skan laminar flow, to compare model behavior in laminar regimes; (ii) a TBL subjected with mild pressure gradient, to examine sensitivity to pressure-gradient effects; (iii) square duct flow, to evaluate performance in flows with strong mean-flow three-dimensionality; (iv) the Aerospatiale A-airfoil, as a realistic high-Reynolds-number configuration; and (v) a two-dimensional Gaussian bump at $Re_L = 1,000,000$, to assess the ability of the model to handle relaminarization phenomena not present in the training database. In addition, we investigate the causes of underperformance of BFM in cases exhibiting relative errors greater than 20%, i.e., those falling within the gray region of Figure 10.

In the following analysis, we project the model error at each wall location and for all matching heights onto two of the three dimensionless inputs: $\Pi_1 = u_1 n_1 / \nu$ and $\Pi_3 = u_p n_1 / \nu$. As discussed in §II E, Π_1 represents a local near-wall Reynolds number, while Π_3 captures the influence of pressure-gradient effects. This projection therefore enables

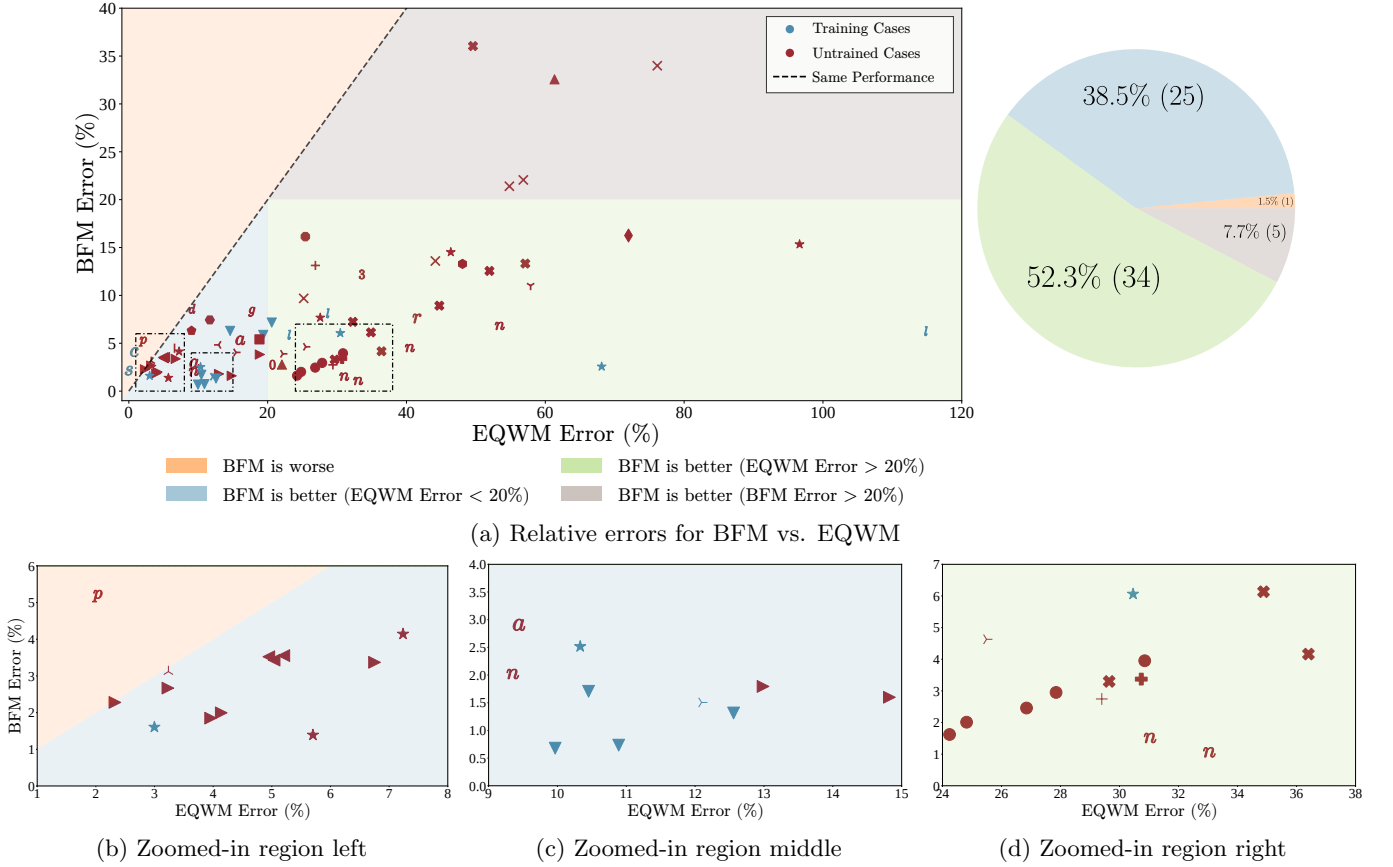


FIG. 10: (a) *A priori* relative errors (Eq. 11) of BFM versus EQWM for sample points far from incipient separation. Symbols follow the conventions defined in Tables II and III. Each symbol correspond to the mean error of a subcase in testing cases or training case. Cases with only change in Reynolds numbers are merged to fewer symbols to save space. Colored regions indicate the outcome categories described in the legend. The accompanying pie chart reports the percentage and number (in parentheses) of subcases falling within each category. Panels (b–d) show enlarged views of three regions with dense symbol overlap, highlighted by black dash-dotted boxes in the main plot for clarity.

a more granular assessment and facilitates interpretation of the error distribution as a function of local Reynolds number and pressure gradient. Each scatter point is color-coded by its relative error. Above each scatter plot, a relative frequency plot is provided to summarize the distribution of relative errors, ranging from 0% and capped at 100%. For cases containing samples with prediction errors above 100%, a small inset box reports the percentage of these outliers. For reference, EQWM results are also shown within the (Π_1, Π_3) input space, although EQWM formally depends only on Π_1 .

a. Falkner-Skan laminar boundary layer. Figure 12 shows the results for the laminar cases included in the BFM training set. As expected, EQWM—originally designed for turbulent flows—fails to generalize to laminar regimes. Its performance degrades substantially, with more than 60% of data points exhibiting prediction errors greater than 20%, and 6.3% exceeding 100% error. In contrast, BFM performs robustly: 96.2% of predictions fall within the 20% error threshold, and the vast majority lie below 5%.

Figure 13 shows the spatial distribution (streamwise and wall-normal) of the model error for one particular APG Falkner–Skan laminar boundary layer, providing a spatial perspective on the performance trends observed in Figure 12. Figure 13a indicates the sampling region. When the errors are visualized in physical space (Fig. 13b–13c), BFM performs well across the entire domain. In contrast, EQWM exhibits large errors both along the streamwise direction and across the wall-normal extent, consistent with the poor performance reported earlier.

b. TBL with mild APG. We now examine an APG TBL case that was not included in the training set. This configuration, introduced by Bobke *et al.* [90], corresponds to a TBL with a constant Clauser parameter of $\beta \approx 2$. The results are shown in Figure 14. Although Bobke *et al.* [90] reported that the inner-layer velocity profile approximately follows a logarithmic law, EQWM performs poorly: prediction errors exceed 10% across most of the profile and

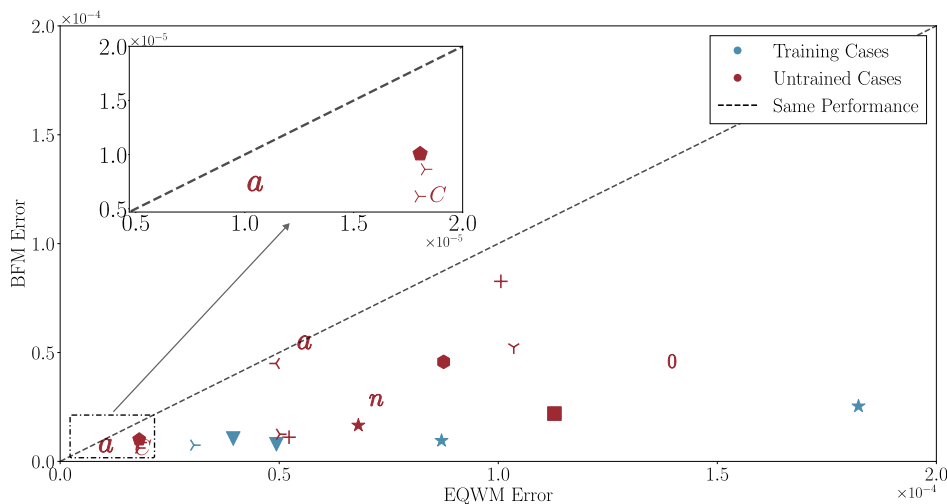


FIG. 11: *A priori* dimensionless errors (Eq. 12) of BFM versus EQWM for sample points near incipient separation. Symbols follow the conventions defined in Tables II and III. The inset provides a zoomed-in view of the region near the origin. One outlier—omitted from the main plot—corresponds to an APG Falkner–Skan laminar flow case, with $\varepsilon = 5.12 \times 10^{-4}$ and $\varepsilon = 3.2 \times 10^{-5}$ for EQWM and BFM, respectively.

reach more than 60% near the wall, particularly within the buffer region. In contrast, BFM maintains high accuracy even though the streamwise evolution of β in this mild APG case differs substantially from the training data (see Figure 35b). The accurate predictions of BFM extend across all wall-normal matching locations, including the buffer layer, with errors remaining below 10%. These results support the modeling assumption that history effects have limited influence on the wall-model predictions.

The spatial distribution of the model errors in Figure 15 offers additional insight. First, it confirms that the superior accuracy of BFM relative to EQWM is primarily localized in the near-wall region. Second, the plot shows a downstream improvement in BFM performance. This trend may be attributed to larger errors in the upstream region, where the boundary layer is thin—a condition that manifests as points clustered near the origin in the model-input space.

c. Square duct. This case tests the ability of the model to predict previously unseen secondary flows. We consider the DNS data of Pirozzoli *et al.* [85] at $Re_\tau = 220, 500, 1000$, and 2000. Whereas prior studies [85, 86] examined only the streamwise velocity, our objective here is to predict the *total* wall-shear-stress magnitude based on the magnitude of the wall-parallel velocity vector. This task is challenging because BFM was not trained on secondary flows or on cases exhibiting mean-flow three-dimensionality. Nonetheless, BFM performs accurately as shown in Figure 16. EQWM also yields small errors, which is expected given that the cross-flow components are weak relative to the dominant streamwise motion. Overall, both models perform well, showing only slightly larger errors than in a comparable turbulent channel flow without secondary motions.

The spatial error distribution, shown in Figure 17, reveals a clear trend for both models: prediction errors increase in proximity to the corners of the domain. This result is consistent with physical intuition, as the models, which are derived from 2D mean-flow assumptions, are expected to degrade where the 3D secondary motions are most intense. Despite this localized deterioration, the overall errors remain small. Furthermore, Pirozzoli *et al.* [85] demonstrated that the effect of this secondary motion diminishes as the Reynolds number increases. Since the current cases are at moderate Reynolds numbers, we hypothesize that the errors induced by the secondary flow would be mitigated even further at larger Reynolds numbers.

d. Aerospatiale A-airfoil near-stall. We further evaluate the models using a realistic, near-stall, high-Reynolds-number airfoil studied by Tamaki and Kawai [107]. The test case corresponds to an airfoil at a chord-based Reynolds number of $Re_c \sim 1 \times 10^7$ and an angle of attack of 13.3° , with solution data available at ten streamwise stations along the suction side. Because such flows lie far outside the low- to moderate- Re canonical regimes typically used for model development, they constitute a stringent test of model generalizability. Both BFM and EQWM achieve reasonable accuracy across all stations as shown in Figure 18. However, BFM shows a modest but clear advantage: a larger fraction of its predictions fall below the 20% error threshold, and none exceed 100% error, whereas EQWM exhibits a few outliers.

Figure 19 shows the mean relative error at each station and highlights the advantage of BFM. For EQWM, although the errors are small over the mid-chord region, they increase sharply near both the leading and trailing edges. In

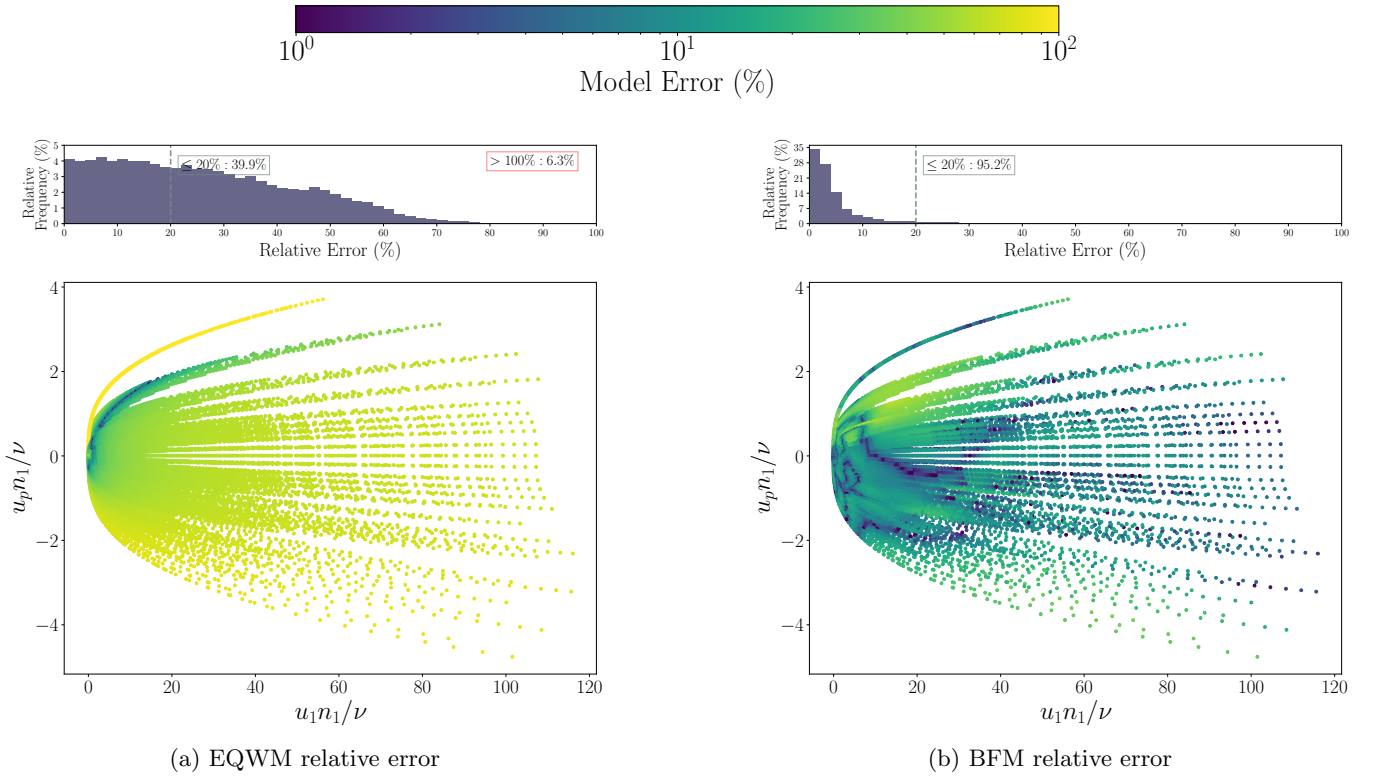


FIG. 12: *A priori* relative errors of (b) EQWM and (c) BFM for the Falkner-Skan laminar boundary layer, shown as a function of two BFM input variables.

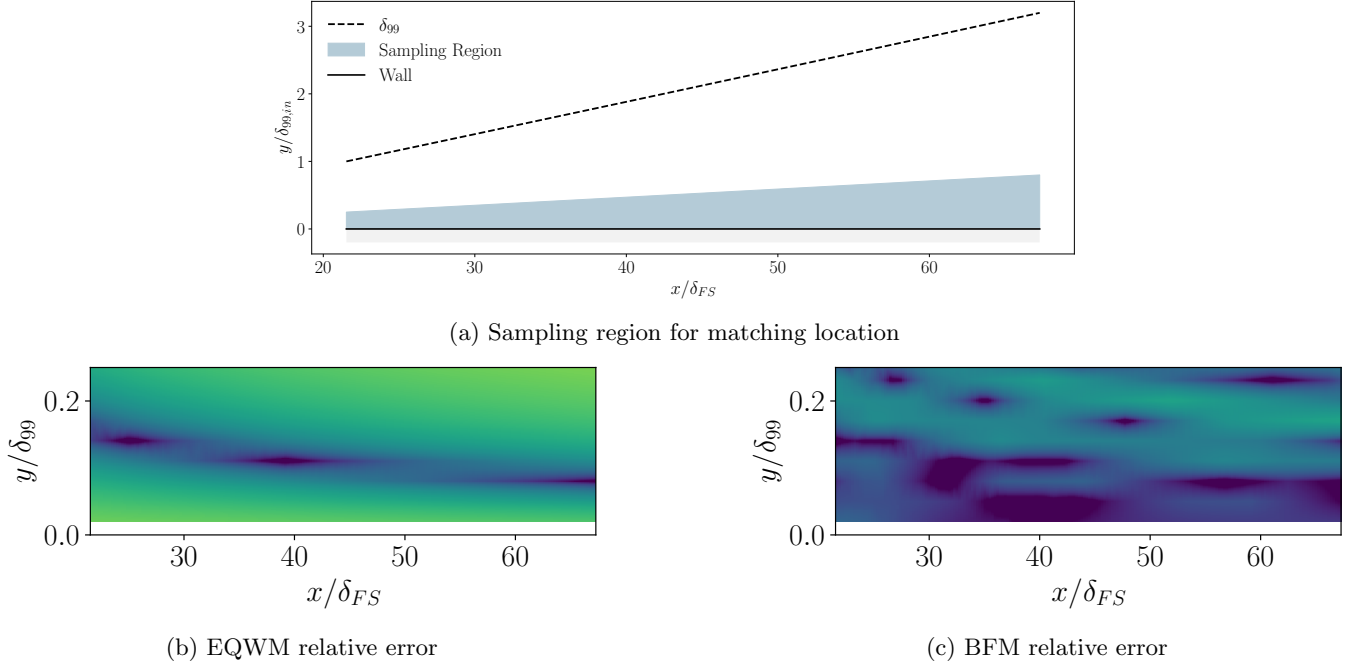


FIG. 13: *A priori* testing of an APG Falkner-Skan laminar boundary layer with edge velocity $U_e = Cx^{-0.05}$. (a) Sampling region (blue) used to select wall-model matching locations. Here, δ_{99} denotes the boundary-layer thickness based on 0.99 value of the freestream, $\delta_{99,in}$ its inlet value, and $\delta_{FS} = \sqrt{\nu/C} x^{(1-a)/2}$ the Falkner-Skan length scale.

(b) Spatial distribution of the EQWM relative error. (c) Spatial distribution of the BFM relative error. The colormaps in panels (b) and (c) are identical to those used in Figure 12.

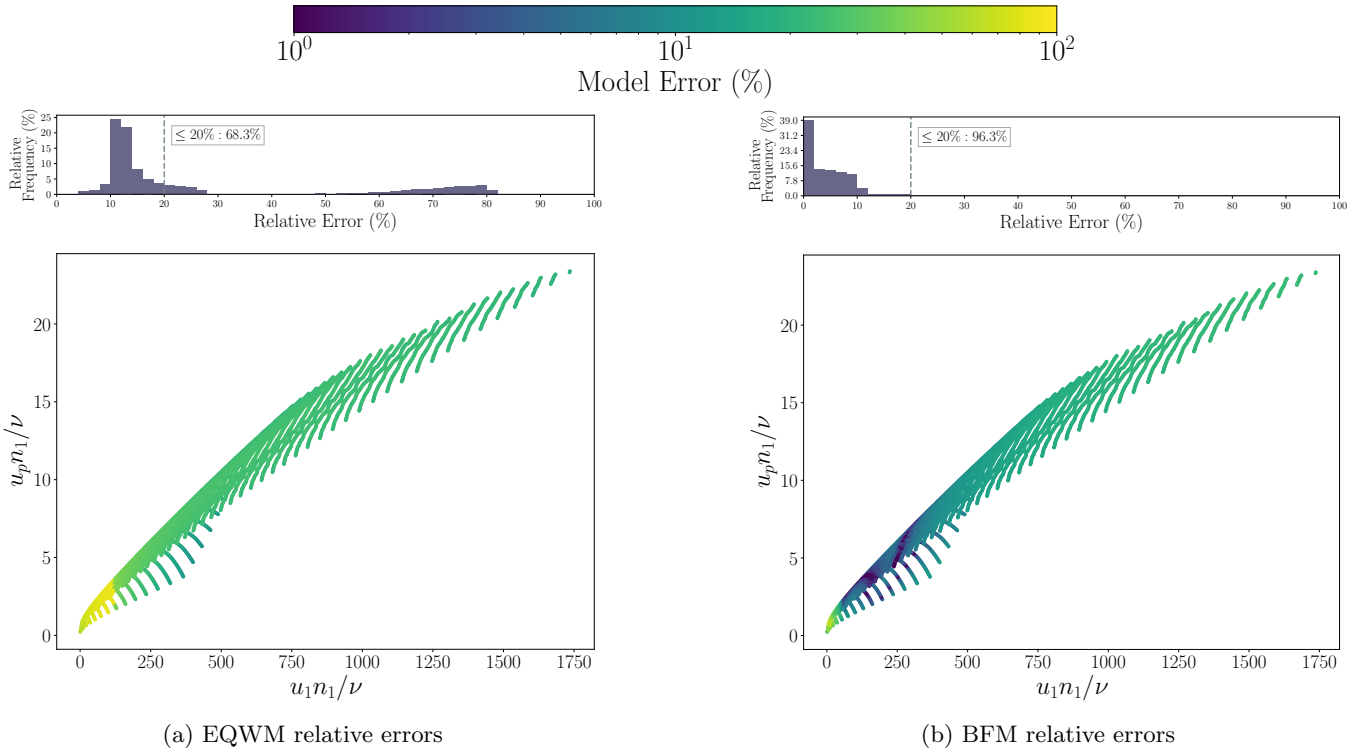


FIG. 14: *A priori* relative errors of (a) EQWM and (b) BFM for the APG TBL with constant $\beta \approx 2$ from Bobke *et al.* [90].

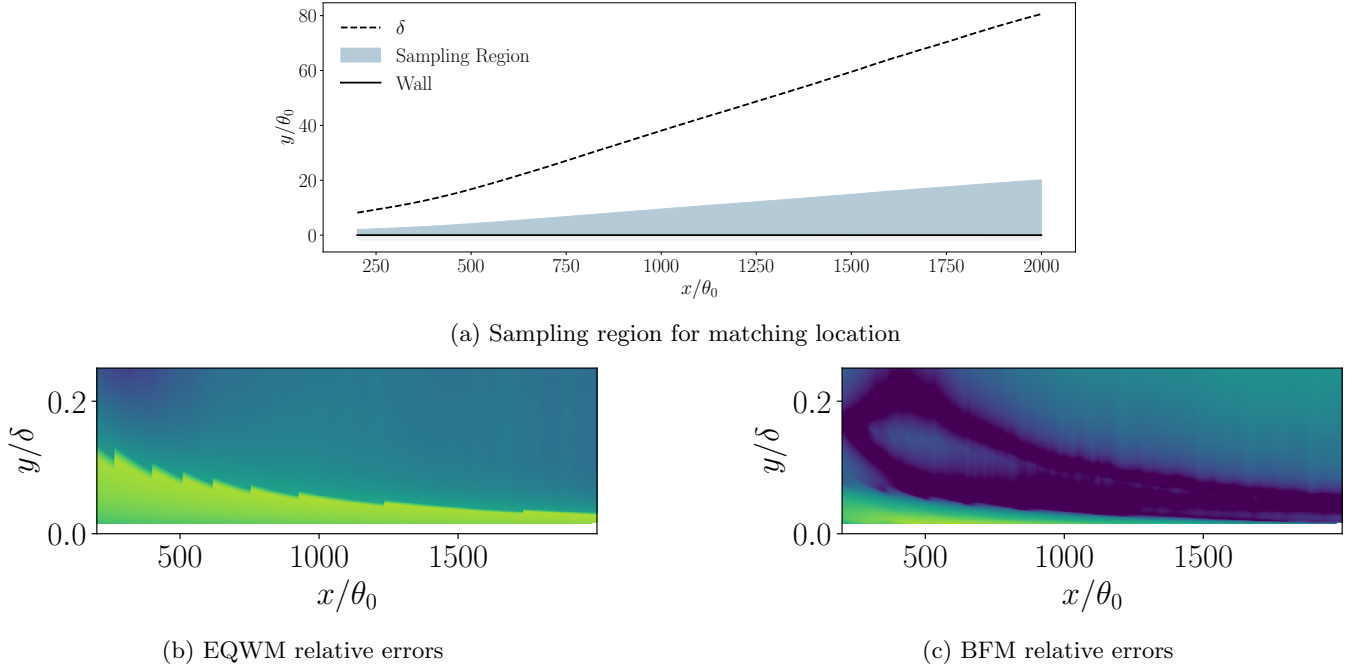


FIG. 15: *A priori* testing of a TBL with mild APG. (a) Sampling region (blue) used to select wall-model matching locations. Here, θ_0 denotes the inlet momentum thickness and δ the boundary-layer edge. (b) Spatial distribution of the EQWM relative error. (c) Spatial distribution of the BFM relative error. The colormaps in panels (b) and (c) are identical to those used in Figure 14.

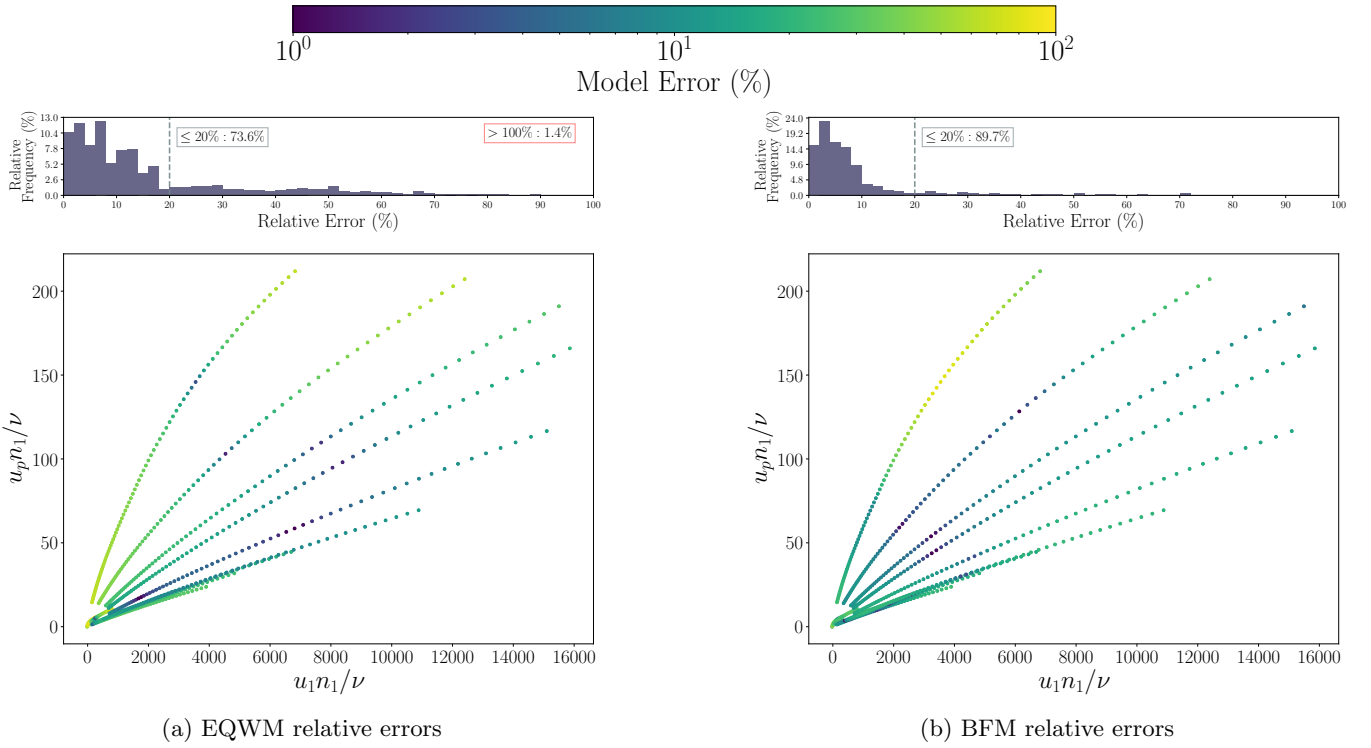


FIG. 18: *A priori* relative errors of (a) EQWM and (b) BFM for the Aerospatiale A-airfoil near-stall from Tamaki and Kawai [107].

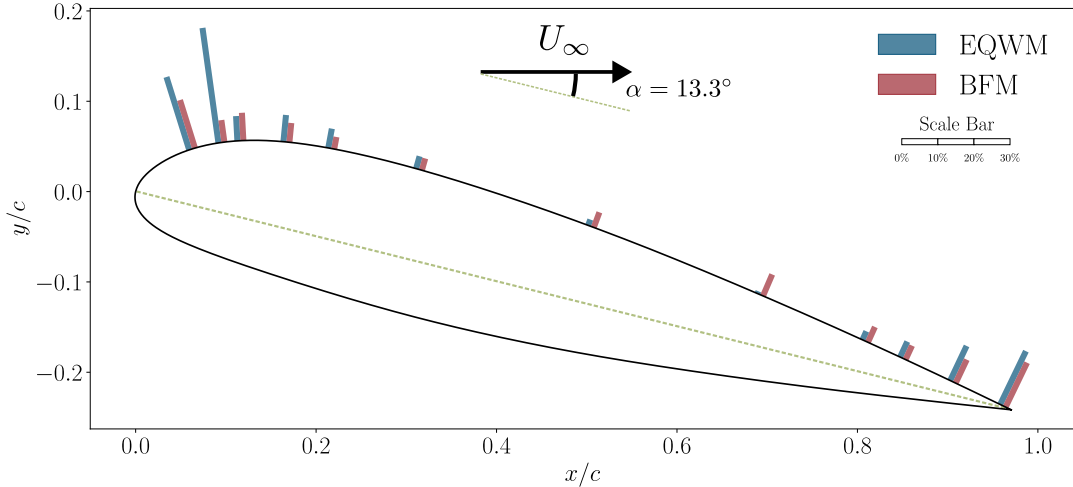


FIG. 19: *A priori* testing of the Aerospatiale A-airfoil at near-stall angle of attack. A comparison of mean errors at stations distributed at different locations of the suction side. Here, c is the chord length, U_∞ is the freestream velocity, and the dashed green line is the chord line. The length of bars is proportional to the model error as shown by the scale bar.

contrast, the errors from BFM remain lower across the chord. This behavior reflects the ability of BFM to handle the transition occurring at the leading edge—where EQWM breaks down—and to better predict the flow approaching separation near the trailing edge. While the errors of both models rise in the vicinity of separation, BFM remains more accurate, underscoring the benefits of its diverse training set.

e. 2D Gaussian bump ($Re_L \approx 1M$). We present results for a Gaussian bump case with a bump-length-based Reynolds number of $Re_L \approx 1 \times 10^6$, which was not included in our training data. This case differs fundamentally from

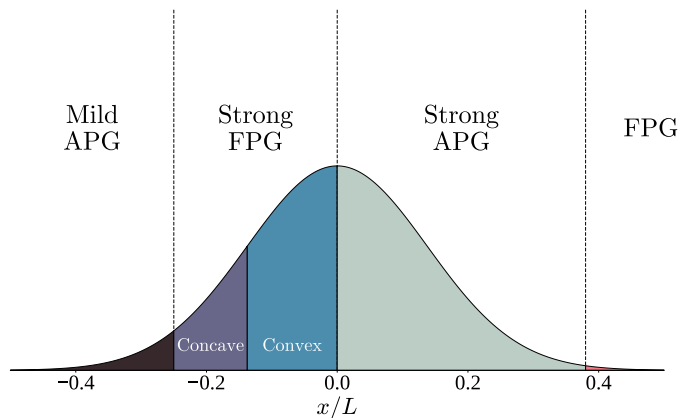


FIG. 20: Flow regimes for the Gaussian bump with $Re_L = 1M$ as a function of streamwise coordinates (x/L). From left to right: $x < -0.25$ (brown): mild APG; $-0.25 < x < -0.138$ (purple): strong FPG with concave surface; $-0.138 < x < 0$ (blue): strong FPG with convex surface; $0 < x < 0.38$ (green): strong APG; $x > 0.38$ (orange): FPG recovery zone.

the training case at $Re_L = 2 \times 10^6$ due to flow relaminarization near the apex, driven by low Reynolds number effects. As shown in Figure 20, the flow initially encounters a mild APG near the root of the bump, followed by a strong FPG. Near the apex, the combination of the convex surface and the FPG induces relaminarization. Downstream of the apex, the APG intensifies, triggering re-transition and pushing the flow to the verge of separation at $x/L \approx 0.2$. Finally, the flow experiences another FPG and approaches a ZPG state near the outflow.

In addition to these changes in pressure gradient behavior, the curvature effects in this case also differ from those in the training set. While the geometric curvature remains constant, the relevant dimensionless parameter, δ/R , varies significantly—primarily because the boundary layer becomes thinner as the Reynolds number increases at a fixed spatial location. Consequently, this case introduces new physical regimes and parameter ranges, providing a stringent out-of-sample test of the generalization capability of BFM. We focus our attention on the two most challenging regions: the strong FPG region with a convex surface and the strong APG region, as indicated in Figure 20. In the FPG region, partial relaminarization degrades the performance of EQWM, whereas BFM remains robust. In the APG region, BFM again significantly outperforms EQWM. However, even in this region, the BFM model shows clear room for improvement due to flow physics not represented in the training set. Specifically, the APG region begins in a partially laminar state and gradually transitions back to turbulence, which distinguishes it from a purely transitional flow where the pre-transition state is fully laminar.

The spatial error distributions in Figure 22 reinforce these observations. In the FPG region, the strong performance of BFM originates from its high near-wall accuracy, consistent with the behavior seen in earlier TBL cases. In the subsequent APG region, the performance of both models deteriorates; however, BFM remains noticeably more accurate. This outcome underscores that while BFM generalizes more effectively through the re-transition, the elevated errors also reflect the inherent difficulty of this case, where the transition begins from a partially laminar state rather than from a fully laminar boundary layer.

f. Underperforming cases. There are three main cases (or five if counting subcases) in which BFM, although outperforming EQWM, still exhibits large errors (i.e., relative errors above 20%). These cases correspond to the curved TBL studied by Appelbaum *et al.* [101], the transitional boundary layer reported by Roach [110], and the three-dimensional TBL induced by a spinning cylinder investigated by Driver and Hebbar [114].

In the first case (curved TBL), the observed errors are likely due to the limited exposure of the model to additional curvature effects during training. Figure 23 illustrates this data gap by showing the two-dimensional parameter space spanned by the friction Reynolds number (Re_τ) and the ratio of boundary-layer thickness to curvature radius (δ/R). The curved TBL case (blue) clearly occupies a region that is only partially represented by the training data incorporating curvature effects (red). This observation suggests the need for a more systematic expansion of the training set to better populate this portion of the parameter space.

For the second and third cases—both experimental—it is important to first acknowledge that measurement uncertainties can be significant. As reported by Driver and Hebbar [114], the friction coefficient alone may carry an uncertainty of up to $\pm 10\%$. Such errors may hinder our ability to evaluate the performance of BFM, as the observed discrepancies could largely stem from measurement noise rather than modeling deficiencies. In the transitional boundary-layer case, this interpretation is further supported by the DNS results of Lee [111], which exhibit much smaller errors for BFM. For the 3D TBL case, the relatively large discrepancies likely arise from two factors: the lack

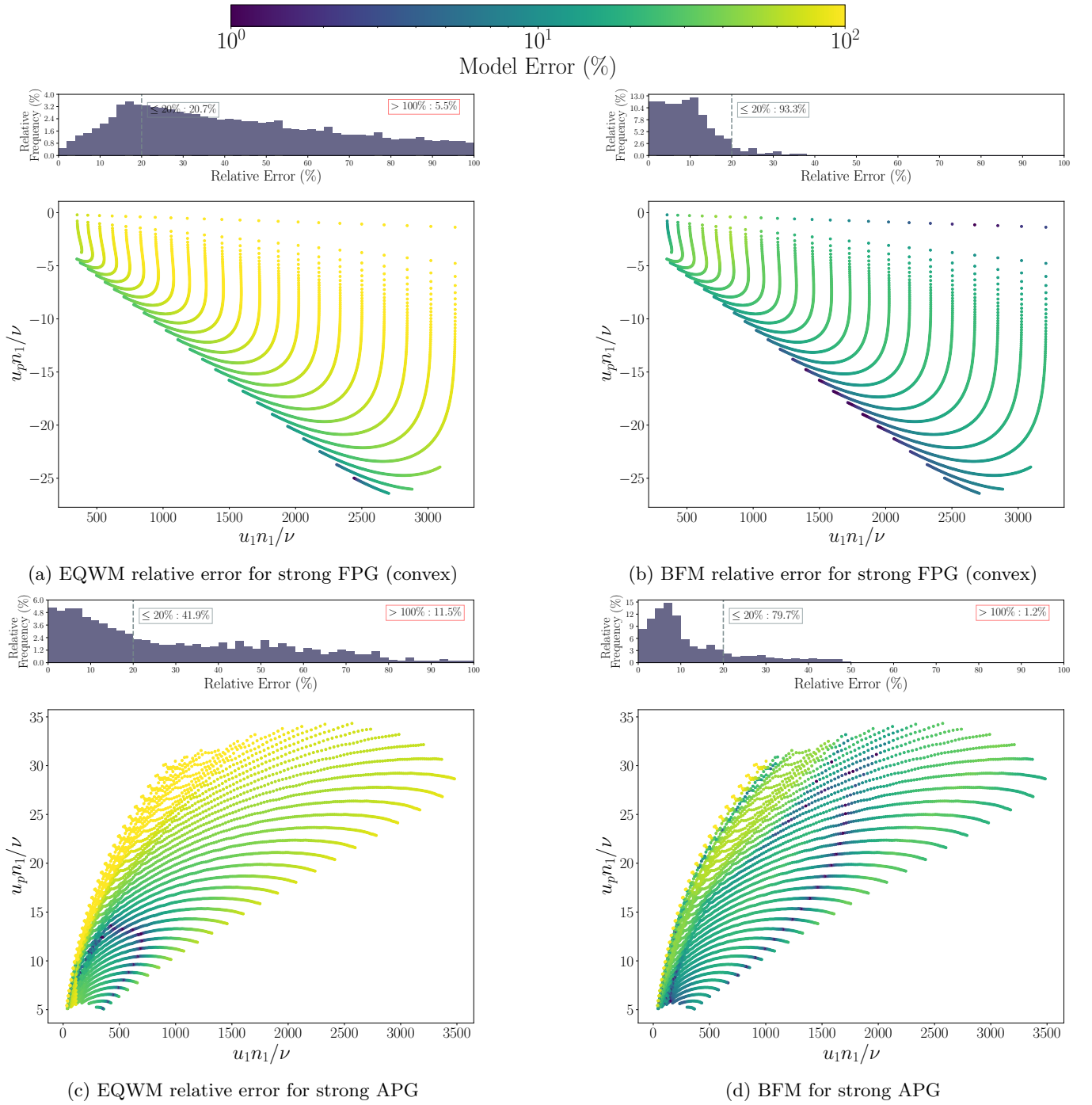
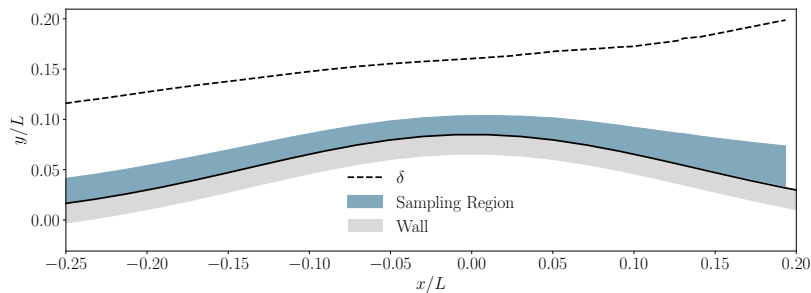
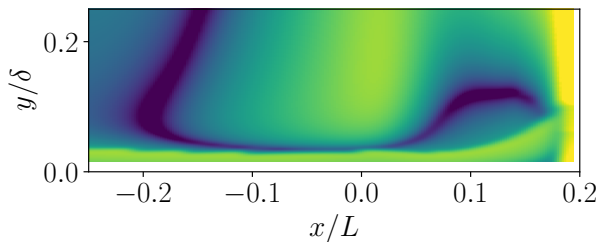


FIG. 21: *A priori* relative errors for (a) EQWM and (b) BFM in the strong FPG region with convex curvature of a 2D Gaussian bump at $Re_L = 1$ M, and for (c) EQWM and (d) BFM in the strong APG region. The two regions are delineated in Figure 20.

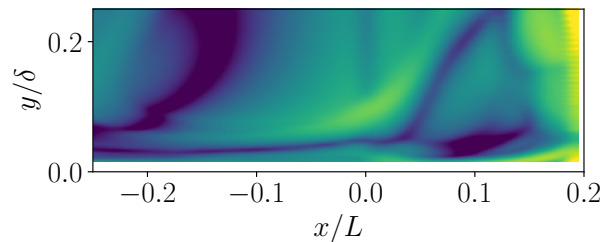
of training data with strong mean-flow three-dimensionality and the experimental uncertainties themselves.



(a) Sampling region for the matching location



(b) EQWM relative error



(c) BFM relative error

FIG. 22: *A priori* testing of a 2D Gaussian bump at $Re_L = 1M$. (a) Sampling region (blue) used to select wall-model matching locations. Here, L is the bump length and δ is the boundary layer edge. (b) Spatial distribution of the EQWM relative error. (c) Spatial distribution of the BFM relative error. The colormaps in panels (b) and (c) are identical to those used in Figure 20.

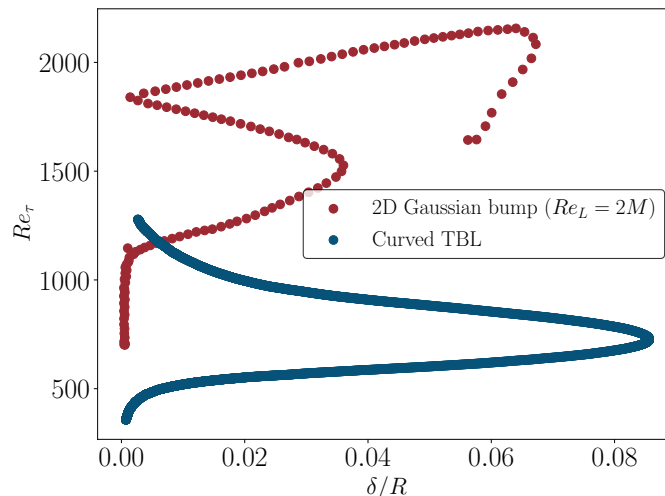


FIG. 23: Friction Reynolds number (Re_τ) versus the ratio of boundary layer thickness to curvature radius (δ/R) for training (Gaussian bump with $Re_L = 2M$) and testing case (curved TBL [101]).

B. *A posteriori* testing

We assess the BFM by conducting *a posteriori* WMLES under two complementary modalities: *nudged a posteriori* tests, which apply a forcing term to correct deviations of the mean velocity profile from the reference DNS solution, and *true a posteriori* tests, which expose the model to the full coupled LES/WM error without any external correction. The cases considered include: (i) turbulent channel flow; (ii) flat-plate turbulent boundary layers under adverse and favorable pressure gradients; (iii) a three-dimensional Gaussian bump to evaluate curvature-induced non-equilibrium effects; and (iv) a realistic aircraft geometry at multiple angles of attack. Cases (i) and (ii) are performed using nudged WMLES, whereas cases (iii) and (iv) are conducted as standard (unnudged) WMLES.

1. Nudged WMLES

The nudging method used for *a posteriori* testing is implemented by adding a corrective forcing term to the LES governing equations. For an incompressible flow, the nudged momentum equation takes the form

$$\frac{\partial \mathbf{u}}{\partial t} + \mathbf{u} \cdot \nabla \mathbf{u} = -\frac{1}{\rho} \nabla p + \nabla \cdot ((\nu + \nu_t) \mathbf{S}) + \mathbf{F}_{\text{nudging}}, \quad (14)$$

where $\mathbf{F}_{\text{nudging}}$ is the forcing term used to correct the mean velocity profile. We denote u , v , and w as the streamwise (x), wall-normal (y), and spanwise (z) velocity components, respectively. For a channel flow, the nudging term is $\mathbf{F}_{\text{nudging}} = [-\alpha(u_{\text{DNS}} - \langle u^{\text{obs}} \rangle_{xzt}), 0, 0]$, where u_{DNS} is the DNS mean velocity profile and $\langle u \rangle_{xzt}$ is the LES mean velocity profile averaged over the streamwise and spanwise directions and a period of time. For a turbulent boundary layer, the forcing becomes $\mathbf{F}_{\text{nudging}} = [-\alpha(u_{\text{DNS}} - \langle u \rangle_{zt}), 0, 0]$, where the only difference is that the LES velocity is no longer averaged in the streamwise direction due to streamwise inhomogeneity.

2. Flow solver

The BFM is implemented in the GPU-accelerated flow solver `charLES` (developed by Cadence, Inc.). The code is a finite-volume, second-order-accurate, compressible solver that employs a low-dissipation spatial discretization scheme, making it well suited for WMLES. A Voronoi-diagram-based meshing strategy is used to generate high-quality unstructured meshes. The solver has been extensively validated across a wide range of configurations [117–120].

An exponential time filter, similar to that proposed by Yang *et al.* [64], is applied to smooth the model inputs. The filter timescale is defined as $T_f = 100/\|\mathbf{S}_1\|$, where $\|\mathbf{S}_1\|$ is the magnitude of the rate-of-strain tensor at the first matching location. This value of T_f , used in all simulations reported below, is empirically chosen to suppress instantaneous oscillations in the pressure gradient that would otherwise degrade the accuracy of the wall model inputs. Further analysis of this choice is provided in Appendix C. Unless otherwise noted, the Vreman SGS model [121] is employed in all cases.

3. Computational cost

We assessed the computational cost of BFM on the MIT Satori cluster using two GPU nodes, each equipped with four NVIDIA V100 32GB GPUs (for a total of 8 GPUs). The cost of the wall model is a critical factor to consider, as excessive overhead could offset the potential benefits of using WMLES. Our results show that BFM offers inference costs comparable to EQWM. This efficiency is primarily enabled by a custom CUDA kernel that leverages shared memory for storing model weights. To quantify performance, we measured the total solver cost for 100,000 time steps (excluding solver initialization) using the Gaussian bump case described in §III B 4. The normalized solver speed was 0.0144 GPU-s/Mcv/step for EQWM and 0.0150 GPU-s/Mcv/step for BFM, where GPU-s, Mcv, and step denote GPU-seconds, million control volumes, and number of time steps, respectively. This represents only a 4% increase in total simulation time for BFM—an overhead that is well justified by its improved accuracy compared to EQWM.

4. Results

a. Turbulent channel flow. A canonical turbulent channel flow was simulated at a friction Reynolds number of $Re_\tau \approx 4,200$. The computational domain has dimensions of $(L_x, L_y, L_z) = (4\pi h, 2h, 2\pi h)$, where h is the half-channel height. A schematic of the domain is shown in Figure 24(a), with x , y , and z representing the streamwise, wall-normal, and spanwise directions, respectively. The flow is periodic in the streamwise and spanwise directions. A pressure gradient is applied in the streamwise direction to drive the flow.

Three cases are simulated using coarse ($\Delta/h = 0.2$), medium ($\Delta/h = 0.1$), and fine ($\Delta/h = 0.05$) isotropic grid resolutions, where Δ is the grid size. These resolutions are representative of practical external aerodynamics simulations, corresponding to approximately 5, 10 and 20 points per boundary layer, respectively [60, 117]. A sample of the fine isotropic grid is shown in Figure 24(b).

The mean profiles from the nudged WMLES, shown in Figure 25, demonstrate that the nudging scheme successfully corrects the mean profiles to match the DNS data. The predicted wall shear stresses for the three grid resolutions are summarized in Table IV. Consistent with our *a priori* analysis, both BFM and EQWM perform well for this case, with BFM exhibiting a slightly worse performance.

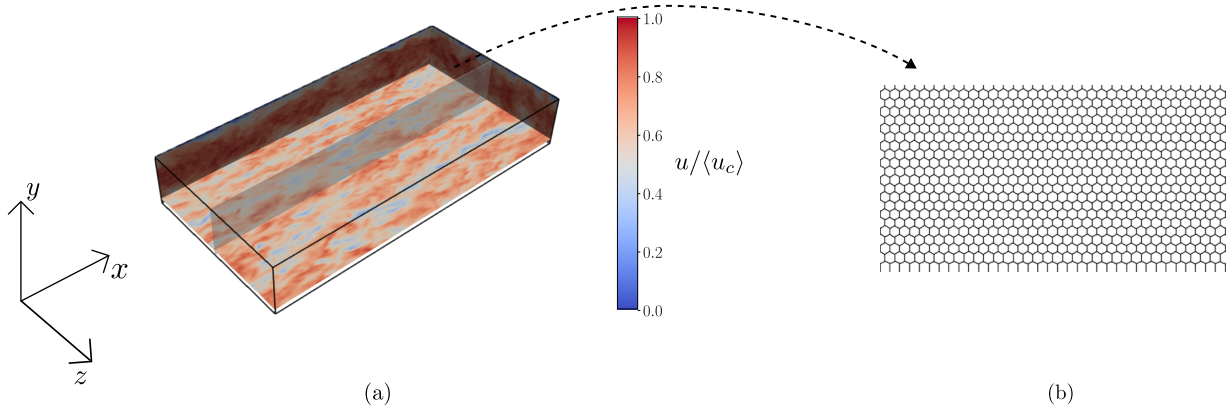


FIG. 24: (a) Schematic of the turbulent channel flow simulation. The quantity represented is the instantaneous streamwise velocity from *a posteriori* testing and normalized by mean centerline velocity at different planes. (b) A plane cut visualizing the fine computational grid ($\Delta/h = 0.05$).

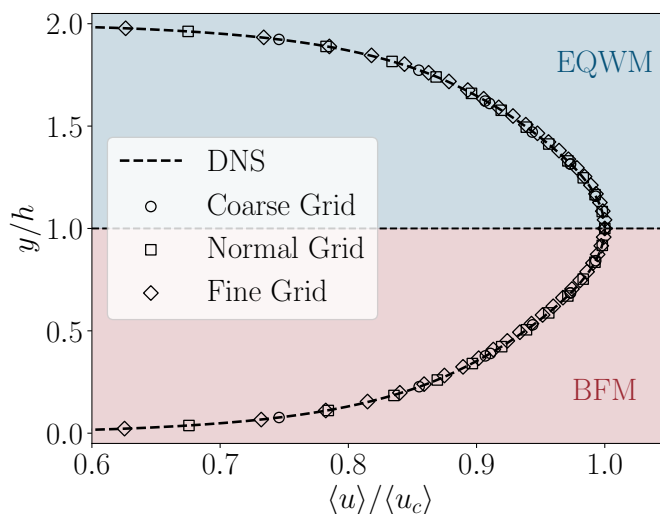


FIG. 25: Mean streamwise velocity profile $\langle u \rangle$ in *a posteriori* testing of a turbulent channel flow normalized by the mean centerline velocity $\langle u_c \rangle$ obtained using the EQWM (top half) and BFM (bottom half) simulated on coarse, medium and fine grids.

b. APG/FPG turbulent boundary layers. Turbulent boundary layers subjected to APG and FPG are evaluated through *a posteriori* testing. The geometry and boundary conditions exactly match those of the corresponding top-ramp TBL cases in the training database, featuring ramp angles of 5° for the APG case and -4° for the FPG case. The Reynolds number based on momentum thickness ranges from $Re_\theta = 670$ to 6,000 for the APG case and from $Re_\theta = 670$ to 1,000 for the FPG case, while the Clauser parameter spans $\beta = 0$ to 2 (APG) and $\beta = 0$ to -0.6 (FPG). WMLES is performed using grid resolutions corresponding to 5–40 points per boundary-layer thickness for

Grid Name	Δ/h	Grid points/ h	$\varepsilon_{\text{BFM}}\%$	$\varepsilon_{\text{EQWM}}\%$
Coarse	0.20	5	0.05%	1.12%
Medium	0.10	10	2.03%	1.03%
Fine	0.05	20	1.76%	0.84%

TABLE IV: *A posteriori* testing of BFM and EQWM in WMLES of a turbulent channel flow at three grid resolutions, defined by Δ/h , where h is the channel half-height. Errors are reported as percentages relative to the reference DNS solution.

the APG case and 5–15 points for the FPG case. The mesh used in the APG simulation is shown in Figure 26(a) and corresponds to the highlighted region in Figure 26(b). The total number of control volumes is 4.7 million for APG and 2.1 million for FPG.

We focus on the downstream region where the flow experiences adverse or favorable pressure-gradient effects. In both cases, the nudged WMLES accurately reproduces the mean velocity profiles at all streamwise stations, independent of the wall model used (Figures 27a and 28a). For the APG case (Figures 27b and 27c), WMLES with BFM maintains a relative error between 0% and 7% in predicting the friction coefficient across the entire domain, whereas EQWM exhibits noticeably larger errors, ranging from 10% to 18%. For the FPG case (Figure 28), both wall models provide accurate predictions of the wall-shear stress; EQWM errors fall between 0% and 4%, while BFM consistently achieves errors near 2% throughout the region considered.

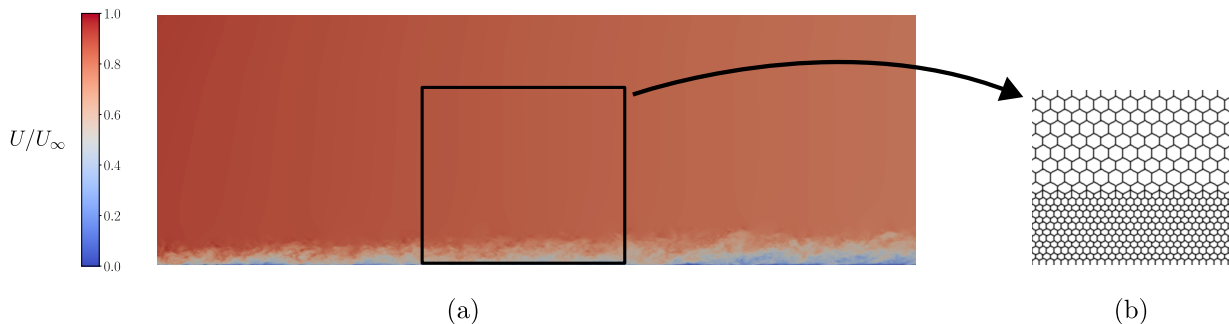


FIG. 26: (a) The contour plot of the normalized instantaneous streamwise velocity at the center plane of the computational domain for *a posteriori* testing of the APG case. (b) The grid in the black rectangular region shown in the left plot.

c. 3D Gaussian bump. The Gaussian bump considered here corresponds to the three-dimensional configuration tested experimentally by Gray *et al.* [122]. The flow in this geometry is highly three-dimensional—a feature not explicitly included in our training data, which only comprised a spanwise-periodic, 2-D Gaussian bump. Unlike the previous tests, this case is conducted as a *true a posteriori* evaluation, with no nudging applied to correct deviations in the mean profiles caused by suboptimal SGS model performance or deficient inflow conditions. As a result, the errors reported here include both internal and external wall modeling errors.

The geometry, shown in Figure 29a, is defined as $y(x, z) = h \cdot ((1 + \operatorname{erf}((L/2 - 2z_0 - |z|)/z_0))/2) \cdot \exp(-(x/x_0)^2)$, where $L = 0.9144$ m is the bump length, $x_0/L \approx 0.195$, $z_0/L = 0.06$, $h/L = 0.085$, and erf denotes the error function, which provides tapering in the spanwise direction. A two-dimensional cross-section of the computational grid is shown in Figure 29b, which employs three levels of isotropic refinement. The simulation comprises 28.96 million control volumes, providing approximately 10 points per boundary layer thickness at the bump apex. The Reynolds number based on the bump length is $Re_L = 3.41 \times 10^6$. The computational domain is a rectangular box extending from $-L$ to $1.5L$ in the streamwise direction (with the bump apex located at $x = 0$), from $-0.5L$ to $0.5L$ in the spanwise direction, and from 0 to $0.5L$ in the wall-normal direction. Boundary conditions are defined as follows: a constant, uniform inflow is imposed at the inlet; a non-reflecting characteristic boundary condition with constant pressure is applied at the outlet; and free-slip conditions are enforced at the lateral and top boundaries.

As shown in Figure 30, both BFM and EQWM perform poorly when coupled with the Vreman SGS model. The EQWM yields a very small separation bubble, while BFM predicts no separation at all. This poor performance—further evidenced by the highly inaccurate mean velocity profiles in Figure 31—highlights the critical importance of selecting an SGS model that minimizes external wall modeling errors. The combined effect of external and internal wall modeling errors leads to significantly degraded overall predictions.

Figure 30 also includes results obtained by coupling the current BFM (i.e., BFM-WM-v2) with BFM-SGS-v1 developed by Arranz *et al.* [53]. The comparison between SGS models (indicated in red and green) reveals a substantial improvement in the predictions of both pressure and friction coefficients when using BFM-SGS-v1. This improvement is primarily due to the enhanced accuracy of the mean velocity profiles, as shown in Figure 31, when the improved SGS model is employed. These results emphasize that reducing the external modeling error significantly enhances the performance of the wall model. In Appendix E, we also present results for BFM coupled with the dynamic Smagorinsky (DSM) SGS model, further illustrating the sensitivity of the *a posteriori* performance to the choice of SGS model.

Finally, for completeness, we compare the current BFM to its previous version BFM-WM-v1 coupled with BFM-SGS-v1 [53]. The BFM-SGS-v1 model was specifically designed to be used in tandem with BFM-WM-v1 to minimize

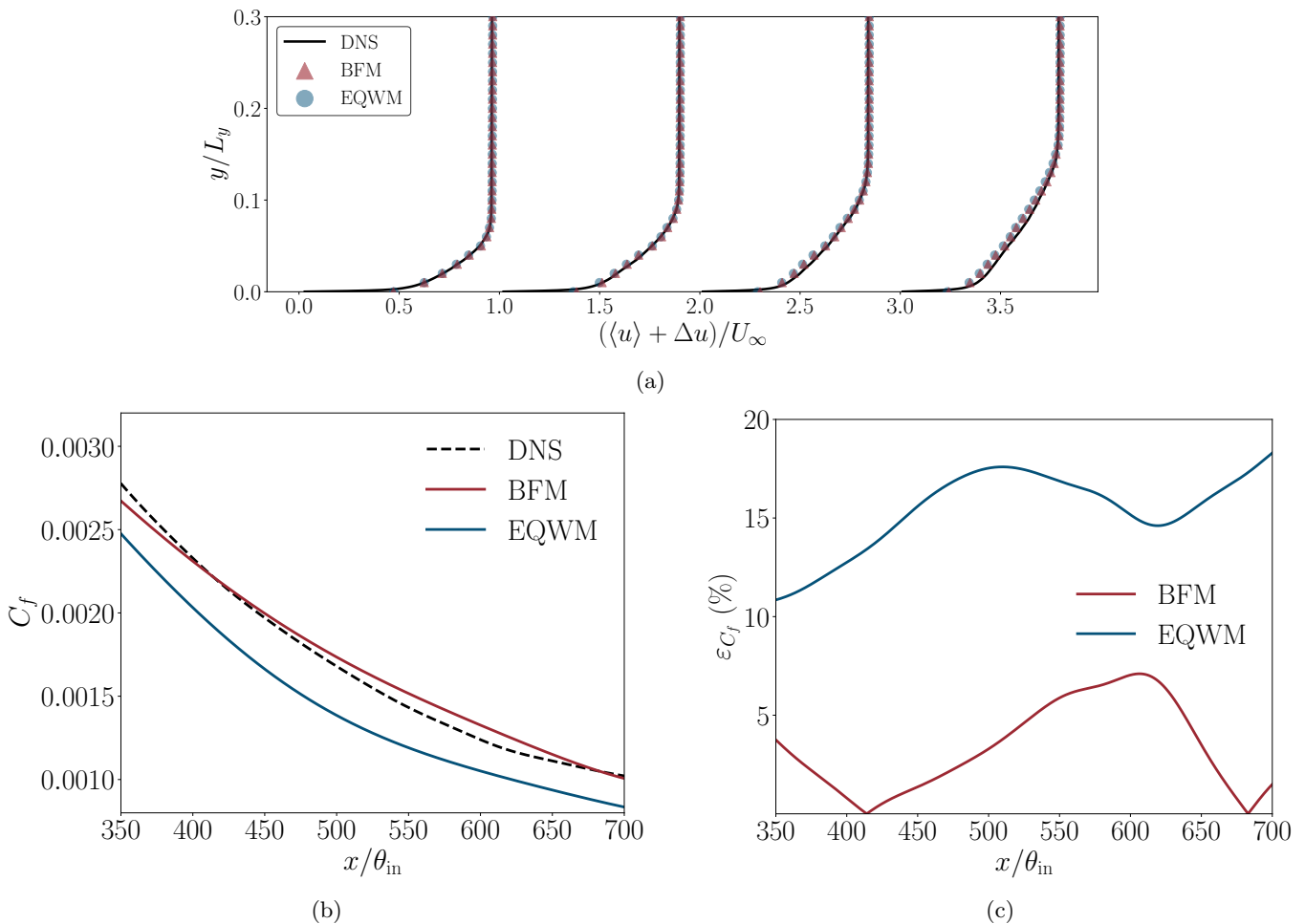


FIG. 27: *A posteriori* testing of BFM and EQWM in the WMLES of an APG TBL. The configuration corresponds to a turbulent boundary layer developing under a top ramp inclined at 5° . (a) Mean velocity profiles at four streamwise locations, $x/L_y = 3, 4, 5$, and 6 . Profiles are vertically shifted by $\Delta u/U_\infty = x/L_y - 3$ for clarity. (b) Streamwise distribution of the predicted skin-friction coefficient C_f . (c) Relative error

$$\varepsilon_{C_f} = (C_{f,\text{pred}} - C_{f,\text{DNS}})/C_{f,\text{DNS}}.$$

external modeling errors. In principle, this configuration should yield the lowest external error. However, as shown in the C_f predictions in Figure 30, the present BFM delivers improved accuracy on the upstream side of the bump. This improvement is attributed to the enhanced ability of the current version to reduce internal wall modeling errors compared to its predecessor. In conclusion, when coupled with an appropriate SGS model, the current data-driven wall model (BFM-WM-v2) provides superior performance.

d. NASA High-Lift Common Research Model. We evaluate the performance of the current BFM on the NASA High-Lift Common Research Model (CRM-HL), which served as the primary test case for the 5th High-Lift Prediction Workshop (HLPW5) [123]. This configuration is widely recognized as a highly challenging benchmark due to its complex geometry and the intricate flow physics encountered near the maximum lift condition. In particular, it poses significant challenges for WMLES, as previously noted by Kiris *et al.* [124]. The specific configuration considered here includes both a leading-edge slat and a trailing-edge flap, corresponding to case 2.3 of HLPW5. The geometry of the configuration is shown in Figure 32.

Following the computational setup of Goc *et al.* [118], the simulation is conducted at a freestream Mach number of 0.2 and a Reynolds number of 5.49×10^6 based on the mean aerodynamic chord. The geometry consists of a semi-span aircraft model placed within a large hemispherical domain with a radius 1,000 times the mean aerodynamic chord. A free-slip, no-penetration boundary condition is imposed on the symmetry plane. The inlet, defined as the front half of the hemisphere, features a uniform plug flow, while the outlet on the rear half employs a non-reflecting boundary condition with the freestream pressure specified. The simulation is performed with 35 million control volumes, with

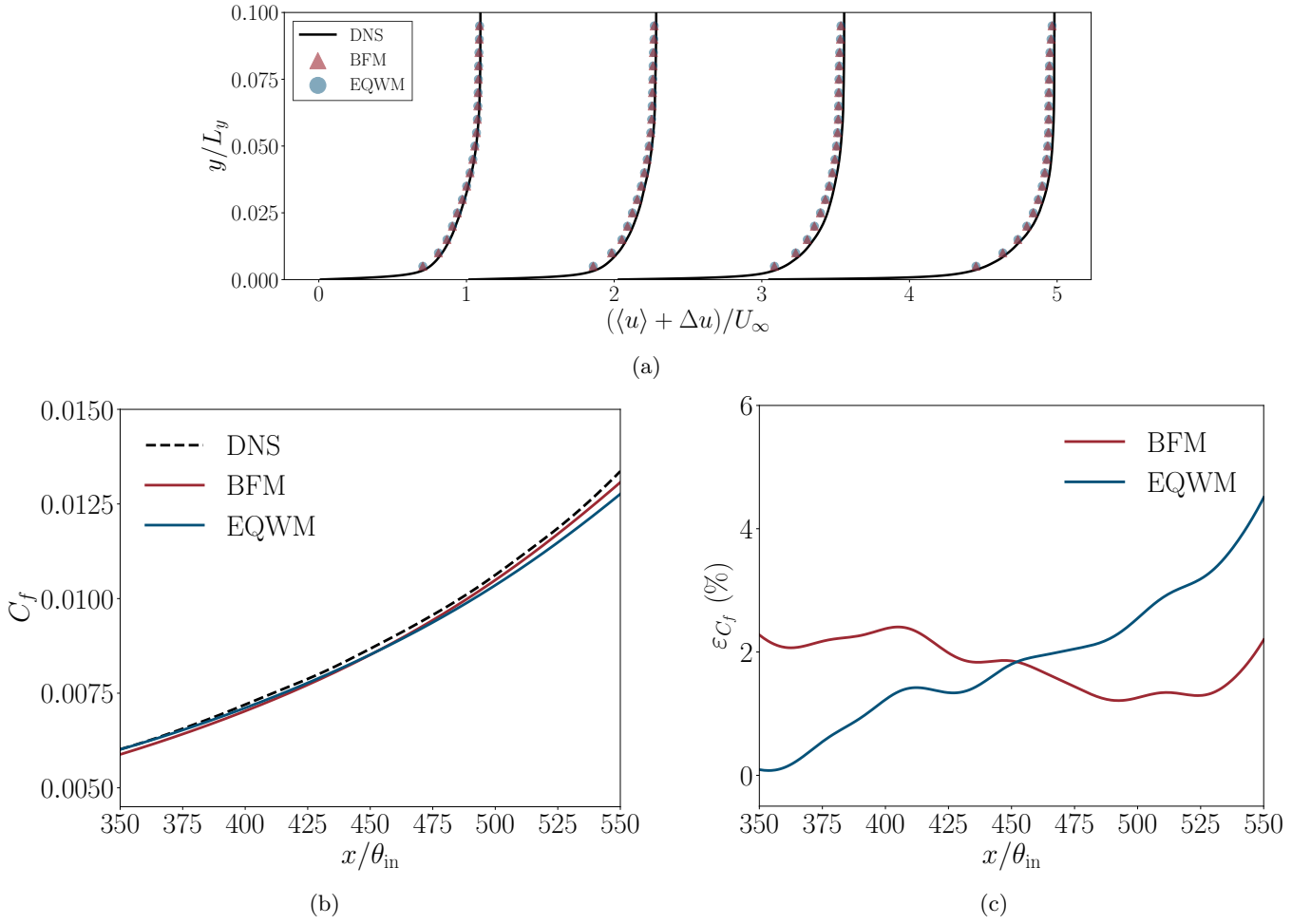


FIG. 28: *A posteriori* testing of BFM and EQWM in the WMLES of an FPG TBL. The configuration corresponds to a turbulent boundary layer developing under a top ramp inclined at -4° . (a) Mean velocity profiles at four streamwise locations, $x/L_y = 3, 4, 5$, and 6. Profiles are vertically shifted by $\Delta u/U_\infty = x/L_y - 3$ for clarity. (b) Streamwise distribution of the predicted skin-friction coefficient C_f . (c) Relative error $\varepsilon_{C_f} = |C_{f,\text{pred}} - C_{f,\text{DNS}}|/C_{f,\text{DNS}}$.

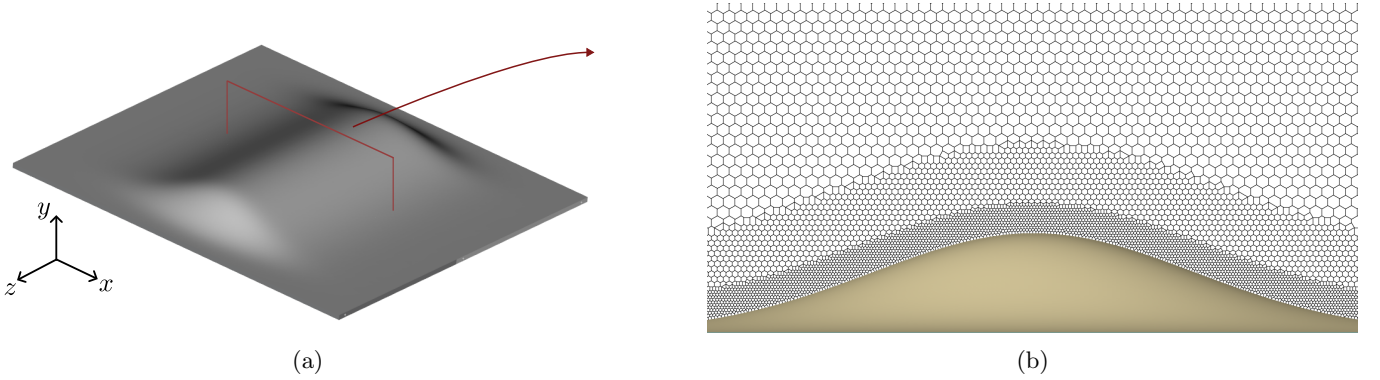


FIG. 29: (a) The geometry of the three-dimensional Gaussian bump case used by Gray *et al.* [122]. (b) A cut of the Voronoi grid used for *a posteriori* test.

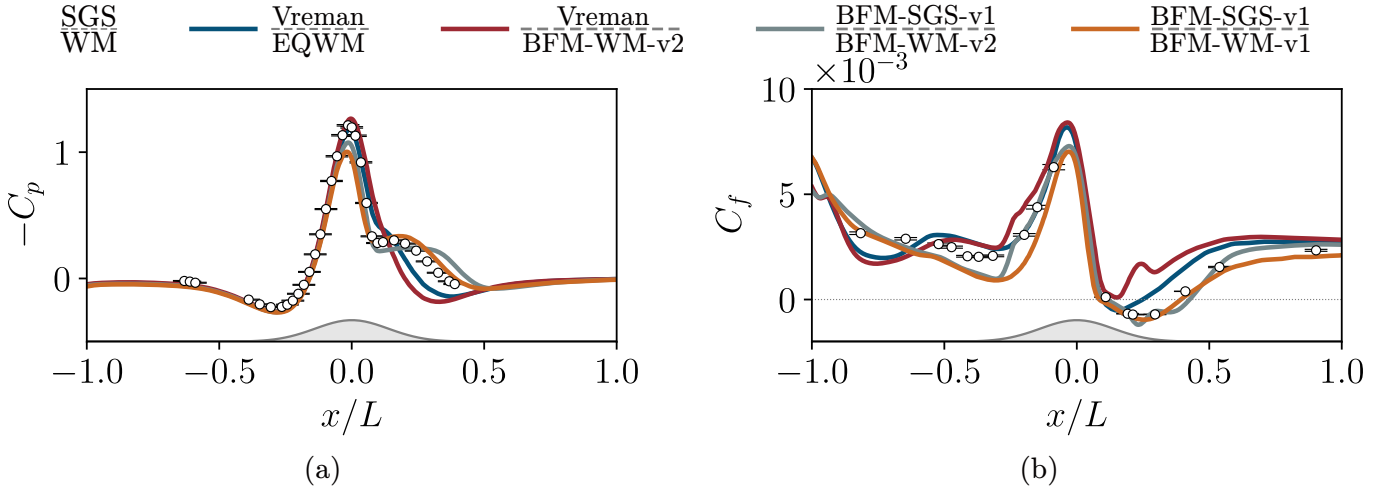


FIG. 30: *A posteriori* testing of BFM and EQWM in the WMLES of a Gaussian bump. (a) Pressure coefficient and (b) friction coefficient at the mid-span plane ($z/L = 0$). The blue and red lines correspond to EQWM and BFM coupled with the Vreman SGS model, respectively. The green line shows results from BFM coupled with the BFM-SGS-v1 model of Arranz *et al.* [53]. The orange line uses the same BFM-SGS-v1 model combined with the earlier BFM wall model (BFM-WM-v1) from Arranz *et al.* [53]. Experimental measurements from Gray *et al.* [122] are shown as black circles with error bars.

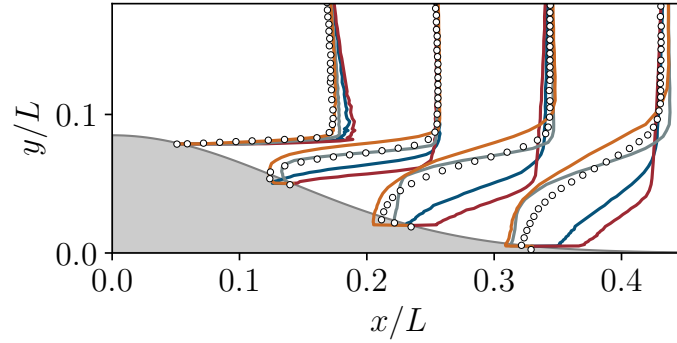


FIG. 31: Mean streamwise velocity profile at four stations downstream of the apex for *a posteriori* testing of the Gaussian bump. The colors of the line are the same as Figure 30.

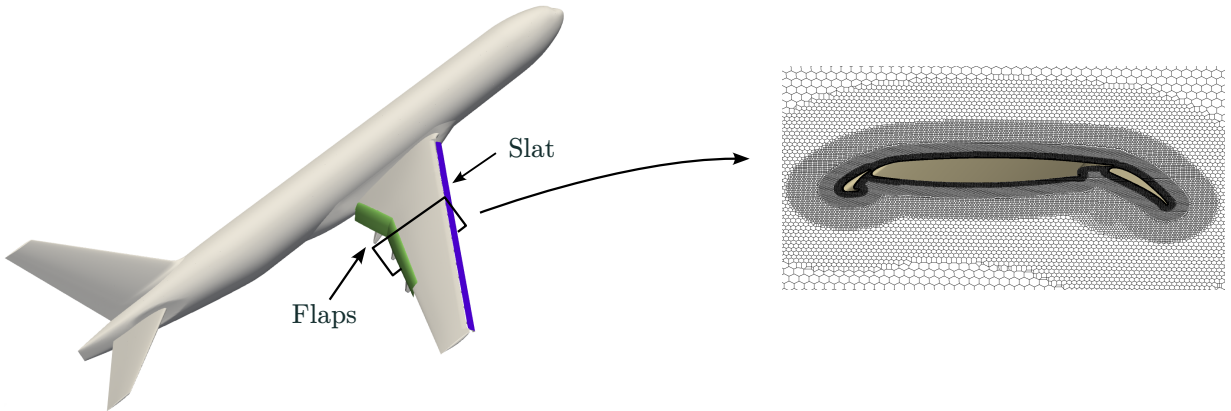


FIG. 32: Geometry of the CRM-HL test case 2.3. The leading-edge slat (purple) and trailing-edge flaps (green) are deployed, while the nacelle and pylons are omitted compared to the complete CRM-HL configuration.

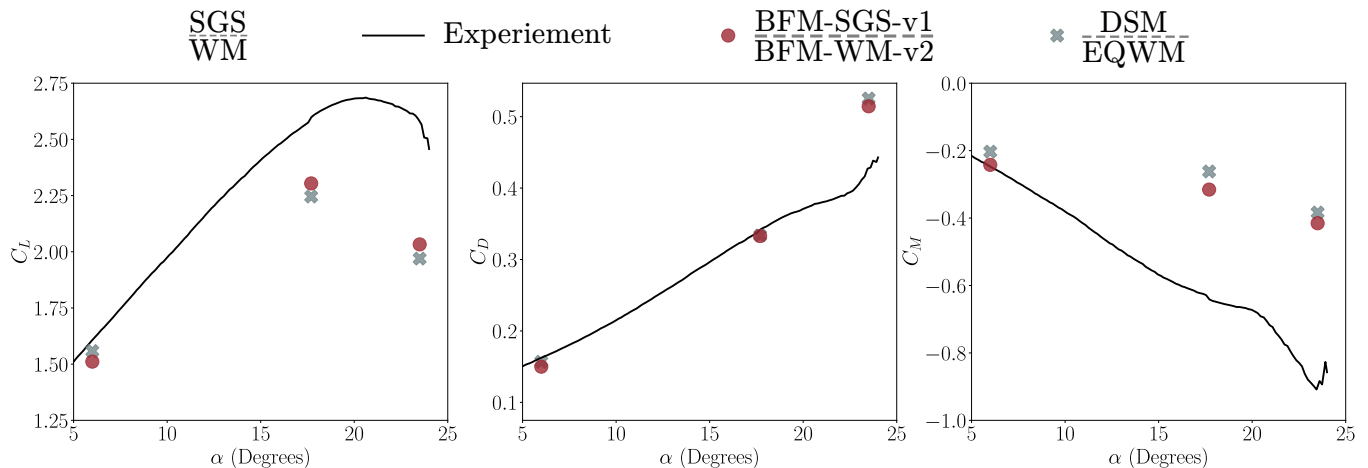


FIG. 33: *A posteriori* testing of the NASA High-Lift Common Research Model test case 2.3 using BFM and EQWM. (a) Lift (C_L); (b) Drag (C_D); (c) pitching moment (C_M) coefficients as a function of angle of attack α .

the minimum grid size $\Delta_{\min} \approx 0.002$ times the mean aerodynamic chord.

The quantities of interest are the integrated aerodynamic forces—specifically the lift (C_L), drag (C_D), and pitching moment (C_M) coefficients defined as

$$C_L = \frac{L}{\frac{1}{2}\rho_\infty U_\infty^2 S}, \quad C_D = \frac{D}{\frac{1}{2}\rho_\infty U_\infty^2 S}, \quad C_M = \frac{M}{\frac{1}{2}\rho_\infty U_\infty^2 S c}, \quad (15)$$

where ρ_∞ and U_∞ are the freestream density and velocity, L is the lift force, D is the drag force, M is the pitching moment, S is the wing area and c is the mean chord length.

The results are shown in Figure 33. The BFM model is evaluated at three angles of attack ($\alpha = 6^\circ$, 17.7° , and 23.5°). As expected, all models perform well in the linear regime at $\alpha = 6^\circ$. However, under near-stall and post-stall conditions, predictions from both BFM and EQWM deviate significantly from the reference data. Although not shown here, these discrepancies are primarily due to underprediction of flap separation and inaccurate modeling of leading-edge transition—phenomena that are well known to be challenging for conventional approaches [124]. While the BFM approach offers a avenue for improving predictions in such complex flow regimes, the present case is likely dominated by wall-modeling errors external to the BFM itself. Future tests will be conducted using BFM combined with BFM-SGS-v2.

IV. DISCUSSION

A. Model Limitations

We outline the primary limitations of BFM-WM-v2 along with potential directions for improvement:

- *Dependence on the building-block-flow assumption:* The core assumption underlying BFM is that a finite set of canonical flows (referred to as building-block flows) can encapsulate the essential near-wall physics necessary for generalizable wall modeling. While this approach provides a structured foundation for data-driven modeling, its validity may be limited in cases involving separation patterns or flow regimes not present in the training data. Two scenarios of this limitation are presented in the following points.
- *Transitional flow regimes:* Although the model performs well for laminar and transitional regimes in controlled *a priori* settings, it was not trained on a comprehensive set of flows capturing laminar-to-turbulent transition dynamics. Incorporating such cases is nontrivial, as it may introduce numerical instabilities, trigger premature transition, and hinder the model to revert to laminar states.
- *Flows with mean-flow three-dimensionality:* The current model predicts only the magnitude of the wall-shear stress, assuming alignment between the stress vector $\boldsymbol{\tau}_w$ and the velocity vector at the first off-wall grid point, \mathbf{u}_1 . This assumption is justified for high Reynolds numbers and typical WMLES resolutions, where the two vectors

remain aligned on average [13]. However, in boundary layers with strong mean-flow three-dimensionality, this assumption breaks down [125], leading to misalignment and inaccurate predictions. Addressing this limitation would require both restructured model inputs and the inclusion of richer three-dimensional datasets, which are currently sparse and difficult to balance relative to two-dimensional cases.

- *Local-state sufficiency assumption:* The model relies exclusively on local flow quantities as input, under the premise that the near-wall region attains a quasi-equilibrium state [63]. While this design choice enhances generalizability to complex geometries, it limits the ability of the model to capture long-range interactions or unsteady effects. Prior work on turbulence forecasting has demonstrated that incorporating temporal history can substantially improve predictive accuracy [126–128].
- *Training on ensemble-averaged inputs:* BFM is trained using ensemble-averaged quantities from DNS, rather than instantaneous flow fields. This design choice simplifies training, avoids underfitting with high-dimensional fluctuating data [42], and facilitates broader dataset inclusion. During inference, a temporal averaging filter is applied to approximate these conditions [1, 64]. However, this restricts the model from accurately predicting instantaneous wall-shear stress and may lead to degraded performance in statistically unsteady regimes.
- *Sensitivity to SGS model:* A key limitation identified in our study is the strong dependence of wall-model performance on the choice of SGS model. Errors introduced by underperforming SGS models (i.e., external wall-model errors) were found to be the dominant source of inaccuracy. This challenge was first discussed in detail during the development of BFM-WM-v1 [1], where the need for a unified wall/SGS modeling framework was highlighted. Our group has advanced this direction through the development of BFM-v1, a consistent framework that includes both an SGS model (BFM-SGS-v1) and a wall model (BFM-WM-v1) designed to operate in tandem [53]. Building on this foundation, Ling and Lozano-Durán [83] proposed a strategy for developing numerically consistent SGS models by enforcing compatibility with a pre-trained wall model. The method generates a training dataset via nudged WMLES, ensuring that the SGS model learns from flow fields already aligned with the wall model. Importantly, the procedure makes no assumptions about the internal structure of the wall model, allowing the resulting SGS model to be integrated seamlessly. Once deployed, such an SGS model is expected to substantially improve *a posteriori* performance when coupled with the original wall model.

B. Outlook for future versions

We conclude by outlining the main directions for improving future versions of the Building-Block Flow Model wall model. The current approach primarily relies on a database of pressure-gradient turbulent boundary layers. While this foundation has proven effective, extending the database and refining the formulation are essential for broader applicability and improved accuracy. Below we discuss the most relevant avenues for future development.

- *Turbulence with mean-flow three-dimensionality.* A critical next step involves extending the model and database to include flows with mean three-dimensionality. Current datasets capture only quasi-two-dimensional physics, while boundary layers subjected to lateral pressure gradients exhibit complex shear-stress misalignment effects [13]. Existing databases of 3D channel flows with imposed spanwise pressure gradients [13] provide a useful starting point, but an ideal solution would be a new parametric dataset—analogue to the PG TBL series—spanning varying spanwise pressure gradients. Capturing these effects requires two key model modifications: (i) including the wall-parallel velocity-vector orientation as part of the model input, and (ii) extending the model output to predict both components of the wall-shear-stress vector instead of only its magnitude. With these changes, retraining on suitably enriched datasets would allow the model to generalize to flows with inherent three-dimensionality.
- *Wall-curvature effects.* Another major extension concerns the inclusion of wall-curvature effects through a richer collection of training cases. The current version was trained only on a single Gaussian-bump configuration. New databases are being generated to include TBLs under adverse and favorable pressure gradients over curved surfaces. Such an expansion is crucial because, in practical flows, curvature and pressure-gradient effects often appear simultaneously. Although parametric studies exist for curved turbulent channels [129, 130], no equivalent systematic dataset exists for TBLs combining both effects. Creating such a dataset remains a primary objective for future work.
- *Laminar-to-turbulent transition.* Accurately modeling transitional flows requires mechanisms for automatically switching between laminar and turbulent regimes. Developing reliable flow-state sensors for this purpose is an

ongoing challenge. Existing sensor-based approaches [28, 131] provide promising foundations, but more advanced or data-driven detection techniques will likely be needed to ensure robust performance across a wide range of Reynolds numbers and flow configurations.

- *Compressible-flow extension.* The building-block modeling approach can be naturally extended to compressible regimes. Our group has successfully applied similar methodologies to high-speed flows [50]. Adapting the current model to compressibility will require modifications to account for variable density, temperature, and acoustic effects. The main limitation, however, is the scarcity of high-fidelity training and validation datasets for compressible wall-bounded turbulence, which remains a bottleneck for data-driven approaches.
- *Wall-roughness effects.* Incorporating the influence of wall roughness represents another important direction. Extending the model to account for subgrid-scale roughness elements would enable prediction of friction and heat-transfer modifications induced by surface texture, a critical capability for realistic aerodynamic and environmental applications. We have applied the building-block flow model approach to develop wall models for rough surfaces [50, 62], although these studies assume isotropic roughness under equilibrium conditions.
- *Numerical consistency with the SGS model.* As discussed above, the current BFM exhibits sensitivity to the choice of SGS model. Developing an SGS model that is both numerically and physically consistent with BFM would help mitigate the external modeling errors identified in the *a posteriori* tests. A unified wall/SGS framework is expected to deliver more stable and accurate WMLES predictions across a broad range of flow conditions.
- *Continual learning and adaptive grid refinement.* Beyond expanding the physical database, continual-learning strategies [132] offer pathway for targeted model improvement. This approach allows retraining on new, specialized datasets without degrading performance on previously learned cases. It is particularly valuable for proprietary or complex datasets that cannot be publicly released. Continual learning enables users to fine-tune the base model to specific flow regimes—e.g., pressure-gradient ranges or Mach numbers—while preserving its general predictive capability. This strategy bridges the gap between generalizability and case-specific optimization.

V. CONCLUSIONS

We have introduced a general-purpose wall model for LES grounded in the building-block flow modeling approach. The method leverages the hypothesis that the essential near-wall physics in complex turbulent flows can be locally represented using a finite set of canonical, simplified flows—termed building-block flows. Rather than constructing a model that memorizes case-specific behaviors, the goal of BFM is to learn the underlying flow physics and achieve generalizability across a wide spectrum of geometries and flow regimes. The resulting wall model is designed to handle a variety of physical scenarios, including laminar and turbulent flows, adverse and favorable pressure gradients, wall curvature, and flow separation. By focusing on extracting essential flow physical, the model traces a patchway to depart from case-tuned equilibrium models.

The current version of the model, referred to as BFM-WM-v2, builds on our prior work (BFM-v1), which established the feasibility of constructing generalizable wall and SGS models using the building-block flow assumption [1, 53]. In BFM-v1, the wall model (BFM-WM-v1) and SGS model (BFM-SGS-v1) were developed jointly and demonstrated strong performance across a range of canonical and complex geometries. In this work, we develop the second-generation wall model for BFM-v2 to address the limitations in predictive accuracy observed in off-training-distribution flows. The improvements in BFM-WM-v2 are driven by insights gained from BFM-v1 and include a more comprehensive training database, an improved input–output design, balanced training via a weighted loss, and a substantially expanded test suite for model validation.

The model formulation uses a feedforward artificial neural network trained to predict the magnitude of the wall-shear-stress vector from localized near-wall flow features. All inputs and outputs are expressed in dimensionless form, ensuring physical invariance under units transformations. To identify the optimal input variables, we employ the Information-Theoretic Buckingham- π method, which systematically selects the most informative dimensionless variables based on the irreducible model error. This procedure yields a compact and physically interpretable input set consisting of local velocities and wall-normal distances, without requiring wall-normal gradients or non-local flow information. The training dataset contains over one million samples extracted from 67 building-block cases, including turbulent channels, pressure-gradient boundary layers, laminar Falkner–Skan flows, Gaussian bumps, and separation bubbles. To balance contributions across cases, sample weights are assigned based on inverse data frequency, and a weighted relative Huber loss is used during training to mitigate the influence of outliers. The final model is

trained using a four-layer ANN architecture with strong regularization and early stopping criteria to ensure robust generalization.

We evaluated the model across a comprehensive suite of validation cases, distinguishing between internal errors—those intrinsic to the wall model formulation—and external errors—those arising from the surrounding LES environment, especially SGS model inaccuracies. This distinction enables a more precise understanding of the performance of the model and its limitations in practical WMLES settings. Internal errors reflect limitations in the physical coverage of the training dataset or modeling assumptions, while external errors include imperfections in boundary conditions and incorrect SGS modeling. This decomposition of errors is central to our evaluation methodology, as it clarifies whether observed discrepancies stem from the wall model or from deficiencies elsewhere in the simulation pipeline. We report results across a rich collection of 140 high-fidelity testing cases (67 training cases included), including experimental and high-fidelity numerical data. The cases range from canonical internal flows to highly three-dimensional, curved, separated, and transitional flows in realistic geometries such as airfoils and swept wings.

In the *a priori* testing, which isolate wall-model performance using direct input-output data from high-fidelity sources, the BFM-WM-v2 consistently outperformed the EQWM across nearly all cases. These tests covered flows with varying Reynolds numbers, pressure gradients, wall curvature, and laminar configurations. Even for cases well outside the training distribution—such as Gaussian bumps at moderate Reynolds numbers with relaminarization, or three-dimensional spinning-cylinder boundary layers—the model maintained reasonable predictive accuracy. The overall relative error across the test sets was reduced substantially compared to EQWM, often by more than 50%. Particularly notable was the accuracy of BFM-WM-v2 in the vicinity of incipient separation, where EQWM typically fails due to its strong equilibrium assumptions. In contrast, BFM-WM-v2 leveraged its non-equilibrium training data to maintain accurate predictions down to low wall-shear stress magnitudes. The *a priori* analysis also revealed that BFM-WM-v2 is robust to variations in the matching location, capturing the correct trend even in buffer-layer and logarithmic-layer inputs.

The *a posteriori* evaluation assessed the model performance within a full WMLES environment, thus accounting for the compounded effects of SGS modeling, grid resolution, and numerical discretization. We conducted both *nudged* and *true a posteriori* simulations. In nudged simulations, the outer flow is driven toward a target mean profile to minimize SGS errors. In these tests, the wall model maintained high fidelity across a wide range of flow types. In *true a posteriori* simulations, BFM-WM-v2 still matched or outperformed EQWM, although some degradation was observed due to large external errors from the SGS model. These results emphasize that an accurate wall model is a necessary but not sufficient condition for accurate WMLES predictions [1]. Addressing external errors requires developing SGS models that are numerically consistent with the wall model—a topic we explore further in companion work and ongoing development of BFM-SGS-v2.

While the results demonstrate strong performance and generalization, several limitations remain. First, the model assumes that the wall-shear stress vector is aligned with the velocity vector at the first off-wall grid point. Although this assumption is reasonable in most high-Reynolds-number LES settings, it may introduce bias in flows with strong velocity skewing. Second, the current training dataset does not yet cover compressible flows, turbulence with pronounced mean-flow three-dimensionality, or laminar-to-turbulent transition scenarios, which may limit accuracy in some applications. The representation of wall-curvature effects in the training data is also still very limited. Third, external errors originating from the SGS model can degrade overall performance despite the intrinsic accuracy of the wall model, highlighting the need for co-trained or co-designed SGS and wall models.

These limitations motivate several directions for future research. Expanding the building-block training set to include richer transitional regimes and separated flows with strong three-dimensionality will improve robustness. Incorporating more nuanced representations of flow history or path-dependence may also aid in cases with strong memory effects. Most critically, there is a need for integrated modeling strategies in which the SGS model and wall model are developed jointly, ensuring numerical and physical consistency across the LES solver.

This study represents Part I of a two-part contribution. In Part II, we introduce three additional components that further enhance the performance and interpretability of the wall model: (i) a flow-regime classifier that identifies the dominant physics underlying each prediction and the specific training samples that support it; (ii) a predictive uncertainty model that decomposes the total error into epistemic and aleatoric components; and (iii) a confidence-scoring mechanism using a spectral-normalized Gaussian process that flags unreliable predictions and, when desired, corrects them through an additive error model. These additions render the model more interpretable and self-aware, enabling practical WMLES applications with integrated mechanisms for reliability, adaptation, and correction.

ACKNOWLEDGMENTS

This work was supported by the National Science Foundation (NSF) under grant number #2317254 and NSF CAREER #2140775. The project is also supported by an Early Career Faculty grant from NASA’s Space Tech-

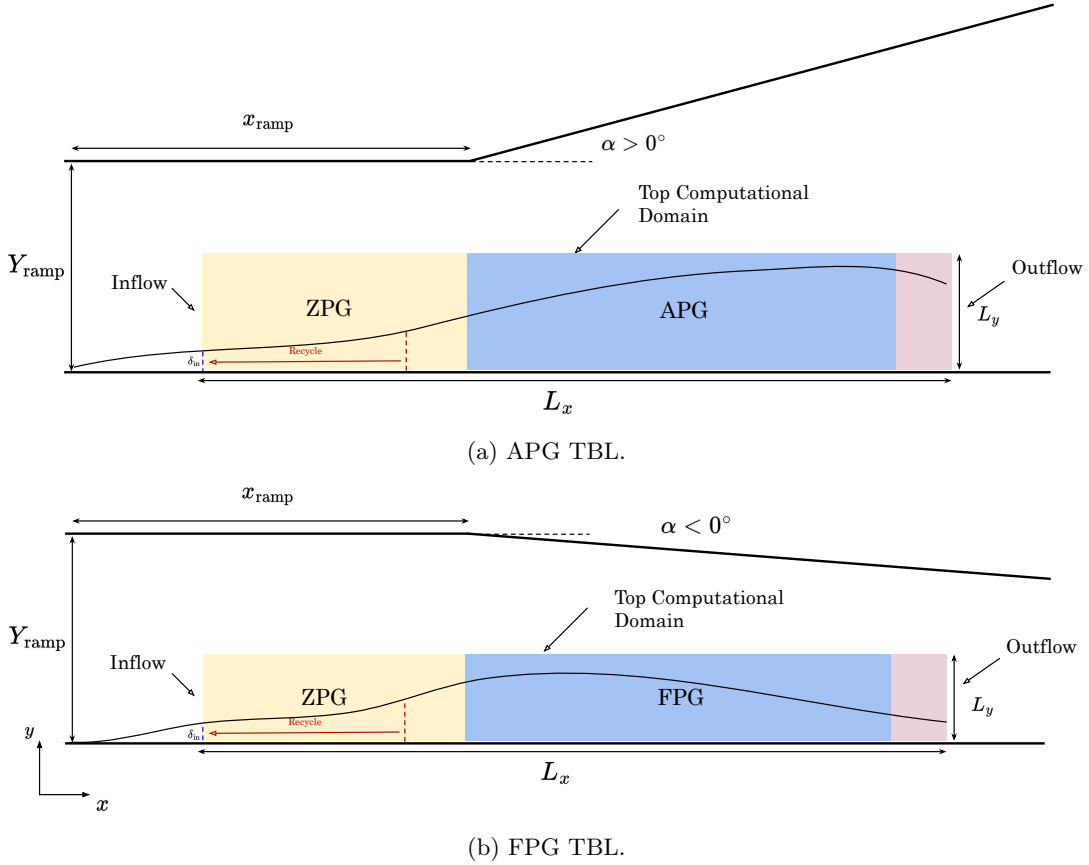


FIG. 34: Schematic of the new DNS of APG/FPG TBLs from Arranz and Lozano-Durán [65].

nology Research Grants Program (grant #80NSSC23K1498). The authors acknowledge the MIT Office of Research Computing and Data for providing high performance computing resources that have contributed to the research results reported within this paper. This work also used the DeltaAI and Delta system at the National Center for Supercomputing Applications and Bridges-2 at Pittsburgh Supercomputing Center through allocation PHY250022 from the Advanced Cyberinfrastructure Coordination Ecosystem: Services and Support (ACCESS) program, which is supported by National Science Foundation grants #2138259, #2138286, #2138307, #2137603, and #2138296.

Appendix A: DNS of APG/FPG turbulent boundary layers

A new set of DNS of APG and FPG turbulent boundary layers was conducted to fill gaps in the existing literature. The simulation setup is illustrated in Figure 34. We conceptualize a virtual straight ramp that is deflected either upward or downward to impose a pressure gradient. An upward deflection ($\alpha > 0^\circ$) generates an APG, whereas a downward deflection ($\alpha < 0^\circ$) produces an FPG. This two-dimensional ramp geometry is extruded in the spanwise direction to form a three-dimensional domain. We investigate a range of deflection angles, $\alpha \in [-4^\circ, -3^\circ, -2^\circ, -1^\circ, 5^\circ, 10^\circ, 15^\circ, 20^\circ]$, at two inflow friction Reynolds numbers, $Re_{\tau, in} = 300$ and 670 , for a total of 16 cases. A detailed analysis of the statistical properties of these TBLs is provided in Arranz and Lozano-Durán [65]; here, we summarize the main features of the cases.

The domain size is $L_x = 1200\theta_{in}$, $L_y = 200\theta_{in}$, and $L_z = 200\theta_{in}$ in the streamwise, wall-normal, and spanwise directions, respectively, for the APG cases, and $L_x = 1000\theta_{in}$, $L_y = 40\theta_{in}$, and $L_z = 200\theta_{in}$ for the FPG cases, where θ_{in} is the TBL momentum thickness at the inlet. The inflow boundary condition is obtained by imposing the mean velocity profile from DNS of a ZPG TBL at the corresponding Reynolds number [133], with superimposed quasi-periodic velocity fluctuations extracted from a downstream location at $x_{recycle} = 100\theta_{in}$. A convective outlet boundary condition, $\partial \mathbf{u} / \partial t + U_\infty \partial \mathbf{u} / \partial x = 0$, is applied at the domain exit [134], and small corrections are introduced to enforce global mass conservation [135]. The spanwise direction is treated as periodic. At the top boundary, we apply an inviscid potential-flow solution obtained by assuming a virtual wall located further above the domain. This

TABLE V: Comparison of current and previous APG/FPG TBL databases with current cases. $Re_\theta = U_\infty \theta / \nu$ is the momentum-thickness-based Reynolds number and β is the Clauser pressure-gradient parameter.

Case	Source	Type	Reynolds number range	β	Case count
APG	Bobke <i>et al.</i> [90]	WRLES	$910 < Re_\theta < 4320$	[0.86, 4.07]	5
Wing	Tanarro <i>et al.</i> [103], Hosseini <i>et al.</i> [144]	WRLES/DNS	$790 < Re_\theta < 3000$	[0.61, 85]	5
ZPG	Schlatter <i>et al.</i> [145], Schlatter and Örlü [146]	DNS	$500 < Re_\theta < 4300$	$\simeq 0$	2
ZPG	Eitel-Amor <i>et al.</i> [147]	WRLES	$600 < Re_\theta < 8300$	$\simeq 0$	1
ZPG	Sillero <i>et al.</i> [133]	DNS	$2780 < Re_\theta < 6600$	$\simeq 0$	1
APG followed by FPG	Gungor <i>et al.</i> [91]	DNS	$1238 < Re_\theta < 12970$	$[\sim 0, \infty]$	3
FPG and APG	Current	DNS	$300 < Re_\theta < 10000$	$[-0.6, \infty]$	16

is achieved by prescribing a pure potential source for the APG cases or a potential sink for the FPG cases. The FPG configurations considered here are similar to the sink-flow simulations of Dixit and Ramesh [136] and Spalart [137]. The wall-normal velocity is calculated by

$$v|_{L_y} = \frac{u_\infty L_y [(x_{\text{ramp}} - x_{\text{source}})^2 + L_y^2]}{(x_{\text{ramp}} - x_{\text{source}}) [(x - x_{\text{source}})^2 + L_y^2]}, \quad (\text{A1})$$

where x_{source} is determined from the requirement that, at x_{ramp} , the potential flow must be parallel to the linear ramp. The source location corresponds to the intersection of the ramp line with the horizontal bottom wall. It is computed as

$$x_{\text{source}} = x_{\text{ramp}} - Y_{\text{ramp}} \tan(\alpha). \quad (\text{A2})$$

The streamwise velocity boundary condition at the top boundary is then imposed by enforcing

$$\omega_z|_{L_y} = \frac{\partial v|_{L_y}}{\partial x} - \frac{\partial u|_{L_y}}{\partial y} = 0, \quad (\text{A3})$$

ensuring that the top boundary remains irrotational. The spanwise velocity shear, $\partial w / \partial y$, is set to zero at the top of the computational domain.

The solutions are computed by DNS of the incompressible Navier-Stokes equations. The spatial discretization is a staggered second-order central finite difference scheme [138]. Time advancement is achieved by a third-order Runge-Kutta scheme [139] combined with the fractional-step method [140]. The code has been validated in previous studies in turbulent channel flows [13, 141], zero-pressure-gradient turbulent boundary layer [142] and transitional boundary layers [32].

Some statistical properties of the simulations are shown in Figure 35, including the Clauser parameter β , the friction coefficient C_f , and the momentum-thickness Reynolds number Re_θ . The momentum thickness is computed following the method of Spalart and Watmuff [143]. Table V summarizes the ranges of β and Re_θ in the present TBL dataset and compares them with those from previous databases in the literature. The results show that our dataset spans a substantially wider Reynolds-number range and encompasses pressure-gradient conditions from strong FPG ($\beta < 0$) to near-incipient separation ($\beta \rightarrow \infty$).

Appendix B: Effect of using instantaneous inputs instead of averaged inputs

We examine the impact of using instantaneous input values rather than averaged inputs in BFM. Most wall models, such as EQWM, are calibrated or trained on mean quantities—i.e., given the mean velocity properties at the matching location, they return the mean wall-shear stress. Consider an exact-for-the-mean wall model of the form

$$\tau_{w,\text{true}} = f(\bar{\mathbf{q}}; \theta, h_{\text{wm}}), \quad (\text{B1})$$

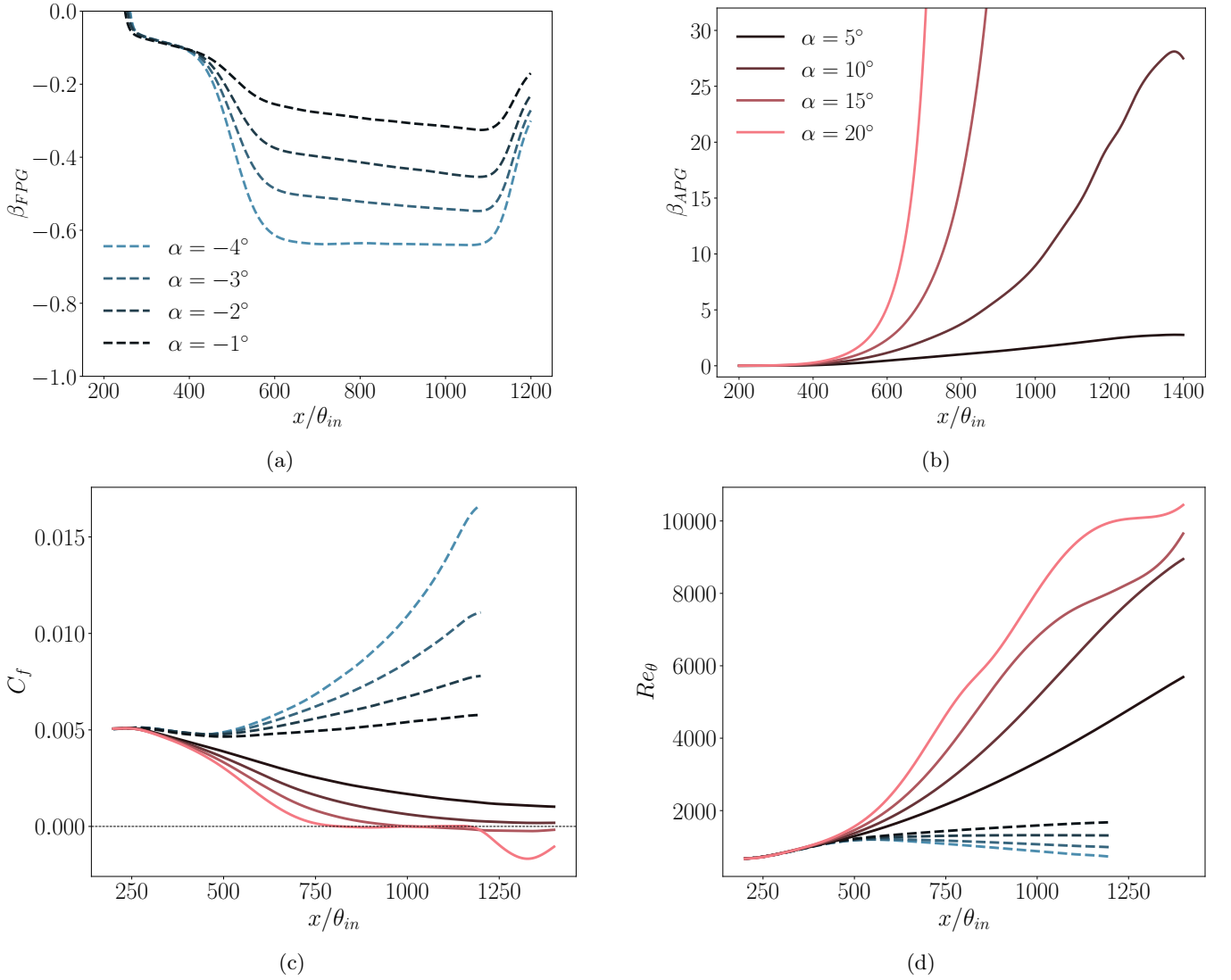


FIG. 35: Clauser pressure-gradient parameter β for (a) FPG and (b) APG cases. (c) Friction coefficient C_f and (d) Momentum-thickness-based Reynolds numbers Re_θ for all cases.

where f denotes the functional form of the wall model, \mathbf{q} is the vector of inputs at the matching location, $\overline{(\cdot)}$ denotes an ensemble average, θ represents the model parameters, and h_{wm} is the matching height. In *a posteriori* testing, the model takes as inputs instantaneous values and the predicted mean wall-shear stress is given by

$$\tau_{w,pred} = \overline{f(\mathbf{q}; \theta, h_{wm})}, \quad (\text{B2})$$

which does not need to coincide with $\tau_{w,true}$ as the inputs \mathbf{q} are now instantaneous. The relative error is defined as [148]

$$\varepsilon = \frac{\tau_{w,pred} - \tau_{w,true}}{\tau_{w,true}} = \frac{\overline{f(\mathbf{q}; \theta, h_{wm})}}{\overline{f(\overline{\mathbf{q}}; \theta, h_{wm})}} - 1, \quad (\text{B3})$$

assuming $\tau_{w,true} \neq 0$. As shown by Larsson [148], using instantaneous rather than averaged inputs in EQWM introduces only very small relative errors (below 2%). This result—derived using Reichardt’s law and DNS Reynolds-stress profiles via a Taylor-expansion analysis—provides indirect justification for the use of instantaneous flow information in wall models within an *a posteriori* context.

We estimate the modeling error in BFM under the simplifying assumption that \mathbf{q} follows a Gaussian distribution. Although \mathbf{q} is generally not Gaussian [149], this exercise is intended to illustrate why EQWM is comparatively less

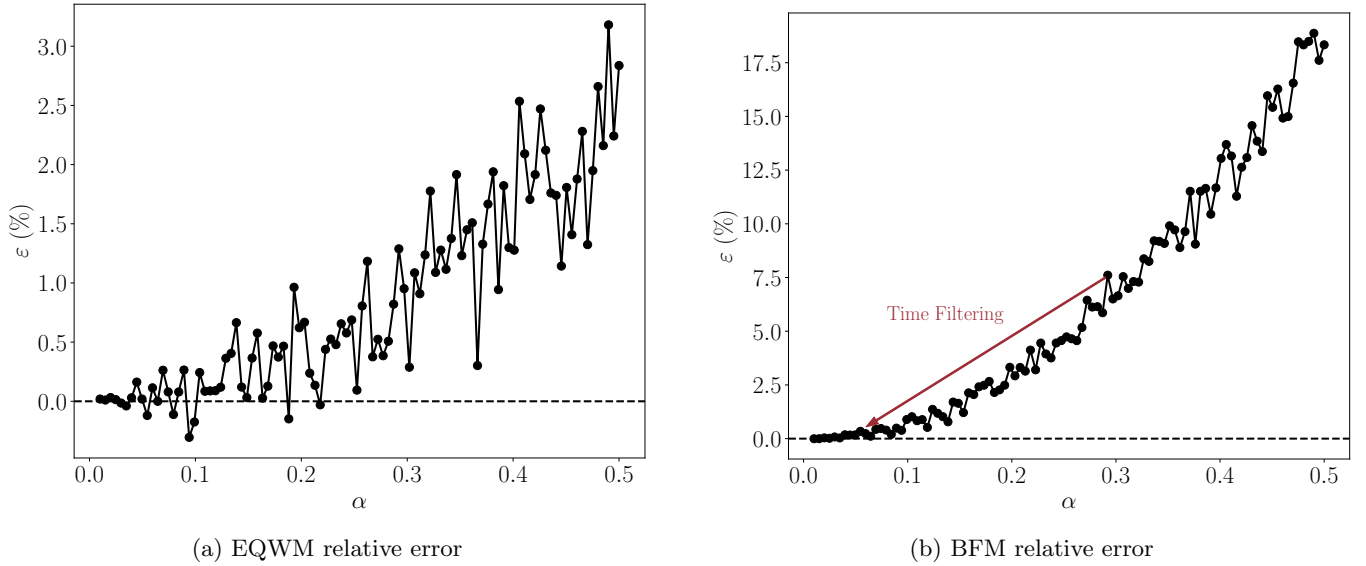


FIG. 36: Relative error induced by using instantaneous inputs for (a) EQWM and (b) BFM. The time filtering is used to reduce the scattering of the instantaneous inputs shown by the red arrow.

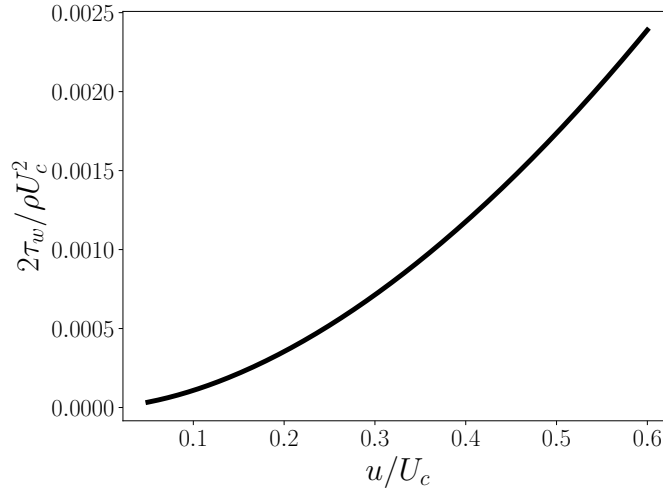


FIG. 37: Wall-shear stress predicted by the EQWM as a function of input velocity. U_c is the centerline velocity for the turbulent channel flow.

sensitive to errors induced by instantaneous inputs. For clarity, we restrict the analysis to a case with friction Reynolds number $Re_\tau = 4,200$.

For EQWM, the input \mathbf{q} reduces to a single scalar u , the wall-parallel velocity magnitude at the matching location. We assume $u \sim \mathcal{N}(\bar{u}, (\alpha_u \bar{u})^2)$, where α_u denotes the ratio of the standard deviation to the mean velocity. For each $\alpha_u \in [0.01, 0.5]$ (incremented by 0.005), we generated 100,000 samples and evaluated the mean prediction using Eq. 13. As shown in Figure 36a, the error introduced by instantaneous inputs remains below 3%, even when α_u reaches 0.5. This finding is consistent with prior work demonstrating that EQWM is relatively insensitive to such errors [148]. The primary reason for this robustness is that although EQWM (Eq. 13) is nonlinear, it is monotonic and contains only mild departures from linearity, as illustrated in Figure 37.

We conducted a similar analysis for BFM. For simplicity, we set the pressure-gradient input to zero and examined how the joint variability of u_1 and u_2 affects the predicted output. We assume they follow the joint distribution

$$\begin{pmatrix} u_1 \\ u_2 \end{pmatrix} \sim \mathcal{N}\left(\begin{pmatrix} \bar{u}_1 \\ \bar{u}_2 \end{pmatrix}, \begin{pmatrix} (\alpha_u \bar{u}_1)^2 & \alpha_u^2 \bar{u}_1 \bar{u}_2 \\ \alpha_u^2 \bar{u}_1 \bar{u}_2 & (\alpha_u \bar{u}_2)^2 \end{pmatrix}\right). \quad (\text{B4})$$

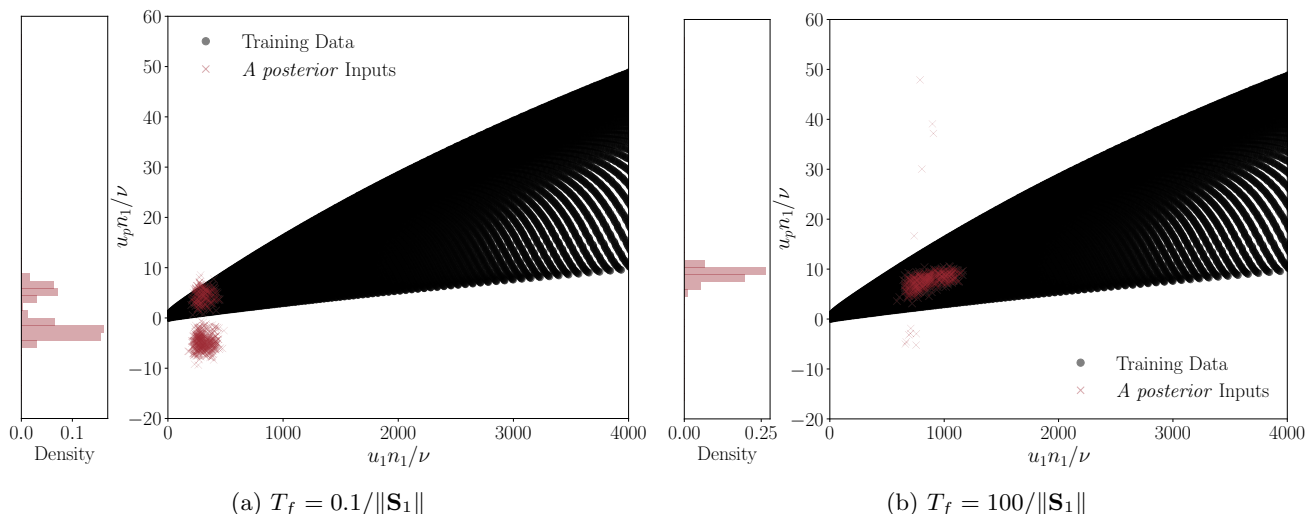


FIG. 38: Comparison between model inputs fed into the model in *a posteriori* testing and training data for a turbulent channel flow with constant (a) $C = 0.1$ and (b) $C = 100$.

We then evaluate how the error ε varies with α_u . The results, shown in Figure 36b, reveal that an $\alpha_u = 0.5$ leads to substantially larger errors—up to 20%—in contrast to the much smaller errors observed for EQWM. This indicates that directly using instantaneous inputs may result in inaccurate predictions in BFM. As discussed in the main text, a time filter is applied to reduce α_u and improve the relative error. For models involving multiple inputs, such filtering is generally necessary to maintain robust performance. As highlighted by the red arrow in Figure 36b, the primary effect of the time filter is to reduce the standard-deviation coefficient α_u , mitigating the induced modeling error.

Appendix C: Effect of timescale used for time filtering

A time filter is applied to the velocity u and pressure p to obtain the BFM inputs. The filter uses a timescale T_f defined as $T_f = C / \|\mathbf{S}_1\|$, where $\|\mathbf{S}_1\|$ is the magnitude of the rate-of-strain tensor at the first matching location. The choice of the coefficient C is critical. If C is too small, the resulting timescale T_f becomes too short, leading to large oscillations in the pressure gradient and, consequently, incorrect model inputs. As shown in Figure 38a, when $C = 0.1$ the pressure-gradient input oscillates between positive and negative values, with more than half of the samples spuriously negative. When the timescale is increased by a factor of 1000, as shown in Figure 38b, nearly all points fall within the correct training range.

There is, however, a trade-off: choosing an excessively large T_f slows the convergence of the simulation. An optimal value of C must therefore balance input smoothness with computational cost. To identify this optimum, we varied C and recorded the percentage of inputs in the *a posteriori* testing that remained within the region $u_p n_1 / \nu > 0$, which is physically consistent with the exact DNS input. As shown in Figure 39, once C reaches 100, more than 98% of the points lie close to the DNS mean value, and further increases yield diminishing returns. Accordingly, we set $C = 100$ for this study.

After setting the filtering timescale, a one-sided exponential filter is applied to the primal variables u and p . The filtered variable Φ is updated at each time step using the formula:

$$\Phi(t) = \epsilon_f \phi(t) + (1 - \epsilon_f) \Phi(t - \Delta t), \quad (\text{C1})$$

where ϕ is the instantaneous variable, $\Phi(t - \Delta t)$ is the filtered variable from the previous time step, Δt is the simulation time step size, and the filtering coefficient ϵ_f is defined as $\epsilon_f = \Delta t / T_f$. Finally, these time-filtered dimensional variables are processed to generate the model inputs.

Appendix D: Effect of wall-curvature training data

We examine how the model performance is affected when the Gaussian bump case, which is the only training case that includes wall-curvature effects, is removed from the training dataset. This analysis assesses the importance of

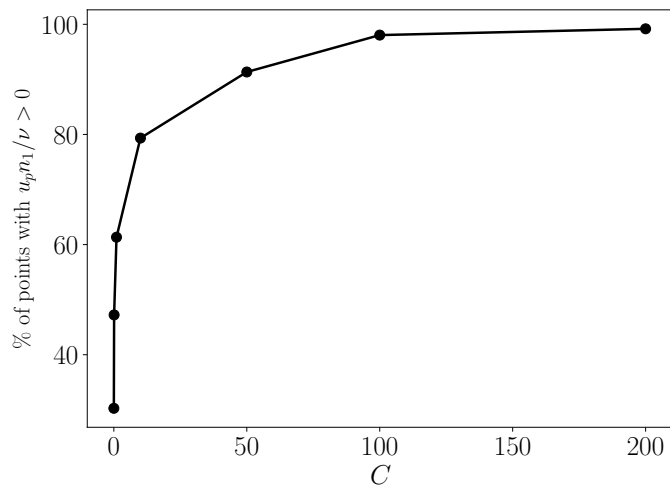


FIG. 39: Percentage of points falling into the region $u_p n_1 / \nu > 0$ as a function of C .

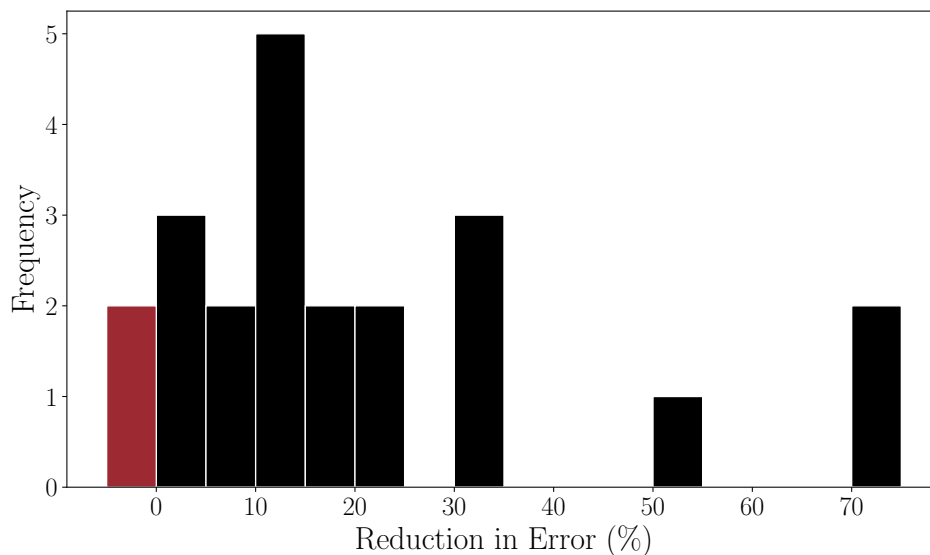


FIG. 40: Reduction in relative error for cases with wall curvature when curvature-containing training data (i.e., the Gaussian bump) is included in the training set. The vertical axis indicates the number of cases. The red bar highlights the two cases for which incorporating curved-wall training data resulted in reduced prediction accuracy.

incorporating turbulence over curved walls into the training set. A new model was trained using the same architecture and hyperparameters described in the main text, but excluding the Gaussian bump data. Its accuracy was then compared with that of the full model for flows involving wall curvature. As shown in Figure 40, when the curvature-containing training data are included, all but two curvature cases exhibit reduced prediction error. This demonstrates that including curvature effects in the training dataset is essential for achieving accurate performance across flow regimes involving wall curvature.

Appendix E: Effect of SGS models on Gaussian bump results

The influence of the SGS model on the *a posteriori* performance for the Gaussian bump case is shown in Figure 41 and Figure 42. The results correspond to simulations using the same grid described in Section III B. Consistent with the observations of Whitmore *et al.* [150] and Agrawal *et al.* [151], the choice of SGS model has a significant impact on the overall WMLES performance for this configuration. For example, at the grid resolution examined here, the

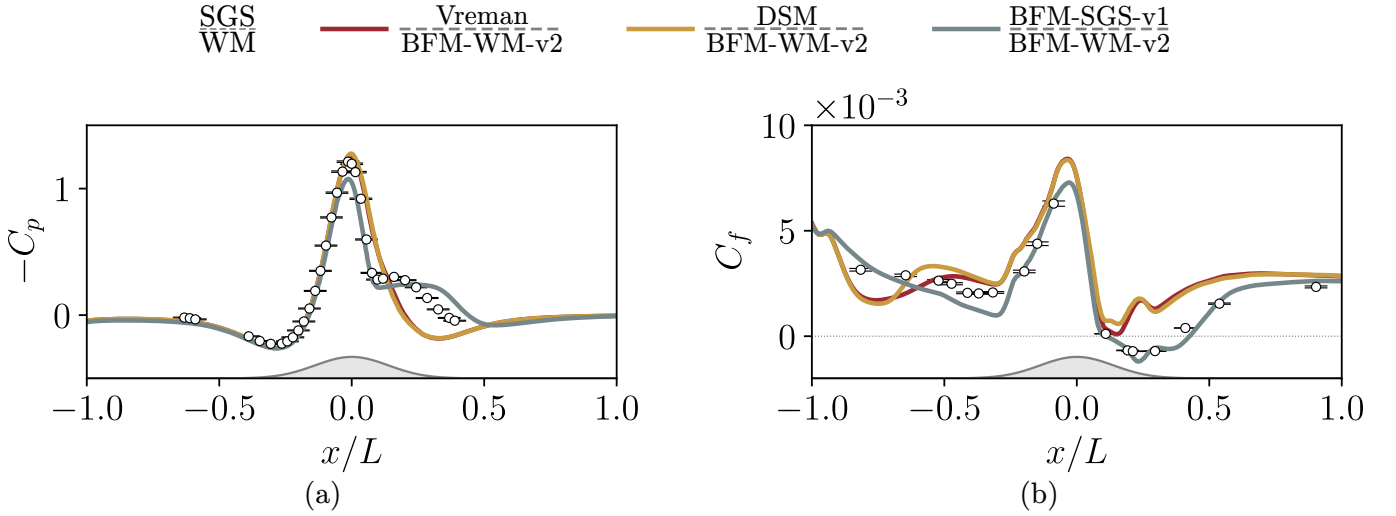


FIG. 41: *A posteriori* testing for the Gaussian bump. (a) Pressure coefficient and (b) friction coefficient in the plane $z/L = 0$. All three curves use BFM-WM-v2 as the wall model. The red line corresponds to the Vreman SGS model, the yellow line to DSM, and the green line to the BFM-SGS-v1 model from Arranz *et al.* [53].

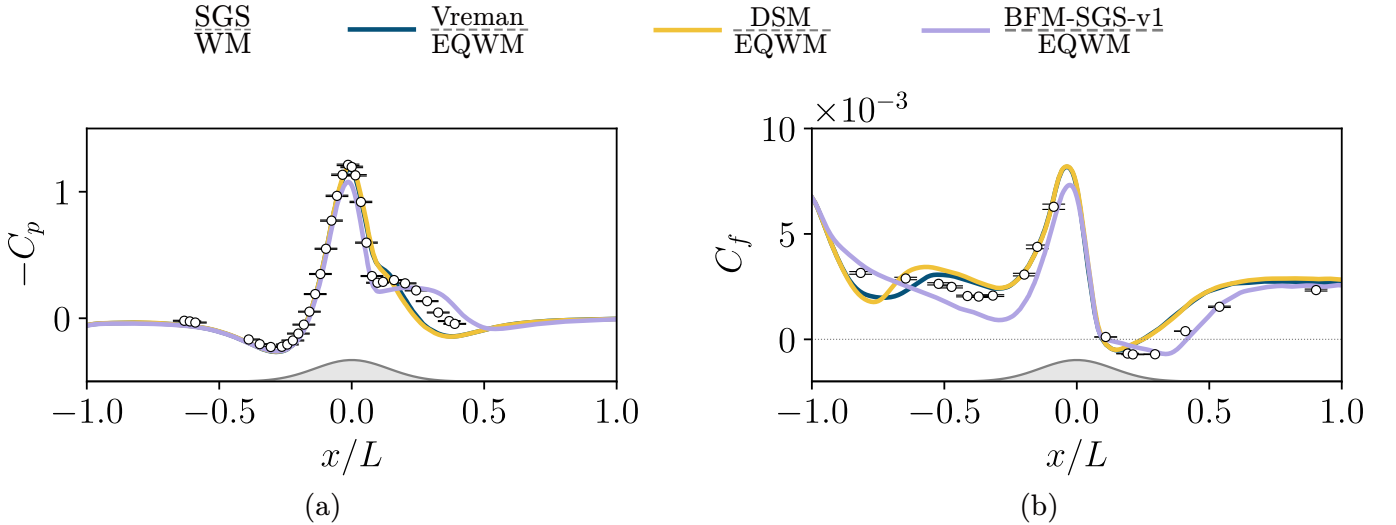


FIG. 42: *A posteriori* testing for the Gaussian bump. (a) Pressure coefficient and (b) friction coefficient in the plane $z/L = 0$. All three curves use EQWM as the wall model. The blue line corresponds to the Vreman SGS model, the yellow line to DSM, and the purple line to the BFM-SGS-v1 model from Arranz *et al.* [53].

Vreman and DSM models yield comparable accuracy when coupled with BFM-WM-v2, whereas the BFM-SGS-v1 model provides substantially improved predictions. A more systematic investigation—such as a full grid convergence study—is required to assess the convergence properties of BFM-WM-v2 once the forthcoming BFM-SGS-v2 model, designed to be numerically consistent with the current BFM wall model, becomes available.

Appendix F: Investigation of the BFM output landscape

We examine the model behavior in regions not covered by the training data. Although overfitting was mitigated during training through L_2 regularization and early stopping, it is still necessary to assess the model's behavior explicitly. Figure 43 shows the model output, $u_\tau n_1/\nu$, plotted as a function of $u_1 n_1/\nu$ and $u_2 n_1/\nu$, with the third input $u_p n_1/\nu$ fixed at zero, corresponding to the ZPG case. The output surface is smooth and free of the abrupt peaks or valleys typically associated with overfitting. A similar plot with $u_p n_1/\nu = 100$ (Figure 44) leads to the same conclusion.

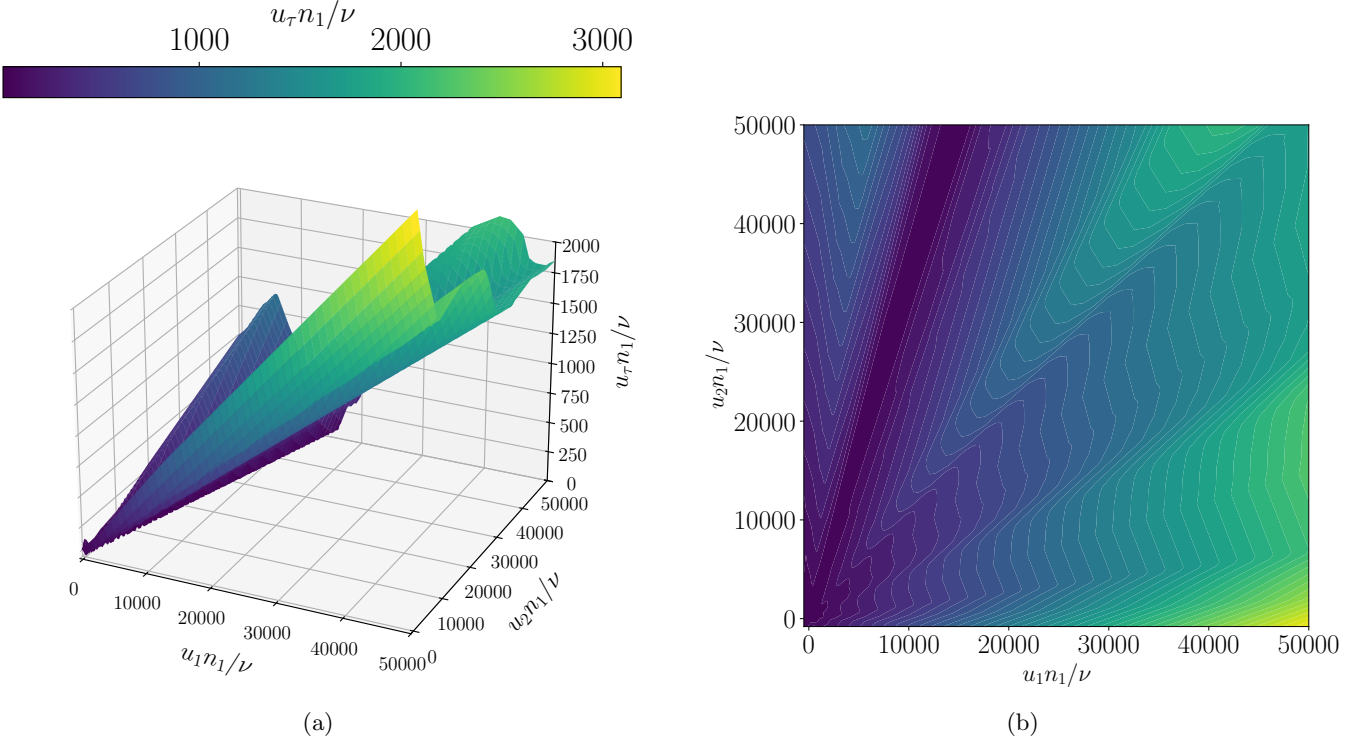


FIG. 43: (a) Surface representation of the BFM-WM-v2 output and (b) its corresponding 2-D projection, showing the dependence of $u_\tau n_1/\nu$ on the inputs $u_1 n_1/\nu$ and $u_2 n_1/\nu$. The third input, $u_p n_1/\nu$, is held fixed at 0. The color scale in both panels indicates the output value.

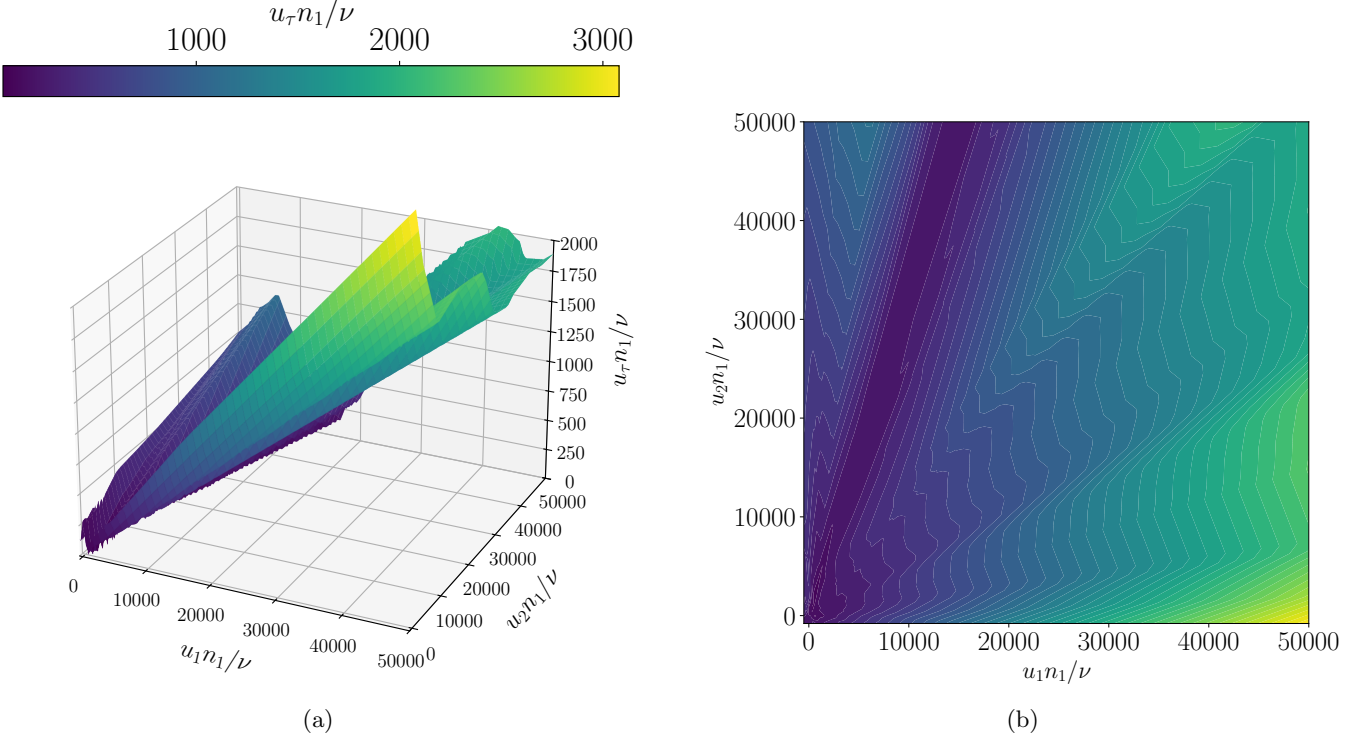


FIG. 44: (a) Surface representation of the BFM-WM-v2 output and (b) its corresponding 2-D projection, showing the dependence of $u_\tau n_1/\nu$ on the inputs $u_1 n_1/\nu$ and $u_2 n_1/\nu$. The third input, $u_p n_1/\nu$, is held fixed at 100. The color scale in both panels indicates the output value.

-
- [1] A. Lozano-Durán and H. J. Bae, *J. Fluid Mech.* **963**, A35 (2023).
- [2] J. P. Slotnick, A. Khodadoust, J. Alonso, D. Darmofal, W. Gropp, E. Lurie, and D. J. Mavriplis, *CFD Vision 2030 Study: A Path to Revolutionary Computational Aerosciences*, Tech. Rep. NASA/CR-2014-218178 (National Aeronautics and Space Administration, Langley Research Center, Hampton, VA, 2014).
- [3] M. Mani and A. J. Dorgan, *Annu. Rev. Fluid Mech.* **55**, 431 (2023).
- [4] J. W. Deardorff, *J. Fluid Mech.* **41**, 453 (1970).
- [5] U. Schumann, *J. Comput. Phys.* **18**, 376 (1975).
- [6] U. Piomelli, *Annu. Rev. Fluid Mech.* **34**, 349 (2002).
- [7] J. Larsson, S. Kawai, J. Bodart, and I. Bermejo-Moreno, *Mech. Eng. Rev.* **3**, 15 (2016).
- [8] S. T. Bose and G. I. Park, *Annu. Rev. Fluid Mech.* **50**, 535 (2018).
- [9] E. Balaras, C. Benocci, and U. Piomelli, *AIAA J.* **34**, 1111 (1996).
- [10] W. Cabot and P. Moin, *Flow Turbul. Combust.* **63**, 269 (2000).
- [11] M. Wang and P. Moin, *Phys. Fluids* **14**, 2043 (2002).
- [12] G. I. Park and P. Moin, *Phys. Fluids* **26**, 015108 (2014).
- [13] A. Lozano-Durán, M. G. Giometto, G. I. Park, and P. Moin, *J. Fluid Mech.* **883**, A20 (2020).
- [14] I. Hayat and G. I. Park, *AIAA J.* **62**, 557 (2024).
- [15] G. Hoffmann and C. Benocci, in *Advances in Turbulence V: Proceedings of the Fifth European Turbulence Conference, Siena, Italy, 5–8 July 1994* (Springer, 1995) pp. 222–228.
- [16] S. Hickel, E. Touber, J. Bodart, and J. Larsson, in *Eighth International Symposium on Turbulence and Shear Flow Phenomena* (Begel House Inc., 2013).
- [17] Y. Tamaki, Y. Fukushima, Y. Kuya, and S. Kawai, *Phys. Rev. Fluids* **5**, 074602 (2020).
- [18] P. Catalano, M. Wang, G. Iaccarino, and P. Moin, *Int. J. Heat Fluid Flow* **24**, 463 (2003).
- [19] R. Kamogawa, Y. Tamaki, and S. Kawai, *Phys. Rev. Fluids* **8**, 064605 (2023).
- [20] M. Fowler, T. A. Zaki, and C. Meneveau, *J. Fluid Mech.* **974**, A51 (2023).
- [21] S. T. Bose and P. Moin, *Phys. Fluids* **26**, 015104 (2014).
- [22] H. J. Bae, A. Lozano-Durán, S. T. Bose, and P. Moin, *J. Fluid Mech.* **859**, 400 (2019).
- [23] P. Raje and K. Duraisamy, *J. Fluid Mech.* **1017**, A35 (2025).
- [24] M. Manhart, N. Peller, and C. Brun, *Theor. Comput. Fluid Dyn.* **22**, 243 (2008).
- [25] C. Duprat, G. Balarac, O. Métais, P. M. Congedo, and O. Brugière, *Phys. Fluids* **23**, 015101 (2011).
- [26] D. R. Gonzalez, M. C. Adler, and D. V. Gaitonde, in *2018 AIAA Aerospace Sciences Meeting* (American Institute of Aeronautics and Astronautics, Kissimmee, Florida, 2018).
- [27] R. Agrawal, S. T. Bose, and P. Moin, *Phys. Rev. Fluids* **9**, 124603 (2024).
- [28] J. Bodart and J. Larsson, 2012 CTR Annu. Res. Briefs **2012**, 229 (2012).
- [29] C. Gonzalez, M. Karp, and P. Moin, 2020 CTR Annu. Res. Briefs , 85 (2020).
- [30] E. T. Dauricio and J. L. F. Azevedo, *J. Comput. Phys.* **484**, 112087 (2023).
- [31] N. Dujardin, *A Wall Model for LES of Flows with Laminar-Turbulent Transition*, Master’s thesis, Université de Liège, Liège, Belgique (2023).
- [32] A. Lozano-Durán, M. J. P. Hack, and P. Moin, *Phys. Rev. Fluids* **3**, 023901 (2018).
- [33] K. P. Griffin, L. Fu, and P. Moin, *Phys. Rev. Fluids* **6**, 024608 (2021).
- [34] X. I. A. Yang, S. Zafar, J.-X. Wang, and H. Xiao, *Phys. Rev. Fluids* **4**, 034602 (2019).
- [35] Z. Zhou, G. He, and X. Yang, *Phys. Rev. Fluids* **6**, 054610 (2021).
- [36] Z. Zhou, X. I. Yang, F. Zhang, and X. Yang, *Phys. Fluids* **35** (2023).
- [37] X. Huang, X. Yang, and R. Kunz, *Phys. Fluids* **31**, 125105 (2019).
- [38] R. Zangeneh, *Phys. Fluids* **33**, 126103 (2021).
- [39] H. J. Bae and P. Koumoutsakos, *Nat. Commun.* **13**, 1443 (2022).
- [40] D. Zhou and H. J. Bae, *AIAA J.* , 1 (2024).
- [41] A. Vadrot, X. I. A. Yang, H. J. Bae, and M. Abkar, *Phys. Fluids* **35**, 055122 (2023).
- [42] D. Dupuy, N. Odier, and C. Lapeyre, *J. Comput. Phys.* **487**, 112173 (2023).
- [43] D. Dupuy, N. Odier, C. Lapeyre, and D. Papadogiannis, *Data-Centric Eng.* **4**, e7 (2023).
- [44] D. Dupuy, N. Odier, and C. Lapeyre, *Data-Centric Eng.* **5**, e10 (2024).
- [45] G. Tabe Jamaat and Y. Hattori, *Phys. Fluids* **35**, 055117 (2023).
- [46] G. Tabe Jamaat, Y. Hattori, and S. Kawai, *Phys. Fluids* **36**, 065164 (2024).
- [47] M. Boxho, *Development of machine learning based wall shear stress models for LES in the presence of adverse pressure gradients and separation*, Ph.D. thesis, Université de Liège (2024).
- [48] M. Boxho, T. Toulorge, M. Rasquin, G. Winckelmans, G. Dergham, and K. Hillewaert, *Flow Turbul. Combust.* , 1 (2025).
- [49] A. Lozano-Durán, G. Arranz, and Y. Ling, in *AIAA Aviation 2023 Forum* (AIAA, San Diego, CA and Online, 2023).
- [50] R. Ma, Y. Yuan, G. Arranz, Y. Ling, R. Agrawal, M. Whitmore, A. Elnahas, C. Pederson, and A. Lozano-Durán, 2024 CTR - Proc. Summer Prog. (2024).
- [51] G. Arranz, Y. Ling, and A. Lozano-Durán, in *AIAA Aviation 2023 Forum* (AIAA, San Diego, CA and Online, 2023).
- [52] Y. Ling, S. Costa, G. Arranz, K. Goc, M. Mani, and A. Lozano-Durán, in *AIAA Aviation Forum and Ascend 2024* (American Institute of Aeronautics and Astronautics, Las Vegas, Nevada, 2024).

- [53] G. Arranz, Y. Ling, S. Costa, K. Goc, and A. Lozano-Durán, *Comms. Eng.* **3**, 127 (2024).
- [54] Y. M. Lee, J. H. Lee, and J. Lee, *Aerosp. Sci. Technol.* **132**, 108014 (2023).
- [55] S. Maejima, K. Tanino, and S. Kawai, *Phys. Rev. Fluids* **9**, 084609 (2024).
- [56] S. Radhakrishnan, J. Calafell, A. Miró, B. Font, and O. Lehmkuhl, *Int. J. Numer. Methods Heat Fluid Flow* **34**, 3166 (2024).
- [57] F. Zhang, Z. Zhou, X. Yang, and G. He, *J. Fluid Mech.* **1011**, R1 (2025).
- [58] Z. Zhou, X.-l. Zhang, G.-w. He, and X. Yang, *J. Fluid Mech.* **1002**, A3 (2025).
- [59] A. Lozano-Durán and H. J. Bae, *J. Comput. Phys.* **392**, 532 (2019).
- [60] A. Lozano-Durán, S. T. Bose, and P. Moin, *AIAA J.* **60**, 747 (2022).
- [61] Y. Ling, G. Arranz, E. Williams, K. Goc, K. Griffin, and A. Lozano-Durán, *2022 CTR - Proc. Summer Prog.*, 5 (2022).
- [62] R. Ma and A. Lozano-Durán, *J. Fluid Mech.* **1007** (2025).
- [63] V. Baxerres, R. Vinuesa, and H. Nagib, *J. Fluid Mech.* **987**, R8 (2024).
- [64] X. I. A. Yang, J. Sadique, R. Mittal, and C. Meneveau, *Phys. Fluids* **27**, 025112 (2015).
- [65] G. Arranz and A. Lozano-Durán, *arXiv* (2025).
- [66] A. Lozano-Durán and J. Jiménez, *Phys. Fluids* **26**, 011702 (2014).
- [67] M. Lee and R. D. Moser, *J. Fluid Mech.* **774**, 395 (2015).
- [68] S. Hoyas, M. Oberlack, F. Alcántara-Ávila, S. V. Kraheberger, and J. Laux, *Phys. Rev. Fluids* **7**, 014602 (2022).
- [69] S. B. Pope, *Turbulent Flows*, Vol. 12 (Cambridge University Press, 2000).
- [70] V. M. Falkner and S. W. Skan, *Lond. Edinb. Dubl. Phil. Mag.* **7**, **12**, 865 (1931).
- [71] A. Uzun and M. R. Malik, *AIAA J.* **60**, 2130 (2022).
- [72] J. Eaton and J. Johnston, *AIAA J.* **19**, 1093 (1981).
- [73] R. L. Simpson, *J. Fluids Eng.* **103**, 520 (1981).
- [74] E. Buckingham, *Phys. Rev.* **4**, 345 (1914).
- [75] Y. Yuan and A. Lozano-Durán, *Nat. Commun.* **16**, 9171 (2025).
- [76] A. Lozano-Durán and G. Arranz, *Phys. Rev. Res.* **4**, 023195 (2022).
- [77] C. E. Shannon, *Bell System Technical Journal* **27**, 623 (1948).
- [78] N. Hansen, S. D. Müller, and P. Koumoutsakos, *Evol. Comput.* **11**, 1 (2003).
- [79] N. Hansen, Y. Akimoto, and P. Baudis, *CMA-ES/pycma on Github, Zenodo*, DOI:10.5281/zenodo.2559634 (2019).
- [80] P. J. Huber, in *Breakthroughs in statistics: Methodology and distribution* (Springer, 1992) pp. 492–518.
- [81] D. P. Kingma and J. Ba, *Adam: A method for stochastic optimization* (2017).
- [82] A. Paszke, S. Gross, F. Massa, A. Lerer, J. Bradbury, G. Chanan, T. Killeen, Z. Lin, N. Gimelshein, L. Antiga, A. Desmaison, A. Köpf, E. Yang, Z. DeVito, M. Raison, A. Tejani, S. Chilamkurthy, B. Steiner, L. Fang, J. Bai, and S. Chintala, *Pytorch: An imperative style, high-performance deep learning library* (2019).
- [83] Y. Ling and A. Lozano-Durán, in *AIAA SCITECH 2025 Forum* (American Institute of Aeronautics and Astronautics, Orlando, FL, 2025).
- [84] S. Pirozzoli, J. Romero, M. Fatica, R. Verzicco, and P. Orlandi, *J. Fluid Mech.* **926**, A28 (2021).
- [85] S. Pirozzoli, D. Modesti, P. Orlandi, and F. Grasso, *J. Fluid Mech.* **840**, 631 (2018).
- [86] D. Modesti, S. Pirozzoli, P. Orlandi, and F. Grasso, *J. Fluid Mech.* **847**, R1 (2018).
- [87] H. Andersson and R. Kristoffersen, in *Turbulent Shear Flows 9: Selected Papers from the Ninth International Symposium on Turbulent Shear Flows, Kyoto, Japan, August 16–18, 1993* (Springer, 1995) pp. 53–70.
- [88] F. Hirt and H. Thomann, *J. Fluid Mech.* **171**, 547 (1986).
- [89] R. J. Volino, *J. Fluid Mech.* **897**, A2 (2020).
- [90] A. Bobke, R. Vinuesa, R. Örlü, and P. Schlatter, *J. Fluid Mech.* **820**, 667 (2017).
- [91] T. R. Gungor, Y. Maciel, and A. G. Gungor, *J. Fluid Mech.* **948**, A5 (2022).
- [92] T. R. Gungor, A. G. Gungor, and Y. Maciel, *J. Fluid Mech.* **997**, A75 (2024).
- [93] D. M. Driver and H. L. Seegmiller, *AIAA J.* **23**, 163 (1985).
- [94] G. N. Coleman, C. L. Rumsey, and P. R. Spalart, *J. Fluid Mech.* **847**, 28 (2018).
- [95] G. N. Coleman, C. L. Rumsey, and P. R. Spalart, *J. Fluid Mech.* **880**, 684 (2019).
- [96] M. Marquillie, U. Ehrenstein, and J.-P. Laval, *J. Fluid Mech.* **681**, 205 (2011).
- [97] A. J. Smits, S. T. B. Young, and P. Bradshaw, *J. Fluid Mech.* **94**, 209 (1979).
- [98] R. S. Barlow and J. P. Johnston, *J. Fluid Mech.* **191**, 137 (1988).
- [99] D. Simmons, F. Thomas, T. Corke, and F. Hussain, *J. Fluid Mech.* **944**, A42 (2022).
- [100] A. Uzun and M. R. Malik, *Direct Numerical Simulation of Smooth-Body Flow Separation Around a Ramp*, Technical Memorandum (National Aeronautics and Space Administration, Langley Research Center, Hampton, VA, 2024).
- [101] J. Appelbaum, M. Kloker, and C. Wenzel, *Theor. Comput. Fluid Dyn.* **39**, 10 (2025).
- [102] A. Uzun and M. R. Malik, *Theor. Comput. Fluid Dyn.* **35**, 293 (2021).
- [103] Á. Tanarro, R. Vinuesa, and P. Schlatter, *J. Fluid Mech.* **883**, A8 (2020).
- [104] P. Balakumar and G. I. Park, in *45th AIAA Fluid Dynamics Conference* (American Institute of Aeronautics and Astronautics, Dallas, TX, 2015).
- [105] X. Gloerfelt and P. Cinnella, *Flow Turbul. Combust.* **103**, 55 (2019).
- [106] F. Bassi, L. Botti, A. Colombo, A. Crivellini, A. Ghidoni, and F. Massa, *Eur. J. Mech. B Fluids* **55**, 367 (2016).
- [107] Y. Tamaki and S. Kawai, *AIAA J.* **61**, 698 (2023).
- [108] A. Uzun and M. R. Malik, *AIAA J.* **56**, 715 (2018).

- [109] R. C. Swanson and S. Langer, *Comparison of NACA 0012 Laminar Flow Solutions: Structured and Unstructured Grid Methods*, Technical Memorandum NASA/TM-2016-219003 (National Aeronautics and Space Administration, Langley Research Center, Hampton, VA, 2016).
- [110] P. Roach, Numerical simulation of unsteady flows and transition to turbulence (1990).
- [111] J. H. Lee, *J. Fluid Mech.* **810**, 323 (2017).
- [112] B. Van Den Berg, A. Elsenaar, J. P. F. Lindhout, and P. Wesseling, *J. Fluid Mech.* **70**, 127 (1975).
- [113] L. Pompeo, M. S. Bettelini, and H. Thomann, *J. Fluid Mech.* **257**, 507 (1993).
- [114] D. M. Driver and S. K. Hebbbar, *AIAA J.* **25**, 35 (1987).
- [115] J. Ohlsson, P. Schlatter, P. F. Fischer, and D. S. Henningson, *J. Fluid Mech.* **650**, 307 (2010).
- [116] O. Lehmkuhl, G. Houzeaux, H. Owen, G. Chrysokentis, and I. Rodríguez, *J. Comput. Phys.* **390**, 51 (2019).
- [117] K. A. Goc, O. Lehmkuhl, G. I. Park, S. T. Bose, and P. Moin, *Flow* **1**, E14 (2021).
- [118] K. A. Goc, P. Moin, S. T. Bose, and A. M. Clark, *J. Aircr.* **61**, 267 (2024).
- [119] K. A. Goc, R. Agrawal, S. T. Bose, and P. Moin, *J. Aircr.* , 1 (2025).
- [120] G. A. Bres, F. E. Ham, J. W. Nichols, and S. K. Lele, *AIAA J.* **55**, 1164 (2017).
- [121] A. Vreman, *Phys. Fluids* **16**, 3670 (2004).
- [122] P. D. Gray, I. Gluzman, F. O. Thomas, and T. C. Corke, in *AIAA Scitech 2022 Forum* (2022) p. 1209.
- [123] A. M. Clark, C. Rumsey, J. P. Slotnick, and L. Wang, in *AIAA SciTech 2025 Forum* (2025).
- [124] C. C. Kiris, A. Ghate, and J. Angel, in *AIAA SCITECH 2025 Forum* (2025) p. 0049.
- [125] P. R. Spalart, *J. Fluid Mech.* **205**, 319 (1989).
- [126] A. Lozano-Durán, H. J. Bae, and M. P. Encinar, *J. Fluid Mech.* **882**, A2 (2020).
- [127] P. A. Srinivasan, L. Guastoni, H. Azizpour, P. Schlatter, and R. Vinuesa, *Phys. Rev. Fluids* **4**, 054603 (2019).
- [128] T. Nakamura, K. Fukami, K. Hasegawa, Y. Nabae, and K. Fukagata, *Phys. Fluids* **33**, 025116 (2021).
- [129] G. Soldati, P. Orlandi, and S. Pirozzoli, *J. Fluid Mech.* **1007**, A28 (2025).
- [130] G. Brethouwer, *J. Fluid Mech.* **931**, A21 (2022).
- [131] N. Xu and I. Bermejo-Moreno, *Phys. Rev. Fluids* **9**, 114605 (2024).
- [132] L. Wang, X. Zhang, H. Su, and J. Zhu, *IEEE Trans. Pattern Anal. Mach. Intell.* (2024).
- [133] J. A. Sillero, J. Jiménez, and R. D. Moser, *Phys. Fluids* **25** (2013).
- [134] L. L. Pauley, P. Moin, and W. C. Reynolds, *J. Fluid Mech.* **220**, 397 (1990).
- [135] M. P. Simens, J. Jiménez, S. Hoyas, and Y. Mizuno, *J. Comp. Phys.* **228**, 4218 (2009).
- [136] S. A. Dixit and O. Ramesh, *J. Fluid Mech.* **615**, 445 (2008).
- [137] P. R. Spalart, *J. Fluid Mech.* **172**, 307 (1986).
- [138] P. Orlandi, *Fluid Flow Phenomena: a Numerical Toolkit*, Vol. 55 (Springer Science & Business Media, 2000).
- [139] A. A. Wray, NASA Ames Research Center, California, Report No. MS **202** (1990).
- [140] J. Kim and P. Moin, *J. Comput. Phys.* **59**, 308 (1985).
- [141] H. J. Bae, A. Lozano-Durán, S. Bose, and P. Moin, *Phys. Rev. Fluids* **3**, 014610 (2018).
- [142] A. Towne, S. T. Dawson, G. A. Brès, A. Lozano-Durán, T. Saxton-Fox, A. Parthasarathy, A. R. Jones, H. Biler, C.-A. Yeh, H. D. Patel, *et al.*, *AIAA J.* **61**, 2867 (2023).
- [143] P. R. Spalart and J. H. Watmuff, *J. Fluid Mech.* **249**, 337 (1993).
- [144] S. Hosseini, R. Vinuesa, P. Schlatter, A. Hanifi, and D. Henningson, *Int. J. Heat Fluid Flow* **61**, 117 (2016).
- [145] P. Schlatter, R. Örlü, Q. Li, G. Brethouwer, J. H. Fransson, A. V. Johansson, P. H. Alfredsson, and D. S. Henningson, *Phys. Fluids* **21** (2009).
- [146] P. Schlatter and R. Örlü, *J. Fluid Mech.* **659**, 116 (2010).
- [147] G. Eitel-Amor, R. Örlü, and P. Schlatter, *Int. J. Heat Fluid Flow* **47**, 57 (2014).
- [148] J. Larsson, WMLES: Instantaneous vs averaged input (2021), blog post.
- [149] S. P. Dinavahi, K. S. Breuer, and L. Sirovich, *Phys. Fluids* **7**, 1122 (1995).
- [150] M. Whitmore, K. Griffin, S. Bose, and P. Moin, 2021 CTR Annu. Res. Briefs , 45 (2021).
- [151] R. Agrawal, M. P. Whitmore, K. P. Griffin, S. T. Bose, and P. Moin, *Phys. Rev. Fluids* **7**, 074602 (2022).